Surface- Plasmon Optical and Electrochemical Characterization of Biofunctional Surface Architectures

Dissertation

zur Erlangung des Grades

Doktor der Naturwissenschaften

Am Fachbereich Biologie

Der Johannes Gutenberg-Universität Mainz

vorgelegt von

Lifang Niu

Aus Shanxi, V. R. China

Mainz, May, 2008

Tag der mündlichen Prüfung: 14, Mai 2008

Die vorliegende Arbeit wurde unter Betreuung von Herrn Prof. Dr. W. Knoll im Zeitraum zwischen June 2006 bis Mai 2008 am Max-Planck Institute für polymerforschung, Mainz, Deutschland angefertigt.

1 Introduction

1.1 *Overview and aim of this work*

Biomolecular interactions and molecular recognition processes are important to understand biological phenomena such as immunologic reactions and signal transduction. In addition, these biological recognition reactions have been proposed to be used in biosensor application. A number of analysis techniques used in biology, medicine and pharmacy have been developed over the past years. Novel detection methods have been developed which combine the specificity of biomolecular recognition systems with the advantages of instrumental analysis. Thus, biosensor devices have gained importance in areas like medical diagnostic, quality control and environmental analysis.

The aim of this study was primarily the development of biosensor formats based on supramolecular interfacial architecture, but included are also optical and electrochemical characterizations based on combination of evanescent wave techniques with electrochemical impedance.

There are several challenges in the field of design, assembly, and characterization of supramolecular (bio-) functional interfacial architectures for optical biosensing applications. The first is the development of immobilization technologies for stabilizing biomolecules and tethering them to a surfaces.[1] The usual aim is to produce a thin film of immobilized biologically active material on or near the transducer surface which responds only to the presence of one or a group of materials or substances requiring detection. Since the immobilization technique used to attach the biological material to the sensor surface is crucial to the operational behavior of the biosensor, realistic strategies for the development of immobilization techniques are essential for practically useful biosensors. The second important challenge is to develop a combination of detection techniques that has a substantial potential for highly controlled on-line monitoring of interaction activity. Only a combination of various methods can lead to a full understanding of complex processes such as the vesicle-to-tBLM transformation. In particular, techniques based on different transducer principles can be combined to test underlying assumptions used for interpretation of the response, and provide more various and detailed information on the test system.

Surface plasmon enhanced fluorescence spectroscopy (SPFS) was recently described[2] and the preliminary application of this technology for DNA detection on surfaces was shown.[3, 4] Driven by the impact of multi-parallel biomolecular detection by single sample or single assay, part of this study focuses on the development of surface array's electrochemical fabrication, as well as surface plasmon microscopy (SPM), surface plasmon enhanced fluorescence spectrometry (SPFS) and microscopy (SPFM) and their potential applications to biosensors.

Combination of electrochemistry and surface plasmon spectroscopy yields a powerful tool to investigate optical and electric properties of surface layers. The second part of this thesis is a study of the suitability of optical surface plasmon based and electrochemical impedance analysis for lipid membrane related biomolecular activities.

This chapter gives a brief background on biosensors. The following chapter focuses on the theoretical descriptions and working mechanisms of surface plasmon resonance (SPR) and impedance spectroscopy (EIS) techniques. It contains the electromagnetic theory necessary for the understanding of the surface plasmon resonance phenomenon. The optical excitation of surface plasmon modes is explained for prism coupling configuration. The basics of fluorescence, the combination of both techniques in the formations of SPFS (spectroscopy), SPFM (microscopy), SPFS (spectrometry) and the influence of surface plasmon fields in fluorophores close to planar surfaces are covered as well. It also contains the Langmuir theory describing adsorption processes.

Experimental methods and all information about sample preparation are given in chapter 3. The instrumental set-up used in this work is introduced in this chapter, together with the different modes of measurement.

In chapter 4 an electrochemical method to addressably mount oligonucleotides onto different sensing units in aqueous environment is introduced. Surface plasmon microscopy (SPM) is utilized for the on-line recording of functioning events. Hybridization reactions between targets from solution to surface-bound complementary probes are monitered by surface-plasmon field-enhanced fluorescence microscopy (SPFM). This study may provide a new approach of DNA array fabrication. What's more, the real-time monitoring of interface build-up and the later hybridization tests can be well conducted by the established surface plasmon related optical read-out.

In chapter 5, tethered bilayer lipid membranes (tBLMs) as a model platform for the investigation of various membrane related processes are introduced. The membrane

construction and membrane surface binding events are optically characterized by SPR and SPFS. The electrochemical sealing properties are characterized by EIS. As a first test of the functionality of the membrane assembly, the carrier valinomycin and the channel alamethicin were functionally incorporated and their ion transport are investigated and demonstrated with EIS.

Chapter 6 presents tBLM as a versatile model platform for the study of lipopolysaccharide (LPS) related membrane processes. By incorporating LPS into tBLMs, antigen-antibody assay can be conducted using SPFS with high sensitivity. The effects of antimicrobial peptide V4 on different membrane components have also been electrochemically investigated based on the tBLM platform.

1.2 *Biosensor and surface sensitive techniques*

A biosensor is defined as an analytical device which contains a biological recognition element immobilized on a solid surface and an transduction element which converts analyte binding events into a measurable signal.[1, 5, 6] Biosensors use the highly specific recognition properties of biological molecules, to detect the presence of binding partners, usually at extremely low concentrations. Biological recognition can surpass any man-made device in sensitivity and specificity. This specificity permits very similar analytes to be distinguished from each other by their interaction with immobilized bio-molecule (antibodies, enzymes or nucleic acids). Biosensors are valuable tools for fast and reliable detection of analytes and have reached an importance for scientific, bio-medical and pharmaceutical applications.[7, 8] The advantages that are offered by the ideal biosensor over other forms of analytical techniques are: the high sensitivity and selectivity, low detection limit, good reproducibility, rapid response, reusability of devices, ease of fabrication and application, possibility of miniaturization, ruggedness and low fabrication cost. By immobilizing the bio-recognition element on the sensor surface one gains the advantage of reusability of the device due to the ease of separating bound and unbound species.

The mere presence of the analyte itself dose not cause any measurable signal from the sensor, but the selective binding of the analyte of interest to the biological component. The latter is coupled to a transducer, which responds the binding of the biomolecule[9, 10]. By simple washing steps the non-specifically bound molecules may be removed. Some surface sensitive

detection formats, such as evanescent wave techniques, even make these washing steps redundant. These techniques are relatively insensitive to the presence of analytes in the bulk solution.

The three most frequently used surface-sensitive transduction devices are electrochemical, piezoelectric (acoustic) and optical detectors. While electrochemical sensors respond to changes in the ionic concentration, redox potential, electron transfer rate or electron density upon analyte binding, piezoelectric sensors monitor changes in the adsorbed mass on the sensor surface. A large number of optical biosensors are based on the principles of fluorescence, chemi-luminescence or absorption spectroscopy.

Surface-sensitive techniques provide a vital link, both for the understanding of biomolecular recognition and the development of biosensors. Indeed, surfaces and cell surfaces in particular, are involved in many important biological functions via the cell surface itself (the recognition of foreign bodies by specific receptors located on the cell surface for example) or across the cell membrane (as in the signal transduction from one neuron to another involving complex membrane receptor proteins). These interfaces are central to a variety of biochemical and biophysical processes: triggering of cellular response by neurotransmitter binding, blood coagulation of foreign substances, cellular mobility, etc.

In addition, surface-sensitive techniques bring an inherent advantage over bulk techniques in that they provide real-time binding data. By immobilizing one of the partners of the binding process on the surface of the transducer, the binding of the complement can be followed unperturbed by the presence of free molecules in the bulk. This eliminates the need for lengthy and perturbing separation steps that are required in most bulk techniques.

The techniques that provide surface-sensitivity, as well as being non-destructive and giving in-situ responses can be classified by the method of detection on which they are based:

-electrical:	impedance spectroscopy	(Cornell, et al., 1997, Stelze, et al., 1993, Terrettaz, et al., 1993)
	microphysiometry	(Hope, et al., 1993, yakel, et al., 1993)
-acoustic:	piezoelectric waveguides	(Gizeli, et al., 1996)
-optical:	ellipsometry	(Azzam and Bashara, 1988)
	reflectometric interference spectroscopy	(Piehler, et al., 1997a, Piehler, et al., 1997b)

attenuated total internal reflection infrared spectroscopy	(Axelsen, et al., 1995, Gray, et al., 1996)
surface plasmon resonance	(Duschl, et al., 1996, Keller, et al., 1995, Knoll, et al., 1997)
total internal reflection fluorescence	(Hsieh and Thompson., 1995, Kalb et al., 1992)
optical waveguides	(Duveneck, et al., 1996, Heyse, et al., 1995)

1.3 *Evanescent Wave Sensors and surface plasmon based technique*

Evanescent wave sensors exploit the properties of light totally reflecting at an interface and the presence of an evanescent field of light at this interface. These techniques make use of the exponentially decaying electromagnetic field at the boundary between two media of different optical thickness upon irradiation with electromagnetic waves. Under total internal reflection conditions the decay length of the evanescent field into the optically thinner medium is on the order of the wavelength of the used excitation light. For visible light the field decays within a few hundred nanometers. Only analyte molecules in the evanescent region are probed, which causes the surface sensitive character of such methods. Basically, three different evanescent wave formats are known: planar waveguides, fiber-optics and surface plasmon resonance devices.

A waveguide consists of a planar glass surface with a refractive index higher than the adjacent medium. Under certain conditions light coupled into this waveguide can travel through the sample by total internal reflection. An evanescent field can interact with molecules in the region surrounding the waveguide. Adsorbed analytes change the optical properties of the waveguide and alter the boundary conditions for guiding light in the sample. Hence, the light coupling out of the waveguide can then used to monitor binding reactions at the surface of the waveguide. Fiber-optic sensors utilize the same principle as waveguides, but differ in the experimental geometry.

In surface plasmon technique, however, the evanescent light wave is used to excite the nearly free electron gas in a thin film (~50nm) of metal at the interface. The excitation of these so called surface plasmons, are directly dependent on the optical properties of the

adjacent medium where the deposition of an optical mass on the metal surface will lead to a change in the coupling conditions of the evanescent wave with the plasmons. The excitation of the resulting surface waves gives rise to a field enhancement compared to the intensity of the incident electromagnetic field.[11] This is used to detect mass changes of the film and thus to measure binding processed at the interface. Illumination by laser light can be used to excite the plasmons in metals. Then the system responds to changes in the optical properties of the medium close to the metal film by altering the intensity of the reflected light. For surface sensitive investigation of adsorption and desorption processes on metallic substrates Surface Plasmon Resonance is the method of choice. Commercial instruments are available and are routinely used to measure biomolecular interactions.

1.4 *The necessity of fluorescence labeling*

Generally, sensor formats can be divided into direct and indirect sensors. The first group is capable of detecting the presence of the analyte molecule directly, while the indirect schemes detect the presence of an additional signal. In electrochemically based sensors redox-active labels like ruthenium pyridinium complexes bind to the receptor-target complex and may be detected voltametrically. Sensitivity is an important aspect for the detection of biomolecules. For example, in order to enhance the sensitivity of SPR measurements, the use of attached colloidal particles and amplification of hybridization signal through streptavidin have been reported. Surface Plasmon Spectroscopy (SPS) and piezo-electric techniques are sensitive to changes in the adsorbed mass and thickness on the surface. Labels of large molecular weight like proteins can be used to enhance the sensitivity of the system. Finally, the most prominent optical labels are fluorescent molecules. They allow for highly sensitive detection because the excitation and emission wavelength can be separated.

Analytical methods incorporating fluorescence based detection are widely used in chemical as well as biochemical research due to the extraordinary sensitivity and the favorable time scale on which fluorescence occurs. A number of molecular processes can be observed by monitoring their influence on a fluorescent probe during the fluorescence lifetime, which is typically in the range of 10ns. The impact of this technology in biochemical research has been shown previously. Immunoassays relying on fluorescence detection (fluoroimmunoassays, FIA) may replace established radioimmunoassay if such limitations like relatively high fuorescence background signals can be reduced.

Several photophysical parameters of fluorescent probes have been exploited to monitor analyte binding events. These include fluorescence polarization,[12-14] fluorescence quenching,[15-18] fluorescence enhancement and resonant energy transfer.[19-21] Combining one of these fluorescence schemes with other optical or electrical detection methods of interest can lead to an improvement in the sensitivity and detection limit of these methods. Since fluorescence detection has been utilized extensively in this work, the underlying principles shall be explained in the following.

The development of novel, easy-to-use detection protocols and assay designs rely on the knowledge of kinetic constants of binding reactions. Thus, surface sensitive techniques are essential for the investigation of surface reaction kinetics. Unfortunately, many of the surface sensitive techniques such as Surface Plasmon Spectroscopy lack in their detection sensitivity if low molecular mass analytes are to be detected. Therefore, combinations of surface sensitive optical techniques with fluorescence detection formats were developed. The excitation of evanescent wave techniques has been demonstrated for waveguides and fiber-optic devices.[22-24] Fluorescent molecules close to the sensor surface are excited by the evanescent electromagnetic field. Compared to direct illumination, an enhancement factor of four can be reached.

Recently surface plasmons were used as intermediate states between the incident light and the excited fluorophore in Surface Plasmon Fluorescence Spectroscopy (SPFS) [2-4, 25-29]. Depending on the nature of the metal the plasmon field provides the possibility to enhance the fluorescence signal up to a factor of 80. SPFS allows for probing the presence of fluorescent analytes with high sensitivity and simultaneously provides information about the sensor architecture. From the viewpoint of bio-molecular architectures employed for biosensors, metal surfaces are important with respect to immobilization strategies and are irreplaceable for self assembly of thiol tethered lipids, proteins and nucleic acids. The detection formats for DNA investigated in this study are based on controlled and reproducible formation of monolayers of proteins and DNA on gold and silver films. Therefore the SPFS technique was used to characterize the formation of the supporting matrix and the DNA hybridization.

The excitation of fluorescence in the evanescent field of the plasmons is strongest close to the metal surface. On the other hand the presence of the metal can reduce the observed fluorescence intensity by inducing distance dependent quenching processes like Förster transfer. Excitation and quenching processes exhibit different distance dependencies. An optimal distance to the metal exists at which maximal fluorescence excitation is observed.

Therefore, the experimental design of the sensor surface architecture has to be optimized in order to obtain an efficient and sensitive sensor concept.

Surface plasmon field enhanced technique is particularly suited to study biomolecular interactions where, in addition to its surface specificity, this technique has a very high sensitivity thanks to the possible use of efficient fluorescent labels. The use of this technique to study biomolecular recognition processes, as well as for the development of biosensors, is central to this work.

1.5 *Supramolecular architectures*

The performance of any biomedical device strongly depends on the proper functionalization of its surface. The proper design and synthesis of surface functional groups manipulate the desired active or interactive communication between the device and its biological environment. For the case of biosensors, these criteria reduce to the seemingly "simple" requirements which the sensor surface needs to fulfill: an optimized density of highly selective and specific functional groups for the recognition (and binding) of the analyte molecule of interest must be combined with a matrix that passivates the sensor surface for any unspecific and, hence, undesired interaction between the many other components in the analyte solution and the sensor surface.[30]

The construction of highly organized molecular systems opens up new vistas for the control of matter and the design of novel functional materials. In recent years significant progress was made in their assembly at solid surfaces, which can be directed and monitored in exquisite detail using physical nanoscience methods. Moreover, this approach facilitates integration in environments structured at a higher level.

2 Theory

2.1 *Surface Plasmon Resonance*

The phenomenon of surface plasmons has been known for a long time. The underlying principles and theories are well understood, so that a number of publications can be found which discuss their properties in detail[11, 31-34]. Surface plasmons are surface waves which can be excited at the interface between a metal and a dielectric (as shown in Fig 2.1) and the exact excitation conditions strongly depend on the optical properties of the system. The changes in these properties will lead to altered experimental excitation conditions. This measurable response of the system permits the sensitive monitoring of processes near this interface. Numerous descriptions of successful surface plasmon based sensors can be found and are discussed later.

An important part of this work is based on the excitation of surface waves and the interaction of the associated electromagnetic field within dielectric thin films. The theoretical background of these processes are described in detail in this chapter, since the understanding of electromagnetic waves in matter and their behavior at interfaces is essential for the

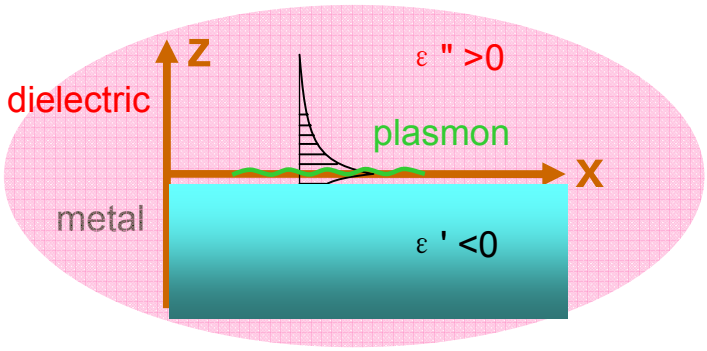

Figure 2.1: Schematic diagram of surface plasmon

following discussion. Fundamental processes like refraction, reflection, transmission and damping of electromagnetic waves at interfaces are considered in general, followed by a discussion of surface plasmon excitation in a two layer system. Finally, the derived model will be extended to multilayer systems and the connection to experimental surface plasmon spectroscopy is made.

2.1.1. Surface Plasmon

Wave-like electromagnetic modes that propagate along an interface between two media and whose amplitudes decrease exponentially normal to the surface are called surface polaritons, i.e. surface electromagnetic modes involving photons coupled to surface electric-dipole and/or magnetic-dipole excitations.

An interface is considered to exist in the xy-plane between two half-infinite spaces, 1 and 2, of optically isotropic mediums which are described by their complex frequency-dependent dielectric functions $\varepsilon_1(\omega)$ and $\varepsilon_2(\omega)$, respectively. S-polarized light (transversal electric TE) propagating along the x-direction possesses only electric field component parallel to the surface (y-direction), and hence is unable to induce a surface charge density and excite surface polaritons. Only p-polarized light (transversal magnetic TM) modes with with components along x and z can result in a periodic surface charge density and induce this interface electromagnetic wave. Of such an electrostatic field is coupled to 'surface photons' a so-called surface polariton is created, the total electric field of which consists of a superposition of the constituting electrostatic and electromagnetic fields.

2.1.2. Plasmon Surface Polaritons at a Noble Metal/Dielectric Interface

The interface between two media of different frequency-dependent, but this time complex dielectric functions is examined.

$$\begin{aligned} \varepsilon_1 &= \varepsilon_1' + i\varepsilon_1'' \\ \varepsilon_2 &= \varepsilon_2' + i\varepsilon_2'' \end{aligned} \tag{2.1}$$

The link between the complex dielectric constant ε and the complex refractive index $(n + i\kappa)$ is given by

$$\begin{aligned} (n+i\kappa)^2 &= \varepsilon' + i\varepsilon'' = \varepsilon \\ \varepsilon' &= n^2 - \kappa^2 \\ \varepsilon'' &= 2n\kappa \end{aligned} \tag{2.2}$$

The real part n is called refractive index whereas the imaginary part κ is the absorption coefficient, i.e. responsible for the attenuation of an electromagnetic wave. The magnetic permeabilities μ_1 and μ_2 are considered to be equal to 1.

As explained above, there only exist surface polaritons for transverse magnetic polarized incident plane waves. Thus, the solution to the problem will have the general form of

$$\begin{aligned} \mathrm{A}_1 &= \mathrm{A}_{01} \cdot \exp\left[i(k_{x1}x + k_{z1}z - \omega t)\right] \\ \mathrm{A}_2 &= \mathrm{A}_{02} \cdot \exp\left[i(k_{x2}x + k_{z2}z - \omega t)\right] \end{aligned} \tag{2.3}$$

with A either being the electric field **E** or the magnetic field **H**. k_{x1} and k_{x2} are the wavevectors in x-directions and k_{z1}, k_{z2} the ones along the z-axis. The numbers 1 and 2 are references to the two media involved for z > 0 and z < 0, respectively. The continuity of the tangential components of **E** and **H** at the surface, i.e. $E_{x1} = E_{x2}$ and $H_{y1} = H_{y2}$ accounts for

$$\begin{aligned} k_{z1} H_{y1} &= \frac{\omega}{c} \varepsilon_1 E_{x1} \\ k_{z2} H_{y2} &= \frac{\omega}{c} \varepsilon_2 E_{x2} \end{aligned} \tag{2.4}$$

On the other hand, inserting equation (2.2) into Maxwell's equations gives

$$k_{x1} = k_{x2} = k_x \tag{2.5}$$

This leads to the only nontrivial solution if

$$\frac{k_{z1}}{k_{z2}} = -\frac{\varepsilon_1}{\varepsilon_2} \tag{2.6}$$

This equation states that surface electromagnetic modes can only be excited at such interfaces where both media have dielectric constants of opposite signs, as has already been shown above. If one of the two media is a dielectric with a positive dielectric constant ε_d then the above relation can be fulfilled by a whole variety of possible elementary excitations if and only if their oscillation strength is large enough to result in a negative dielectric constant ε. For excitations like phonons or excitons the coupling to a surface electromagnetic wave leads to phonon surface polariton or exciton surface polariton modes, respectively. Another type of excitation that can couple to surface electromagnetic waves is the collective plasma oscillation of a nearly free electron gas in a metal around the charged metal ions, called plasmon surface polaritons.

In dielectrics the electrons are bound tightly to the nuclei resulting in a small, positive and real dielectric constant. In metals, however, the electrons are quasi-free and may be moved easily by an external force. The classical Drude model, which considers the electrons to be free, already derives at a highly negative, complex dielectric constant:

$$\varepsilon(\omega) = 1 - \frac{\omega_p^{\,2}}{\omega^2} \tag{2.7}$$

The plasma frequency ω_p usually lies in the UV range for metals. The above equation is valid for frequencies ω from 0 up to a maximum frequency $\omega_{\max}$, which is given by

$$\omega_{\max} = \frac{\omega_p}{\sqrt{1+\varepsilon_d}} \tag{2.8}$$

For metals the dielectric function, ε_m, is in general complex with a negative real part and a small positive imaginary part.

Continuing the above deduction of the very distinct wavevector of a surface plasmon, the wavevectors in the direction of the z-axis can be calculated:

$$k_{zd} = \sqrt{\varepsilon_d \left(\frac{\omega}{c}\right)^2 - {k_x}^2} \quad \text{and} \quad k_{zm} = \sqrt{\varepsilon_m \left(\frac{\omega}{c}\right)^2 - {k_x}^2} \tag{2.9}$$

Finally, with equation (2.12) this leads to the dispersion equation for surface plasmons at a metal/dielectric interface:

$$k_x = k_x' + i k_x'' = \frac{\omega}{c}\sqrt{\frac{\varepsilon_m \cdot \varepsilon_d}{\varepsilon_m + \varepsilon_d}} \tag{2.10}$$

In conclusion, the complex nature of the wavevectors in x- and z- direction leads to an exponentially decaying wave in z and an attenuated wave along the x-axis. A finite propagatin length L_x

$$L_x = \frac{1}{k_x''} \tag{2.11}$$

can be defined, which extremely influences the lateral resolution and is especially important in surface plasmon microscopy applications. For a gold/air interface with $\varepsilon_m = -12 + i \cdot 1.3$ and $\lambda = 632.8\,\text{nm}$ the propagation length is in the range of $L_x = 10\mu\text{m}$.

2.1.3. Excitation of Surface Plasmons

Another aspect of the dispersion relation of surface plasmons is summarized in the following equation:

$$k_{x,SP} = \frac{\omega}{c}\sqrt{\frac{\varepsilon_m \cdot \varepsilon_d}{\varepsilon_m + \varepsilon_d}} \quad \geq \quad \frac{\omega}{c}\sqrt{\varepsilon_d} = k_{x(\max),ph} \tag{2.12}$$

Clearly, one result of this equation is, as already stated above, that the z-component of the surface plasmon wavevector is purely imaginary. Thus, the surface plasmon is a nonradiative evanescent wave with maximum field amplitude at the interface. It decays exponentially into the dielectric and the metal. Another consequence is that a light beam incident from the

dielectric with the maximum wavevectorv $k_{x(\max),ph}$ at the interface cannot excite a surface plasmon with the wavevector $k_{x,ph}$ since its momentum is not sufficiently large.

Figure 2.2 presents these details graphically. Although the light line of free photons (a) approaches asymptotically the dispersion curve of surface plasmons (p) there is no intersection of both curves and the x-component of the waevector of incident light is always smaller than the one for surface plasmons. Among the developed methods to increase the momentum of the light in order to couple to surface plasmons there are for example nonlinear

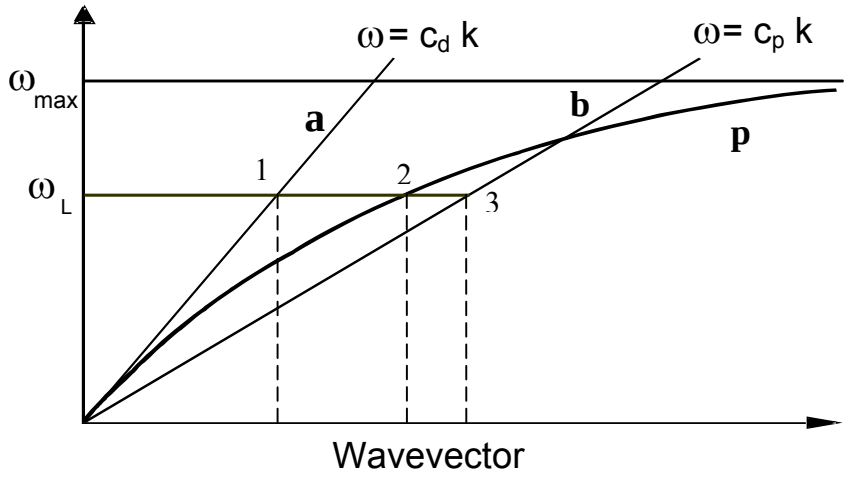

Figure 2.2: Dispersion relation of free photons in a dielectric (a) and in a coupling prism (b) with $n_p > n_d$, compared to the dispersion relation of surface plasmons at the interface between metal and dielectric. At a given laser wavelength ω_L the energy and momentum match of the photons impinging from a dielectric with the surface plasmon is not achieved whereas for the photons incident through a prism, which is increasing the pohotons momentum, it is attained.

coupling or coupling by means of a rough surface. By far the most predominant coupling techniques, however, are the prism coupling and the grating coupling, but only the prism coupling will be discussed in the following.

Prism coupling represents one way of increasing the wavevector of the incident light and hereby the x-component of the wavevector, which only couples to the surface excitation. Figure 2.2 also shows the corresponding dispersion relation if the refractive index of the prism n_p is larger than the one of the dielectric n_d. The momentum is increased, the curve more tilted and therefore at a given laser wavelength ω_l, coupling to surface plasmons (2) can be obtained. However, since at point (3) the momentum of the light beam is too large it has to

be tuned to the one of the surface plasmon by varying the angle of incidence ($k_{x,ph} = |k_{ph}| \cdot \sin\theta_i$).

There exist two different configurations with which to excite surface plasmons by use of a high refractive index prism. The one that was proposed first is the so-called Otto configuration. Here, the laser beam is reflected off the base of a prism (common geometries are half-sphere, half-cylinder or 90° prisms). A gap of low refractive index, less than a few radiation wavelengths thick (for visible light < 2µm) provides for a tunnel barrier across which the evanescent radiation couples from the totally internally reflecting base of the prism to the bound surface field of the surface plasmon. Experimentally, the resonant coupling is observed by monitoring the reflected light beam as a function of the angle of incidence. However, there is a major technical drawback to this type of configuration as one has to fulfill the need of providing a gap of approximately 200nm for efficient coupling. Even a few dust particles can act as spacers preventing a controlled assembly of the coupling system.

Fortunately, there is another method for coupling light to surface plasmons by means of a high refractive index prism – the Kretschmann configuration. In this excitation scheme the light does not couple through a dielectric layer yet, alternatively, through a thin metal layer, which is directly evaporated onto the base of the prism. At the momentum matching condition a surface plasmon is then excited at the interface between the metal and dielectrics, as depicted in figure 2.3.

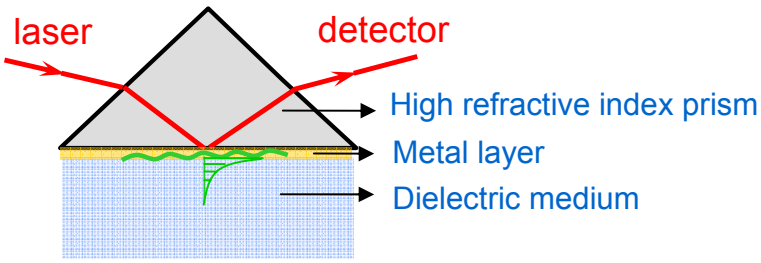

Figure 2.3: Schematic diagram of prism coupling

However, in contrast to the above derived mathematical description the surface plasmons are not restricted to two half-spaces anymore. Quantitatively, one has to take the finite thickness of the metal layer into account, which allows in particular that some of the surface plasmon light is coupled out through the metal and the prism. This new, additional rediative-loss channel, however, can be considered as a minor perturbation to the surface plasmon

electromagnetic wave. In any case, it is clear that there exists an optimum thickness of the metal: taken that the metal film is too thin damping of the surface plasmon wave will occur due to the radiative loss channel back through the metal film and the prism. If the metal layer is too thick the tunnel barrier is too large and only little light will couple to surface plasmons at the metal/dielectric interface. For both, gold and silver, the optimum thickness for a laser wavelength of $\lambda = 632.8\,\text{nm}$ lies between 45nm and 50nm, which can be easily controlled by evaporation.

2.1.4. Surface Plasmon Spectroscopy

As high refractive prisms are used for the excitation of surface plasmons in the examples of figure 2.3, the momentum of the incident light beam in the plane of the interface exceeds the one needed for the excitation. Thus, it is possible to tune the system into resonance by simply changing the angle of incidence, as $k_x = k_0 \cdot \sin\theta_i$. This situation is schematically shown in figure 2.4 (a) and (b).

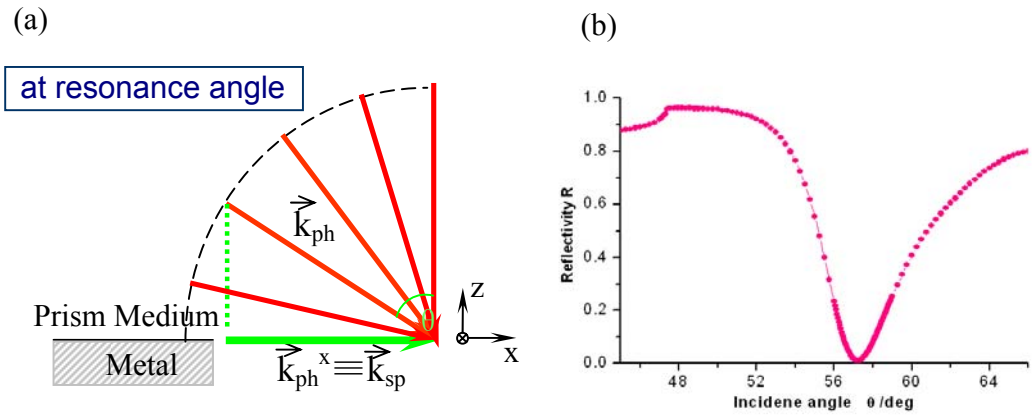

Figure 2.4: (a): The momentum of the incident light beam in the plane of the interface exceeds the one needed for the excitation. Thus, it is possible to tune the system into resonance by simply changing the angle of incidence; (b): A typical angular scan of Surface Plasmon Spectroscopy.

At low angle, the reflected intensity increases, as described by the Fresnel formulas. Then, from a certain angle, the angle of total reflection θ_c, onwards it reaches a plateau. Note, firstly, that the reflectivity before θ_c is rather high, which is due to the evaporated metal film that acts as a mirror reflecting most of the incident light. Secondly, the maximum reflected intensity never reaches unity since the photon energy is partly dissipated in the metal layer.

Lastly, the position of the critical angle only depends on the substrate and superstrate, i.e. prism and water, and is not influenced by any of the intermediate layers. If the projection of $\mathbf{k}_i$ to the interface matches $k_{x,SP}$ resonance occurs and a surface plasmon is excited. This condition is given at the intersection 2 of figure 2.3. Once the system is in resonance surface electromagnetic waves are excited, which can be observed as a dip in the reflected intensity. The minimum is denoted by θ_0 (angle of incidence inside the prism θ_0') and is given by

$$\theta_0' = a\sin\left(\sqrt{\frac{\varepsilon_m \cdot \varepsilon_d}{(\varepsilon_m + \varepsilon_d)\cdot \varepsilon_p}}\right) \tag{2.13}$$

with ε_p being the dielectric constant of the prism. As mentioned above, for real metals there is resistive scattering and hence damping of the oscillations created by the incident electromagnetic field. (If not the surface plasmon resonance would be infinitely sharp and have an infinite propagation length.) The imaginary part of the dielectric constant of the metal causes the damping and the dispersion relation for surface plasmons can be rewritten as:

$$k_x = k_x' + ik_x'' = \frac{\omega}{c}\sqrt{\frac{(\varepsilon_m' + i\varepsilon_m'')\cdot\varepsilon_d}{(\varepsilon_m' + i\varepsilon_m'') + \varepsilon_d}} \approx \frac{\omega}{c}\sqrt{\varepsilon_d}\left(1 - \frac{\varepsilon_d}{2\varepsilon_m'}\right) + i\cdot\frac{1}{2}\frac{\omega}{c}\frac{\varepsilon_m''(\varepsilon_d)^{3/2}}{(\varepsilon_m')^2} \tag{2.14}$$

Thus, the shift of surface plasmon is inversely proportional to ε_m' whereas the width, which is related to k_m'', depends on ε_m'' and is inversely proportional to $(\varepsilon_m')^2$. While at first sight it might therefore be beneficial to have a small imaginary part of the metal dielectric constant the real part is of even higher significance. Clearly, silver with the higher absolute value of ε_m' and the smaller imaginary part can be identified having a much sharper resonance.

The advantage of surface plasmon spectroscopy lies in its sensitivity to surface processes due to its evanescent field. This means, on the one hand, that a change of the dielectric, i.e. ε_d in equation (2.12), leads to either a drop or an increase of the wavevector of the surface plasmon resonance, depending on the sign of the change. For example, the resonance angles θ_0 for air and water can be found at low and high angles, respectively. On the other hand, the addition of a thin layer ($d << 2\pi / k_{zd}$) of a second dielectric to the already existing triggers a changed surface plasmon response and the corresponding shift of the dispersion curve is equivalent to a change of the overall refractive index integrated over the evanescent field. The net effect is a slight shift of the surface palsmon dispersion curve as can be seen in figure 2.5 (a) for an additional layer with higher refractive index than the one of the reference dielectric

medium. At the same energy $\hbar\omega$ of incident light the dispersion curve of the surface plasmon intersects with the light line at a higher wavevector (point 4 in fig 2.5 (b)). In terms of the reflectivity as a function of the angle of incidence the minimum is therefore shifted to higher angles.

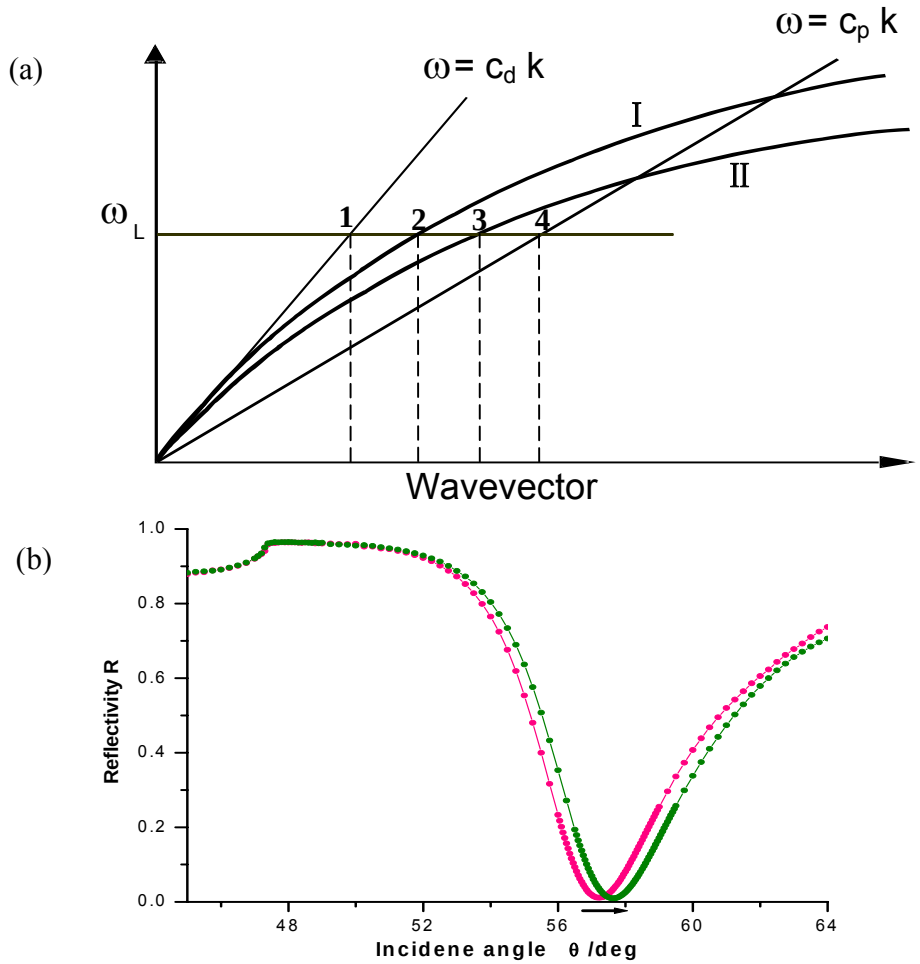

Figure 2.5: (a): Dispersion relation of surface plasmons at the interface between metal and dielectric before (Ⅰ) and after (Ⅱ) the absorption of an additional layer, compared to the dispersion relation of free photons in a coupling prism; (b) Comparison of full angular scans before and after the absorption of an additional layer. Note the increase of the maximum resonance angle.

When adding a layer to the existing system two parameters are of interest, the refractive index and the thickness of the film. In order to separate these two parameters at least two distinct features that are correlated to the addition are needed. Yet, the surface plasmon resonance only provides one. Consequently, only a set of parameters (n, d) can be derived from such reflectivity curve, provided both parameters are unknown. If one of them is known the other one can be obtained from fits to the curves. Several methods resolve the ambiguity

of this problem. Firstly, resonance curves can be taken at different laser wavelengths. This method, however, does not resolve the ambiguity of the unknown dispersion behavior of the refractive index of the coating. Secondly, the contrast of the experiment can be varied, i.e. the surface plasmon curves are measured in at least two solvents with different refractive indices. The minimum shift does not depend on the absolute value of *n* but rather on the contrast, i.e. the refractive index difference between the layer and the surrounding medium. In both of the presented methods a set of at least two different curves of *n* vs. *d* is obtained, the intersection of which determines the correct refractive index and thickness of the additional layer. Finally, if the aim of the study and the chemicals allow for the preparation of thick films, waveguide modes can be excited. If the film is sufficiently thick and an adequate number of modes is available, *n* and *d* can be evaluated separately and even the indicatrix may be obtained.

2.2 *Fluorescence*

2.2.1 Fluorescence phenomenon

Fluorescence is a well characterized phenomenon which describes the emission of photons from molecules that undergo a transition from an electronically excited to the ground state.[35, 36] Fluorescence is a result of a three-stage spontaneous process that occurs in certain molecules (generally polyaromatics hydrocarbons or heterocycles) called fluorophores or fluorescent dyes. Fluorophores often exhibit strongly delocalized electrons in conjugated double bonds or aromatic systems. The molecular processes during absorption and emission

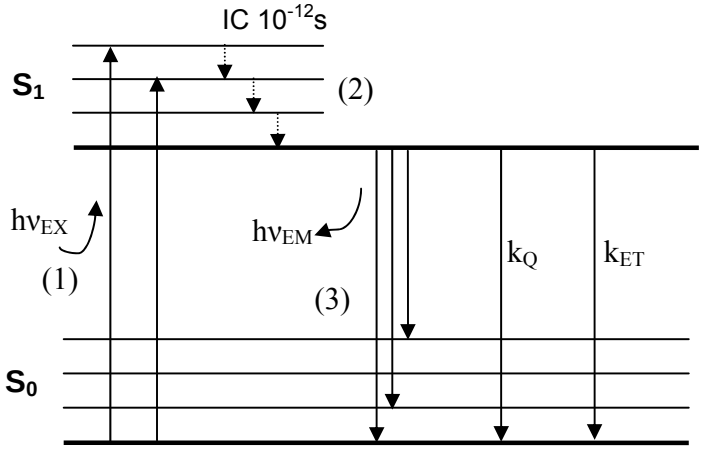

Figure 2.6: Jablonsky diagram illustrating the electronic and vibrational states of a fluorophore and processes during photon absorption and fluorescence emission.

of photons are illustrated by the schematic Jablonsky energy level diagram shown in Figure 2.6.

A fluorophore may exist in several electronic states, two of which are depicted here (S_0 and S_1). These levels are described by the spin multiplicity of the state, so that e.g. singlet and triplet states can be found, depending on how the orbits of the molecule are populated and how the spins of the electrons are paired. Triplet states are not involved in the fluorescence mechanism itself, so that we concentrate on the singlet levels only. At each of these electronic levels the fluorophore can exist in a number of vibrational levels, which are populated according to the Boltzmann distribution law. Hence, at room temperature and a given energy spacing of the levels most of the molecules will be present in the lowest vibrational level of S0. Upon the adsorption of a photon of energy $h\nu_{EX}$, the fluorophore is excited from the ground state to one of higher vibrational levels of S_1 or S_2 (not shown) in the time scale of 10^{-15}s. During this time, it undergoes changes such as conformational change and interacts with its environment in many different ways (stage 1, cf. Fig 2.6). Consequently, the energy from the excited state (S1') is partially dissipated, yielding a relaxed singlet excited state (S1) from which the fluorescent emission occurs. Finally, the reconversion to S0 from S1 emits a photon of energy hνEM (stage 3, cf. Fig 2.6). Not all of the excited species return to the ground state via fluorescent emission. Many other processes can occur with their respective rate constants, such as fluorescence resonance energy transfer (FRET, k_{ET}), intersystem crossing (ISC, k_{ISC}), internal conversion (IC, k_{IC}) or collisional quenching (CQ, k_{CQ}), which can depopulate molecules from S1. They all influence the fluorescence quantum yield Φ, which is the ratio of the number of fluorescence photon emitted to the number of photon adsorbed. Due to energy loss during the excited state lifetime, $h\nu_{EM}$ is smaller than $h\nu_{EX}$. Therefore, the emitted fluorescence photons have longer wavelength (lower frequency) than the photons responsible for the excitation. This wavelength difference is fundamental to the sensitivity of fluorescence techniques, because it allows the emitted photons to be easily distinguished from excitation photons, leading to the possibility of a very low background in fluorescent studies.

A fluorescence emission spectrum is recorded by holding the excitation wavelength constant and detecting the fluorescence intensity over a range of emission wavelengths. In contrast to this, an excitation spectrum is recorded by holding the emission wavelength constant and scanning over a range of excitation wavelength. With a few exceptions the excitation spectrum of a fluorescent species in dilute solutions is identical to the absorption

spectrum. Under the same conditions, the fluorescence emission spectrum is independent of the excitation wavelength.

2.2.2 Fluorescence quenching and self-quenching

Quenching refers to any process that causes a reduction in the quantum yield of a given fluorescence process. Quenching can be either collisional or static. The collisional quenching occurs if the quencher comes into contact with the excited fluorophore during the fluorescence lifetime and causes the dye to return to the ground state without emitting a photon, described by the Stern-Volmer Equation:

$$I_0 / I = l + k_q[Q]\tau \tag{2.15}$$

Where *Io* is the fluorescence intensity in the absence of quencher, *I* is the intensity in the presence of the quencher at concentration *[Q]*, k_q is the rate of collisional quenching, and *ô* is the observed lifetime. Static quenching is due to the formation of a ground state complex between the fluorescent molecule and the quencher with formation constant *Kc*, described by:

$$I_0 / I = l + k_c[Q] \tag{2.16}$$

One of the interesting phenomena about fluorescence is that multiple labelling of a molecule with a fluorophore does not always leads to an increase in fluorescent intensity. The brightness of a fluorophore is defined as the product of the extinction coefficient (ε) and the quantum yield (Φ):

$$Brightness = \varepsilon \times \Phi \tag{2.17}$$

If we conjugate *N* fluorophores to a molecule, the overall brightness can be described as:

$$Brightness = \varepsilon \times \Phi \times N \tag{2.18}$$

In many cases, as *N* increases, the overall brightness does not increase linearly and sometimes even decreases. This is known as a phenomenon of inter-conjugate "self-quenching" of the conjugated fluorophores.[37] Different fluorophores differ in their ability to self-quench. It has been confirmed that the more hydrophobic the fluorophore, the lower the ratio of fluorophores/conjugate to which quenching will occur. Intra-conjugate "self-quenching" is also observed if conjugates are densely packed. Generally, self-quenching is considered as a result of excited-state interactions (collisional quenching), or, of the formation of non-fluorescent complexes (e.g. dimers).

2.2.3 Fluorescence resonance energy transfer

Resonance energy transfer, often known as fluorescence resonance energy transfer (FRET) or Förster energy transfer, is the transfer of excitation energy from a donor to an acceptor. An important consequence of this transfer is that the emission of light by the donor is greatly reduced. The acceptor may or may not be fluorescent. FRET is a distance-dependent interaction where the energy transfer occurs typically over a distance of 1-10 nm, making it useful over distances comparable with the dimensions of biological macromolecules (e.g. the

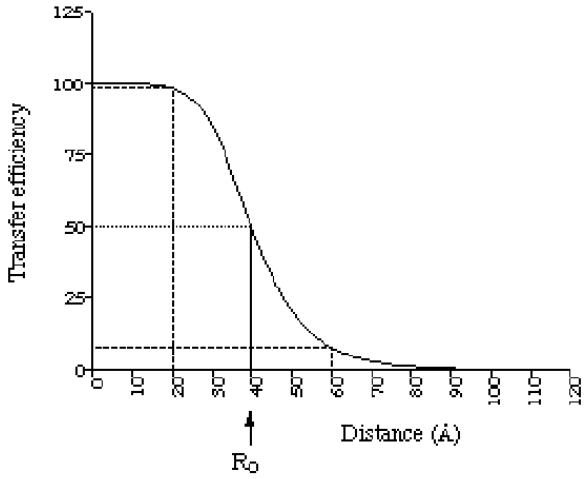

Figure 2.7: Schematic example of energy transfer efficiency dependent on the distance of donor-acceptor.

molecular beacon technology.[38] The efficiency of FRET is a key factor, which is dependent on the inverse sixth power of the intermolecular separation (R) of dipole-to-dipole interaction given by the following equation:

$$\Phi_{ET(R)} = \frac{R^6}{R^6 + R_0{}^6} \tag{2.19}$$

The distance at which energy transfer is 50% efficient (i.e., 50% of excited donors are deactivated by FRET) is defined by the Förster radius (*R0*).

2.2.4 Photobleaching

A typical fluorophore can undergo a finite number of excitation-relaxation cycles prior to photochemical destruction. This process is often referred to as photobleaching, photofading or photodestruction. For a photostable fluorophore, e.g. tetramethylrhodamin, photobleaching occurs after about 10^5 cycles. In contrast, fluorescein photobleaches very easily. Generally speaking, the photobleaching involves the generation of reactive oxygen molecules, thus it is

sometimes useful to introduce antioxidants or to use anoxic conditions. On the other hand, the rate of the photobleaching is often proportional to the intensity of illumination. Therefore, a simple practical way to overcome this is to reduce the time or the intensity of the excitation radiation.

2.2.5 Fluorescence at the metal/dielectric interface

In respect to the evanescent field excitation mechanism used in this work, it is very important to examine the behavior of fluorophores in the vicinity of metals. A fluorophore close to a surface can be excited by the evanescent wave. For that, the fluorophores should be placed within the decay length of the evanescent field for excitation, which is typically several tens to hundreds of nanometers for applicable wavelengths. On the other hand, metals can also act as generic quenchers. The excited state of the fluorophore can couple to the broad band of electronic states in bulk metal and relax by essentially heating up the metal slightly.

If a dye is positioned at a distance within 10 nm to the metal surface, the non-radiative decay of fluorescence is the dominating process. The excitation is assumed to be dipole-to-dipole, if it is due to the excitation of an electron-hole pair (exciton) in the metal. The standard Förster model gives a R-6 dependence of the transfer rate to the seperation distance (cf. Figure 2.8), due to the co-effect from both near fields of the donor molecule and the acceptor molecule. However, the distance dependence of energy transfers involving a dye and a surface (could be rough) can be greatly compromised to be R-3 ~ R-4 dependent due to the integration over the enlarged number of effective acceptor sites. The transferred energy dissipated by the metal is converted into heat.

At an intermediate-distance regime (a few nm up to ~20 nm), a significant fraction of excited fluorescence couples back to surface plasmon polaritons, by fulfilling momentum-matching conditions. Unless SPP modes can be converted again into photons by a coupling-prism or a grating, which allows for the monitoring of SPP decay channel 49, it represents a significant loss of fluorescence yield.

At sufficient separation distances (>20 nm), free emission of the dyes dominates. However, the fluorescence yield cannot be directly obtained unless two effects are considered. Firstly, the fluorescence emission oscillates as the distance increases, since the metal reflects the fluorescence field and introduces light interference. Secondly, the excitation source, i.e., the evanescent field weakens as the distance increases.

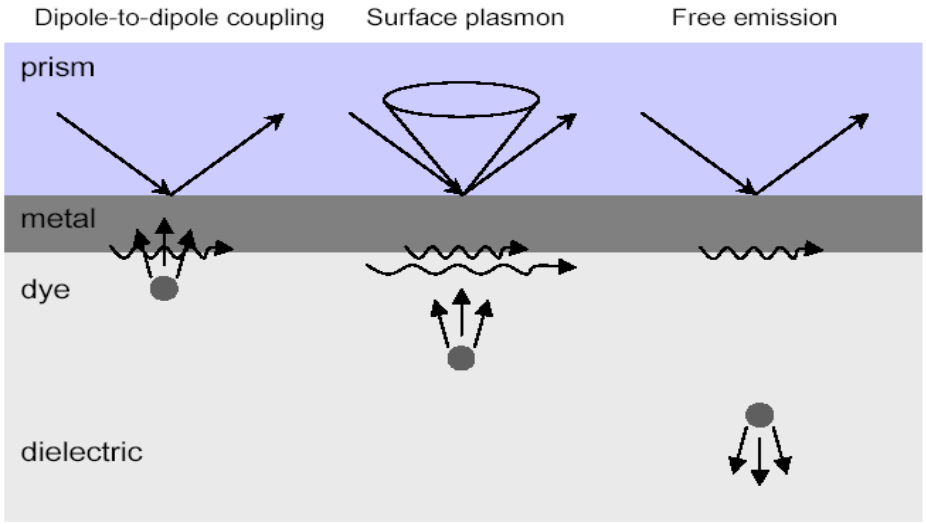

Figure 2.8: Schematic drawing of a fluorophore positioned close to a metal/dielectric interface. Different fluorescence decay channels take place at different fluorophore/metal separation distances.

2.3 *Electrochemical impedance spectroscopy (EIS)*

Electrochemical impedance spectroscopy (EIS) is a well established method of characterizing various electrical properties (i.e., conductivity, capacitance, and inductance) of materials and their interfaces with electronically conducting electrodes. Additionally, it has been used to investigate the dynamics of bound or mobile charge in the bulk or interfacial regions of solid or liquid material: ionic, semi-conducting, mixed electronic-ionic, and even insulators (dielectrics).

Recently, EIS have shown to have great potential in the fields of biosensor application as a transducer principle, especially in those systems that are composed of functional proteins as actual sensing element on lipid bilayer platform[39-42].

EIS is a transient technique, the system under study is perturbed by a pulse or a periodical signal and the relaxation (i.e., the response as a function of time) resulting in a new equilibrium or steady state is analyzed to extract the desired kinetic information. Typically an EIS measurement is combined with theoretical considerations on an appropriate physical model of the studied system. By fitting the measured impedance spectra into equivalent circuit derived from the model, the resulting resistance and capacitance values give a well description of the system in terms of the applied physical model.

2.3.1 Base of electrochemical impedance spectroscopy (EIS)

Like resistance, impedance is measure of the ability of a circuit to resist the flow of electrical current (Fig. 2.9). It differs from resistance in two significant aspects. First, it's an alternating current (AC) phenomenon; second, it is usually specified at a particular frequency. The impedance is normally measured by applying an AC potential to an electrochemical cell and measuring the current through the cell. The response to a sinusoidal potential is sinusoid at the same frequency but shifted in phase. Through the measured resistance by the impedance spectroscopy with AC voltage, the information about the conductivity can be obtained.

The excitation or input signal expressed as a function of time is:

$$E(t) = E_0 \cos(\omega t) \tag{2.20}$$

where $E(t)$ is the potential at time t, E_0 is the amplitude of the signal, and ω is the radial frequency $\omega = 2\pi f$ and f is a frequency expressed in Hertz (Hz). In the linear system, the response or output signal $I(t)$ with amplitude I_0 is shifted in phase

$$I(t) = I_0 \cos(\omega t - \varphi) \tag{2.21}$$

The response of electrical circuits to an alternating current can be described in terms of the impedance (Z) defined as:

$$Z = \frac{E(t)}{I(t)} = \frac{E_0 \cos(\omega t)}{I_0 \cos(\omega t - \varphi)} = Z_0 \frac{\cos(\omega t)}{\cos(\omega t - \varphi)} \tag{2.22}$$

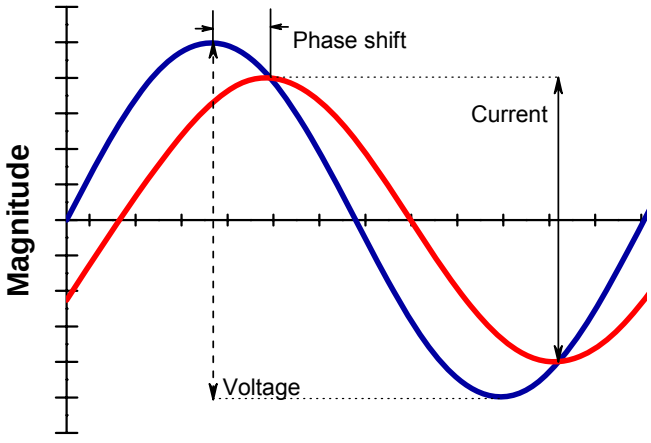

Figure 2.9: Current and voltage as a function of time. The current response is shift in time

The impedance is therefore expressed in terms of a magnitude, Z_0, and a phase shift φ. Using Euler's relationship, the impedance is then represented as a complex number

$$Z = \frac{E(t)}{I(t)} = \frac{E_0 \exp(j\omega t)}{I_0 \exp(j\omega t - j\varphi)} = Z_0 \exp(j\varphi) \\ = Z_0(\cos\varphi + j\sin\varphi) \tag{2.23}$$

The impedance vector in complex plane (Nyquist impedance plot) is described by two components, real, Z', and imaginary, Z''. The real part of Z' is in the direction of the real axis x, and the imaginary part the y axis. An impedance $|Z| = Z' + jZ''$ can be plotted in the plane with either rectangular or polar coordinated, as shown in Figure 2.10.

Here the two rectangular coordinate values are given as follows:

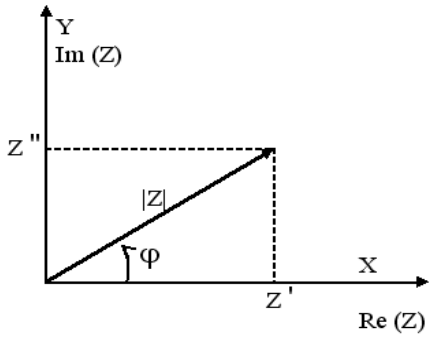

Figure 2.10: The impedance Z plotted as a planar vector using rectangular and polar coordinates

Here the two rectangular coordinate values are given as follows:

$$\begin{aligned} \mathrm{Re}(Z) &= Z' = |Z| \cdot \cos\varphi \\ \mathrm{Im}(Z) &= Z'' = |Z| \cdot \sin\varphi \end{aligned} \tag{2.24}$$

with the phase angle

$$\begin{aligned} \mathrm{Re}(Z) &= Z' = |Z| \cdot \cos\varphi \\ \mathrm{Im}(Z) &= Z'' = |Z| \cdot \sin\varphi \end{aligned} \qquad \varphi = \tan^{-1}(Z''/Z') \tag{2.25}$$

and the impedance can be calculated from the vector length |Z|

$$|Z| = \sqrt{(Z')^2 + (Z'')^2} \tag{2.26}$$

2.3.2 Impedance spectra

Data from impedance measurement can be expressed either in the Nyquist plot, the Bode plot, or in the admittance plot. The impedance Z, and the admittance Y, are usually described by complex numbers, whose real and imaginary parts represent their components for a phase delay of 0° and 90°, respectively.

- **Nyquist-Plot**

A Nyquist plot is a parametric plot of the real and imaginary parts of the transfer function in the complex plane as the frequency is swept over a given range. If one plots the real part on the X axis and the imaginary part on the Y axis, the representation of the impedance at each frequency can be obtained, meaning that each point on the plot is the impedance at a particular frequency. Figure 2.11 shows a typical Nyquist plot for a resistor and capacitor in parallel.

The disadvantage of the Nyquist plot is that it can not provide information on frequency. Therefore, it is impossible to tell what frequency was used for a particular impedance. For this reason, Nyquist plots are usually supplemented with other plots.

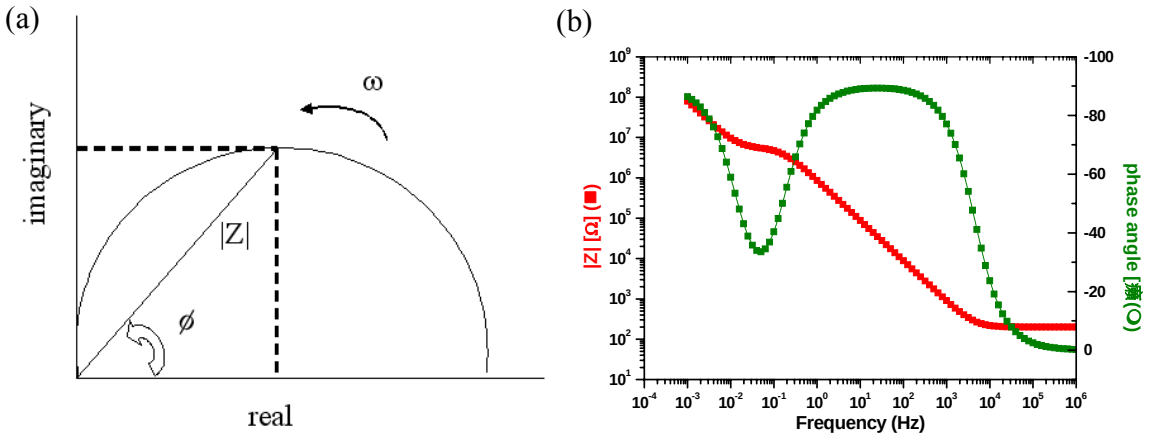

Figure 2.11: (a) The Nyquist plot provides a representation of impedance at each frequency; (b) Bode plots can examine both phaseshift and imdepance as a function of frequency.

- **Bode-Plot**

To well characterize an impedance, Z, it's better to specify both its magnitude, $|Z|$, and phase, θ, as well as the frequency, f, at which it was measured. These three parameters are often plotted on what is known as Bode plot. In a Bode impedance plot, the absolute magnitude of impedance is plotted against the frequency f or logarithm of frequency, whereas a graph of phase angle versus the frequency or logarithm of frequency gives a Bode phase

plot. In this case, the log of frequency is plotted as X- axis and both the absolute value of the impedance |Z| and phase shift are plotted on the Y- axis. Usually, the Nyquist plots and Bode plots are used together to understand a sensor element's transfer function.

- **Complex Admittance (frequency normalized): High-frequency bias**

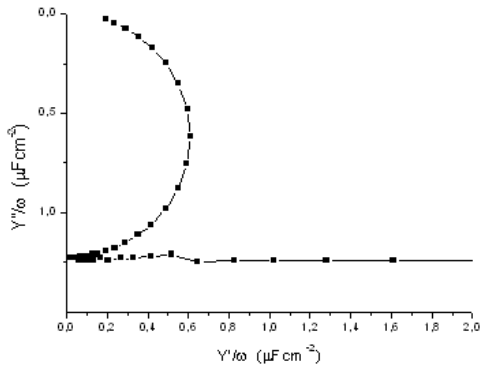

Figure 2.12: Schematic of complex admittance. The capacitance of the system can be read directly from the graph

The advantage to analyze AC circuit in terms of the admittance Y, which is the inverse impedance Y=1/Z, and therefore represents a kind of conductance (Fig.2.13). The complex admittance Y and impedance Z hold the relation

$$Y = \frac{1}{Z} = Y' + jY'' = G + G_a + j\omega C \tag{2.27}$$

The real part and imaginary part of adminttance can be obtained from

$$\begin{aligned} Y' &= \frac{Z'}{(Z')^2 + (Z'')^2} \\ Y'' &= \frac{-Z''}{(Z')^2 + (Z'')^2} \end{aligned} \tag{2.28}$$

Variation of the AC frequency, ω (*f*), results in different figure in complex plane corresponding to changes in the ratio between real and imaginary components of the admittance.

Equivalent circuits

Interpretation of EIS data is based on the combination of equivalent circuits composed of resistors and capacitors. The real and imaginary parts of the impedance and admittance of basic circuit elements are given in Table 2.1.

	Z_r[a]	$\|Z_i\|$[b]	Y_r[c]	Y_i[d]
Resistor	R	0	1/R	0
Capacitor	0	$1/\omega C$	0	ωC
RC parallel	$R/1+\omega^2R^2C^2$	$\omega CR^2/1+\omega^2R^2C^2$	1/R	ωC
RC series	R	$1/\omega C$	$R\omega^2C^2/1+\omega^2R^2C^2$	$\omega C/1+\omega^2R^2C^2$

Table 2.1: Definition of the impedance Z and the admittance Y

Notes: a means real part of the impedance
b means absolute value of the imaginary part of the impedance
c means real part of the admittance
d mean imaginary part of the admittance

3. Experimental Methods

3.1 Instrument

A major part of this work is based on the characterization of surface processes like adsorption and desorption of analytes onto and from dielectric thin films of known architecture. Surface plasmon spectroscopy (SPS), as a prominent optical method, permits the detection of such processes on metal substrates and is therefore described in detail. It's microscopic formation Surface Plasmon Microscopy (SPM), and furthermore the experimental construction of simultaneous fluorescence detection in Surface Plasmon Fluorescence Spectroscopy (SPFSs), Surface Plasmon Fluorescence Microscopy (SPFM), and Surface Plasmon Fluorescence Spectrometry (SPFSm) are presented. Finally the combination of surface plasmon methods with electrochemical probing is elucidated.

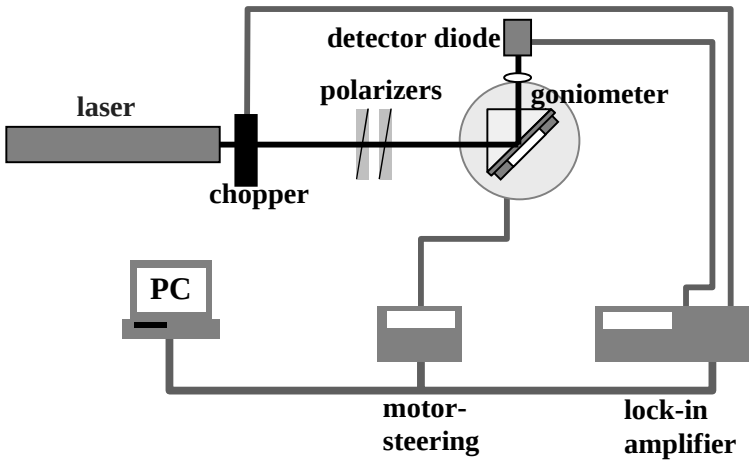

Figure 3.1: Schematic diagram of Surface Plasmon Spectroscopy (SPS) setup

3.1.1 SPR

The schematic of the set-up is depicted in Figure 3.1. The beam of a Helium-Neon (HeNe) laser (Uniphase, 5 mW, λ = 632.8 nm or 5mW, λ = 543 nm) passes through a chopper (frequency = 1331 Hz) that is connected to a lock-in amplifier (EG&G). The modulated beam then passes through two polarizers (Glan-Thompson), by which the intensity of the incident light and the plane of polarization of can be adjusted. A programmable shutter is installed such as to constantly block the laser (unless data points are recorded), thus minimizing the photo-bleaching effect of the fluorescent dyes. Next, the beam is reflected off the base of the

coupling prism (Schott, LaSFN9, n = 1.85 @ 633 nm) and is focused by a lens (f = 50 mm, Owis) onto a collection lens and a photo-diode detector, connected to the lock-in amplifier. The prism/sample and the photo-detector are mounted onto a 2 phase goniometer (Huber) which can be rotated in $\Delta\theta$ = 0.001deg steps by the use of the connected personal computer. According to the reflection law the angular position of the optical arm holding the detection unit (detector motor) is adjusted during the measurements. The sample is mounted onto a table which can move and tilt to allow for the optimal adjustment of the setup.

As explained, a resonance spectrum (also referred to as angular scan curve) is obtained by reflecting a polarized laser beam off the base plane of a prism and plotting the normalized reflected intensity versus the incidence angle. The range of the angles measured is important, since the resulting scan should cover the total reflection edge and most of the resonance minimum. The obtained scan curve can then be fitted according to Fresnel's formula in order to calculate the thickness of the metallic and dielectric layers. The calculations based on the transfer matrix algorithm are carried out with the computer software Winspall 2.0, which was developed in our group. Parameters that are included in the fitting procedure are the measured reflectivity, the incidence angle, thickness and dielectric constants of the layers as well as the used laser wavelength and the geometry of the coupling prism. By iterative optimization of the parameters the simulated reflectivity curve is fitted to the measured scan curve and the optical constants of the involved layers are determined.

Since the thickness and dielectric constant of the layers cannot be determined independently, one of the parameters has to be measured by use of other techniques. However, if the refractive index of the prism is known, the refractive index of a used solvent can be easily calculated by determining the critical angel. The angular position of the total reflection edge is only dependent on the optical constants of both outer media.

The adsorption of an additional layer (e.g. a self assembled monolayer of thiols on gold) changes the optical properties of the dielectric next to the metal and results in a shift of the resonance minimum as schematically depicted in figure 3.2. This shift can be theoretically considered by introducing an additional layer into the Fresnel simulations while the parameters of the other layers are held constant. Such a comparison between the simulated parameters before and after the adsorption process allows for the determination of the thickness or refractive index of a layer adsorbed to the metal.

Not only static measurements of interface can be obtained but also the online monitoring of processes near the surface is possible and kinetics of surface reactions can be recorded. For this purpose the incidence angle is fixed at a position for which the measured scan curve exhibits a linear slope (e.g. at 30% reflectivity) and the detected reflectivity is recorded with time. The reflectivity at this fixed incidence angle is increased if the resonance is shifted

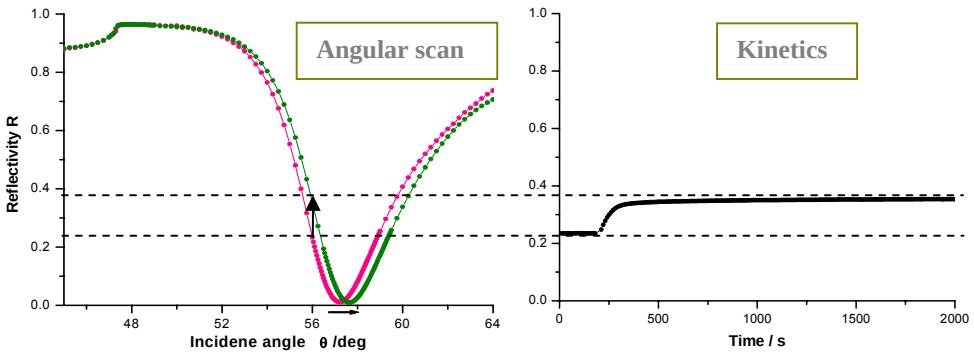

Figure 3.2: Angular scan curves and associated kinetic measurement. Note that the reflectivity is increased if the incidence angle is fixed and the resonance curve is shifted.

towards higher angles and the detected shift represents a linear time dependence of the optical properties of the investigated system. Here it is assumed that the dependence of the resonance minimum shift on optical changes is linear, too. In addition, it is assumed that the shape of the scan curve in the considered region is not changed upon adsorption of the additional layer. Otherwise the linear response of the kinetic curve would be lost.

3.1.2 Surface Plasmon Microscopy (SPM)

Surface plasmon microscopy (SPM) can also be realized for monitoring laterally structured surfaces[43, 44] or for parallel read-out of arrayed samples[45-48]. Two modifications in the set-up are necessary:

1) Use a beam expander by an 10× objective lens, an 25 µm pinhole and a collimating lens to get clean, parallel and expanded beam for illuminating a larger surface area,

2) Replace the photo-diode detector to be a monochromatic CCD camera (Hamamatsu, C5405-01) equipped with an imaging lens (EHD, Zoom70 or Rodenstock f = 50 mm). The CCD camera is connected to a frame-grabber card for image transmitting.

By employing a surface plasmon microscope (SPM)[43, 44, 49] approach and the related data-analyzing software one can document the interfacial build-up visually in real time and can gain quantitative information about the binding reactions, especially in the assay of DNA arrays.

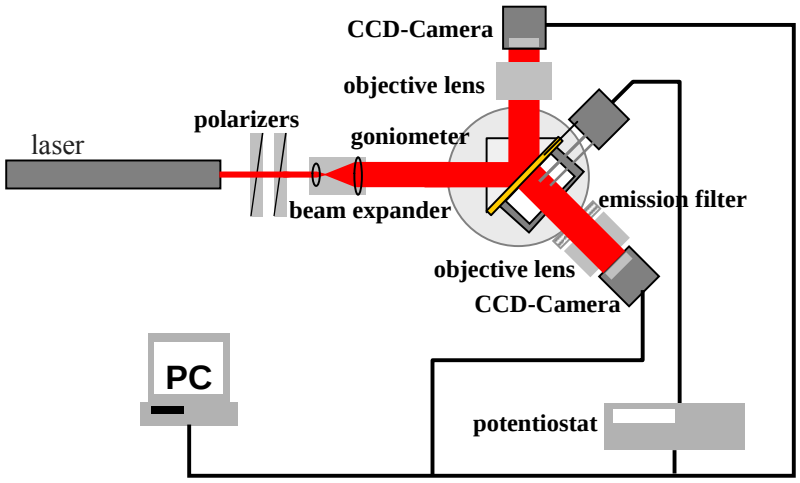

Figure 3.3. Schematic experimental setup in the Kretschmann configuration for surface plasmon microscopy and surface plasmon field-enhanced fluorescence microscopy, combined also with electrochemistry element.

3.1.3 Surface Plasmon Fluorescence Spectroscopy (SPFSs), Microscopy (SPFM) and Spectrometry (SPFSm)

Fluorescent molecules near surfaces can be excited by the evanescent field of surface plasmons. The fluorescence detection unit is mounted towards the base of the prism, rotating together with the prism (sample) at θ, while the photo-diode detecting the reflected light rotates at 2θ. The fluorescence emission from the sample surface is collected by a lens (f = 50 mm, Owis) and passes through an interference filter (λ = 670 nm, λ = 10 nm, LOT, 80% transmittance) into a photomultiplier tube (PMT, Hamamatsu), which is connected to a photon-counter (Agilent) unit via a home-built electronic protection unit and a programmable switch box. Note that the interference filter is specifically designed for commercially versatile fluorophores such as Cy5 (Cyanine 5, from Amersham Pharmacia Inc.) and illuminant nanoparticles (from Qdot). Occasionally, a neutral filter (attenuator) is used to attenuate the

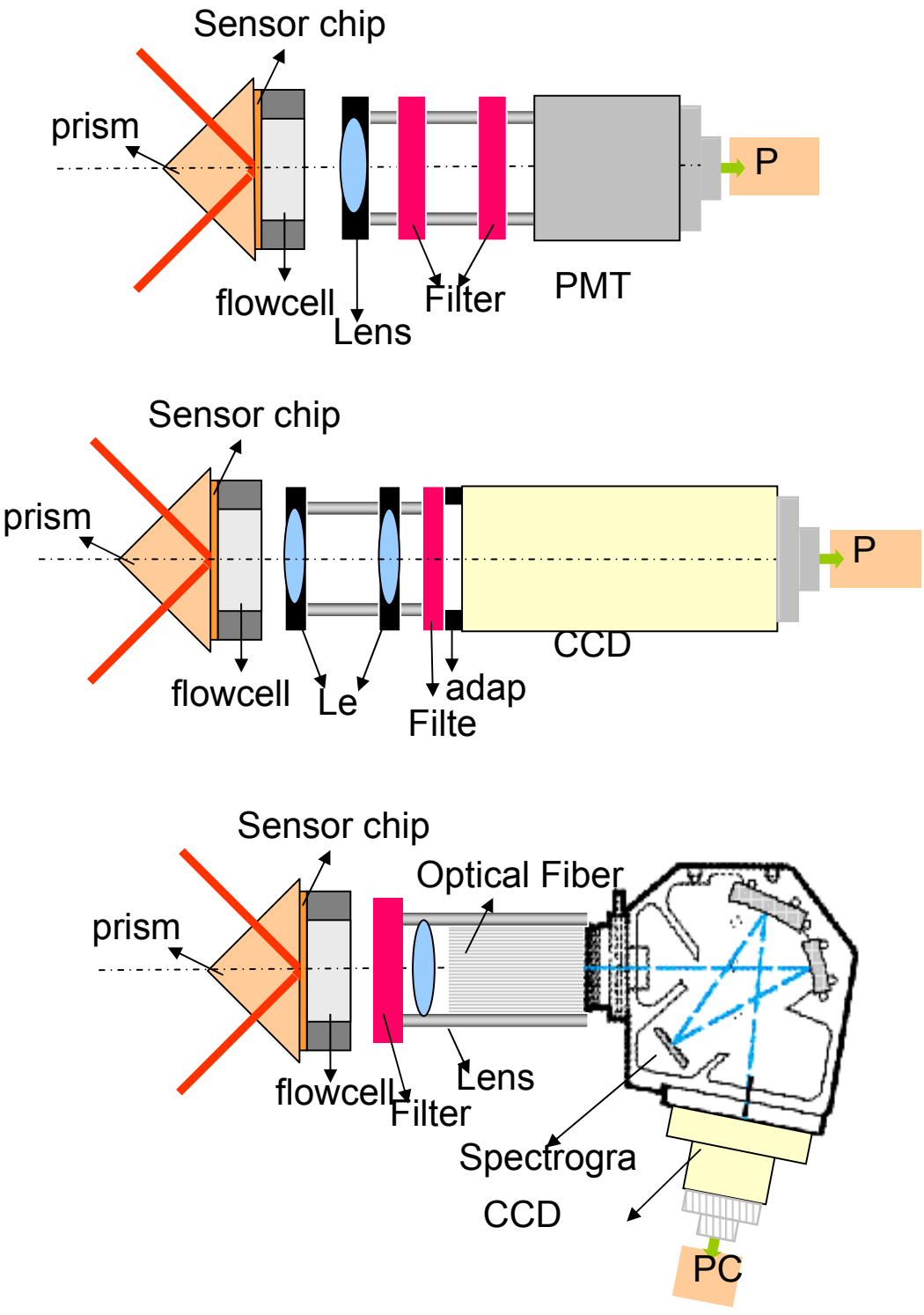

Figure 3.4: Schematic drawing of SPFSs, SPFM, SPFSm

fluorescence in the case of strong fluorescence intensity, in order to keep the PMT working in

the linear input-versus-output range (<1~2 million counts per second).

For the fluorescence microscopy, a particularly sensitive color CCD camera (Kappa optoelectronics, Gleichen, Germany) is mounted to that part of the goniometer that rotates the

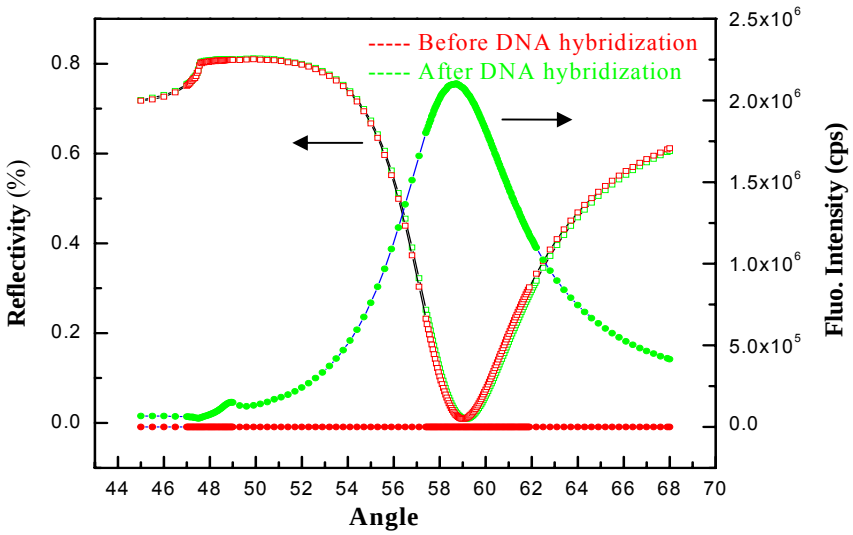

Figure 3.5: Typical SPFS curves before and after adsorption of fluorescence DNA target oligonucleotide.

sample cell (θ) thus ensuring that the camera always looks at a fixed angle normal to the substrate surface. To avoid the collection of scattered and transmitted laser light, an excitation filter (Omiga Opticals Inc, USA) is placed between the flow cell and the CCD camera. The software package KAPPA Image Base Control (Kappa optoelectronics, Gleichen, Germany) allows for the recording of the fluorescence images. The camera is operated at an internal temperature of T = 25°C and with an integration time of Δ t = 20 sec.

For the surface-plasmon field-enhanced fluorescence spectrometry the experimental setup is modified in such a way, that the color CCD camera is exchanged by a fiber optics cable collecting the fluorescent light, which passes through the excitation filter and is focused by a lens sitting in front of the fiber optics collection head. The fluorescence light is then remitted to a MS125 spectrograph unit (Thermo Oriel, Stratford, CT, USA). Data collection and processing are performed with a PC running the software “Andor MCA V2.62” from Andor Technologies (Belfast, Northern Ireland).

3.1.4 SP methods in combination with electrochemical measurement

Since electroactive materials are used in this work, and their interfacial properties depend heavily on the degree of oxidation (p-doping) or reduction (n-doping, therefore, the combination of electrochemistry with surface plasmon spectroscopy (ESPR) is a powerful tool for probing extremely small changes of various films at the metal/solution interface.
Some details of the electrochemical flow cell design are shown in Figure 3.6a. The body of this single-compartment cell is made of Teflon, with a silica glass slide as cover window. The cuvette has two holes for inserting the reference and the counter electrodes, respectively, as well as an inlet and an outlet for liquid sample exchange and rinsing. Electrochemistry was conducted using an AutoLab (Type II μAutolab) potentiostat, with a coiled platinum wire used as counter electrode and an Ag/AgCl electrode as reference.

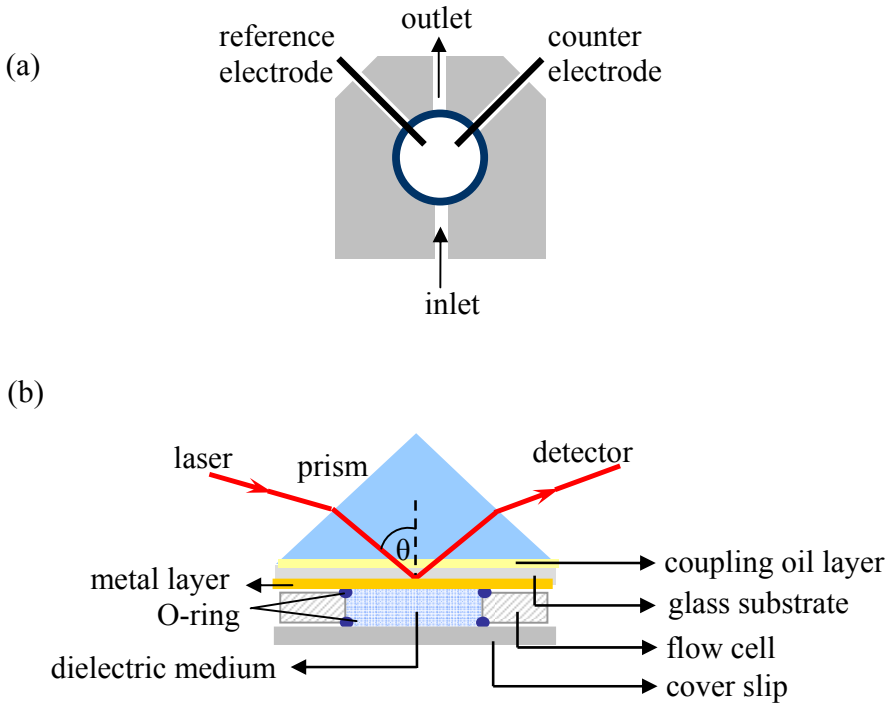

Figure 3.6: (a) Cross-section of the cell body with liquid inlet and outlet for fluid handling and with platinum wire as counter and Ag/AgCl as reference electrode. (b) Schematic of flow cell attached to prism coupling configuration.

Figure 3.6b also gives a schematic cross-section of the flow cell attached to the prism coupling unit in the Kretschmann configuration for surface plasmon excitation. The flow cell is sealed by Viton O-rings against the multi-electrode sensor chip, on top of which a prism (LaSFN9, ε = 3.4069 @ λ = 633 nm) is index matched for surface plasmon resonance

spectroscopy (SPR), surface plasmon microscopy (SPM) and surface plasmon fluorescence microscopy (SPFM) measurements.

Shown in Figure 2 is a simplified schematic diagram of the combination.

3.2 *Surface Functionalization*

3.2.1 Self-assembled monolayers on Au surface

Molecular self-assembly phenomena are widely seen in surface modification strategies. Selfassembled monolayers (SAMs) are highly ordered molecular assembles of long chain alkanes that chemisorb on the surface of solid materials[50-53]. The structure of SAMs, effectively two-dimensional crystals with controllable chemical functionality, makes them ideal model systems for the investigations and applications in wetting, adhesion, corrosion, protein adsorption, surface functionalization, micro-/nano- fabrications, etc. SAMs of alkanethiolates on gold (RSH/Au) are one of the most attractive system for their: (i) ease of fabrication; (ii) degree of perfection; (iii) chemical stability; (iv) availability of materials; and (v) flexibility in chemistry and thus surface functionality. SAMs of alkanethiolates on Au (111) form quasi-crystalline structures for n>6 with the driving forces coming from lateral van del Waals forces and the strength of the sulphur-gold bond.

The incorporation of a wide variety of groups both in the alkyl chain and at the chain terminus of the thiol derivatives and their use as building blocks allow for the fabrication of (laterally patterned) supramolecular interfacial architectures. Formation of mixed (binary) SAM is a strategy to build sensor surfaces as it has been reported extensively. This strategy helps to build up structurally well-defined functional monolayers and enables convenient tuning of functional group density.

In this work, SAMs were prepared by simply dipping the Au substrates into the thiol solution. Experimentally, thiol solutions are prepared at a net thiol concentration of 500 μM in absolute ethanol (99%). Freshly coated Au substrates are immersed in the thiol solutions, then sealed and kept overnight at room temperature. Subsequently, the substrates are removed, rinsed thoroughly with ethanol and blown dry by a stream of nitrogen. The prepared substrates were stored under Argon atmosphere until use.

3.2.2 Bioconjugation of QDs and DNA

The conjugation of target DNA oligonucleotides to the quantum dots was prepared as follows: 100 µL Qdot™ streptavidin conjugates (2 µM) were diluted to a volume of 1.8mL by adding quantum dot reaction buffer. The reaction mixture was completed by the addition of 200 µL oligonucleotides in $H_2O_{bidest.}$ (20 µM). The mixture was stirred in the dark for 2 h at RT. The excess of non conjugated oligonucleotides was removed by a gradual concentration of the reaction mixture with 30 kDa Nanosep® centrifugal concentrators and a subsequent resuspension with PBS buffer. This procedure also exchanged the quantum dot reaction buffer with a PBS buffer, which was suitable for the performed hybridization experiments. The quantum dot – DNA conjugates were stored in PBS buffer at 4°C in the dark.

3.2.3 DNA microarray preparation

The preparation of the SPFM and SPFS sensor surfaces emanated from LaSFN9 glass slides, which were coated with a mixed Ag/Au (37/8 nm) metal layer. Firstly, a mixed self-assembled monolayer (SAM) of a biotinylated thiol derivative and a short chain OH-terminated thiol used as a diluent at a mixing ratio of 1:9 was assembled at the Ag/Au substrates, generating a binding matrix optimized for the formation of a streptavidin monolayer via the specific recognition to the biotin moieties. The streptavidin monolayer was then created on top of this SAM by incubation of the surfaces with 500nM streptavidin in PBS. The bound streptavidin exposes biding sites to the aqueous phase of the cuvette which allows for the assembly of an oligonuleotide catcher probe layer.

For the preparation of a micro array sensor, microspots of biotinylated probe DNA oligonucleotides were spotted on the center of this streptavidin monolayer surface with a pitch of 350µm between the spots by using an ESI SMA™ Arrayer. The micro spotting is thereby accomplished by direct surface contact between the printing substrate and a delivery module that contains an array of pins that serve to transfer the biochemical samples to the surface. Once the microarrayed slides are freshly prepared, they will be kept in a desiccator until used.

3.2.4 Electrochemically Addressable Functionalization of a DNA Biosensor Array

Thin films of Cr (d = 2 nm) and Au (d = 44 nm) were evaporation-deposited onto a high refractive index glass slide (LaSFN9/Schott) at a pressure of about 5×10^{-5} Pa in a commercial evaporation set-up (Biemtron, Japan) using a mask for the definition of the electrodes on the sensor chip. For simplicity, we prepared only 4 gold stripes each of which acts as a working electrode as well as an addressable detector unit. The size of each electrode was 10 mm in

length and 700 μm in width. Neighboring electrodes were separated by a (glass) gap of 200 μm.

For the preparation of the addressable DNA array, the gold coated multi-electrode sensor chip was mounted to the combined SPM and SPFM setup and connected to a potentiostat. The PEG thiol solution in PBS was applied to the sensor chip surface for 20min in order to allow for the formation of a compact, hydrophilic thiol layer on this 4-electrode system, protecting the surface from unwanted adhesion of molecules introduced during the following processing steps. In order to start the thiol desorption, one of the electrodes was connected to the potentiostat as working electrode and a constant potential of E = –1.1V was applied for 8mins followed by a thorough rinse on order to completely remove the PEG thiol producing a fresh, clean gold surface. Biotinylated thiols were then allowed to self-assemble at this bare Au electrode, resulting in a monolayer with a thickness after rinsing of ca. d = 1.5 nm (calculated with n = 1.50). Next, a streptavidin monolayer of ca. d = 4.0 nm in thickness was formed by specific binding from solution to the biotin-sites at the surface. Finally, a layer of biotinylated single-stranded oligonucleotide strands was assembled on the surface by occupying the free binding sites of the streptavidin monolayer. The same preparation cycles were then applied to the other electrodes until a total of three sensor elements were functionalized, each with a different oligonucleotide capture probe, while one electrode remained covered with a PEG thiol monolayer as reference as it is schematically depicted in Figure 3. Each interfacial reaction step was characterized by SPR or SPM measurements.

3.2.5 Small unilamellar vesicles (SUVs) preparation

For preparation of liposomes with either mono-lipid or mixed lipid composition, the lipids were firstly dissolved in chloroform thorouly to assure a homogeneous mixture of the lipids. Then the organic solvent was removed by using a dry stream of argon in a fume hood. The lipid film was thoroughly dried to remove residual organic solvent by placing the vial or flask on a vacuum pump overnight. Hydration of the dry lipid film/cake was accomplished simply by adding proper amount of MilliQ water to the container of dry lipid and agitating. During the 1 hour hydration period with vigorous shaking and mixing, the temperature of the hydrating medium was kept at 60 degree which is above the gel-liquid crystal transition temperature of the used lipids. This allows the lipid to hydrate in its fluid phase with adequate agitation.

In order to prevent the membranes from fouling and improves the homogeneity of the size distribution of the final suspension, lipid extrusion was utilized to prepare Small unilamellar vesicles (SUVs). Firstly, lipid suspension was freeze– thawn for 5 times. Secondly, the solution was extruded through 0.05 Am polycarbonate membrane filters 20 times using a mini-extruder syringe device (Avanti Polar Lipids).

4. SPR, SPM, SPFM and SPFSm studies of DNA biosensor arrays

4.1 *Motivations*

The need for rapid, multiple, and reliable analytical methods and formats for the detection of binding events between surface immobilized ligands and high specific biomolecules from solution gained increasing importance in the light of unsolved questions and problems in gene therapy and mutation studies. This initiated tremendous research activities in the field of sensor conception and development addressing these problems[54, 55].

Since the introduction of commercial instruments, especially the BIAcore setups, Surface plasmon resonance (SPR) spectroscopy has become widely used in the fields of chemistry and biochemistry for the characterization of biological surfaces and to monitor binding events. Despite many examples documented in the literature for the wide application area[56-58], sensitivity enhancements of these sensors have to be achieved, as their present limit of detection, as well as their applicability for multiple detections at one surface, is insufficient for diagnostic medical applications. Efforts to enhance the sensitivity of the SPR technique have been made especially by combining it with fluorescence spectroscopy[3, 59].

In this work, a concept was recently introduced for the sensitive detection of hybridization reactions between surface-attached oligonucleotide catcher probes and chromophore-labeled complementary target strands approaching the interfacial binding matrix from solution[25, 60]. We could show that the kinetic rate constants, k_{on} and k_{off}, as well as the affinity constant, K_a, between strands with base sequences exhibiting different mismatches could be evaluated even in low concentrations at an excellent signal-to-noise level. The basis of this new concept is the combination of surface plasmon field enhancement and fluorescence spectroscopy. By this approach, the resonant excitation of an evanescent surface plasmon mode (PSP) can be used to excite the fluorophores chemically attached to the target molecules. Upon binding to the probe DNA strand at the metal/solution interface, the chromophore reaches the strong optical fields that can be obtained in PSP resonance giving rise to significant enhancement factors. The emitted fluorescence photons are monitored and analyzed in the usual way to give information about the behavior of the analyte itself. The use of fluorescence detection schemes in combination with the resonant excitation of surface plasmons has been shown to

increase the sensitivity for bioanalyte monitoring considerably[2]. Similar to the above-mentioned, the measurement and interpretation of different surface plasmon resonance intensities caused by different thicknesses of surface-bound layers has led to the introduction of the so-named surface plasmon microscopy[44, 49]. In this work, surface plasmon fluorescence techniques are applied to a microscopy format for the characterization of laterally structured samples. Furthermore, the concept is also extended to surface plasmon fluorescence spectroscopy (SPFS), which counts the number of photons and monitors the information of the binding event only in terms of a fluorescence intensity, to a true spectroscopic format, which is able not only to give the fluorescence intensity but also records the emission wavelength, i.e., the spectral information of the attached fluorophores.

In this new detection approach, called surface plasmon fluorescence microscopy (SPFM) and spectrometry, quantum dots (QDs) were used as fluorescent probes. Quantum dots are small, inorganic, semiconducting nanocrystals that possess unique luminescent properties. As fluorescent probes, QDs have several advantages over conventional organic dyes. Their emission spectra are narrow, symmetrical, and tunable according to their size and material composition, allowing closer spacing of different probes without substantial spectral overlap. Moreover, they exhibit excellent stability against photobleaching. Most significantly, they display broad absorption spectra, making it possible to excite all QDs simultaneously with a single excitation light source[61, 62].

In the work presented here, SPFM and SPFSm are used to realize the parallel detection of hybridization reactions taking place at a whole microarray of individual sensor spots by using a highly sensitive color CCD camera as the recording element. The camera takes images of the fluorescence intensities emitted from each sensor element arranged on the chip surface in a matrix format using a microarray chip writer preparation protocol[63]. This way, a large number of individually functionalized spots can be monitored simultaneously. For simplicity, we here show a study of an array of 3×4 spots of three different probe oligonucleotide sequences and their mixtures.

4.2 *SPFSs, SPFM, and SPFSm studies on spotted microarrays*

4.2.1 Materials

Streptavidin-conjugated quantum dots (Qdot) were purchased from Quantum Dot Corp. (Hayward, CA). These dots (2 μM) were supplied in a 50 mM borate buffer, pH 8.3. The

quantum dot reaction and coupling buffer contained 50 mM sodium borate, pH 8.3, with 2% (m/v) BSA and 0.05% (m/v) sodium azide. All hybridization experiments were performed in a standard PBS buffer containing 150 mM sodium chloride. Streptavidin was purchased from Sigma-Aldrich (St. Louis, MO). The biotinylated and OH-terminated thiols used for the preparation of the SPFS surfaces were synthesized in our laboratory. Highly purified salt-free oligonucleotides were obtained from Research Biolabs (Singapore). Nanosep centrifugal concentrators were purchased from Pall Life Sciences (Ann Arbor, MI). Microarray spots were printed using an ESI SMA arrayer (Ontario, Canada), and the whole process was controlled by a PC running the software Chopwriter Compact Professional Arrayer from Virtek Technologies (Waterloo, ON, Canada).

The probe and target DNA sequences used in this study are given in Table 1. All oligonucleotides were biotin tagged at their 5'-end. In addition to 15 thymine residues used as a spacer, the sequences exhibited 15 nucleobases as the particular recognition sequence. The recognizing nucleotides of P1 and P2 were fully complementary with the 15 bases located at the 3'-end of T1 and T2. The biotin anchor group attached to the probe, and target oligonucleotides facilitated their immobilization to the surface-bound straptavidin monolayer either on a sensor surface or on a quantum dot. The conjugation of target DNA oligonucleotides to the quantum dots was performed as follows: 100 μL of Qdot streptavidin conjugates (2 μM) was diluted to a volume of 1.8 mL by adding quantum dot reaction buffer. The reaction mixture was completed by the addition of 200 μL of oligonucleotides in H_2O (20 μM). The mixture was stirred in the dark for 2 h at room temperature. The excess of nonconjugated oligonucleotides was removed by a gradual concentration of the reaction mixture with 30-kDa Nanosep centrifugal concentrators and a subsequent resuspension with PBS buffer. This procedure also exchanged the quantum dot reaction buffer with a PBS buffer, which was suitable for the hybridization experiments. The QD-DNA conjugates were stored in PBS buffer at 4 °C in the dark.

The preparation of the SPFS surfaces emanated from LaSFN9 glass slides, which were coated with a laminated Ag/Au (37/8 nm) metal layer. First, a mixed self-assembled monolayer (SAM) of 10% biotinylated thiol derivative and 90% OH-terminated thiol (Figure 4.1) used as a diluent at a mixing ratio of 1:9 was assembled at the Ag/Au substrates, generating a binding matrix optimized for the formation of a streptavidin monolayer via the specific recognition of the biotin moieties. The streptavidin monolayer was then created on top of this SAM by incubation with 500 nM streptavidin in PBS. The bound streptavidin

exposes free biotin biding sites to the aqueous phase of the cuvette that allows for the assembly of an oligonuleotide catcher probe layer.

Table 4.1: (a) Nucleotide sequences of the probe and target single stranded DNAs used for the experiments; (b) Possible hybridizations.

(a)

Name	Nucleotide Sequence
P1	5'-Biotin-TTT TTT TTT TTT TTT GCA CCT GAC TCC TGT-3'
P2	5'-Biotin-TTT TTT TTT TTT TTT TGT ACA TCA CAA CTA-3'
P3	5'-Biotin-TTT TTT TTT TTT TTT TAG TTG TGA TGT ACA-3'
T1	5'-Biotin-TTT TTT TTT TTT TTT ACA GGA GTC AGG TGC-3'
T2	5'-Biotin-TTT TTT TTT TTT TTT TAG TTG TGA TGT ACA-3'

(b)

Possible hybridizations	Number of miss-match bases
P1↔ T1	MM0
P1↔ T2	MM14
P2↔ T1	MM14
P2↔ T2	MM0
P3↔ T1	MM14
P3↔ T2	MM11

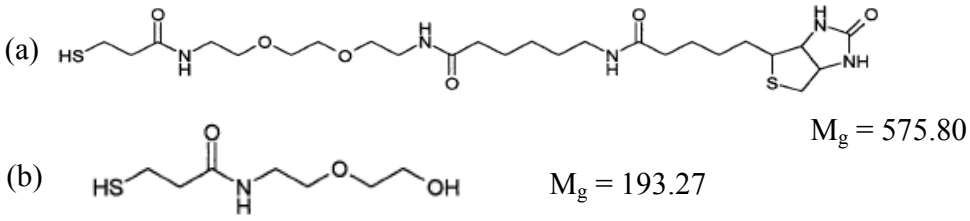

Figure 4.1: Structure formula of the biotinylated thiol (a) and OH-terminated thiol (b) employed in the preparation of the mixed self-assembled monolayer (SAM) which is capable of binding a monolayer of streptavidin.

For the preparation of a microarray sensor, 12 microspots of biotinylated probe DNA oligonucleotides were spotted on the center of this streptavidin monolayer surface with a pitch of 350 μm between the spots by using an ESI SMA Arrayer. The microspotting is thereby

accomplished by direct surface contact between the printing substrate and a delivery module that contains an array of pins that serve to transfer the biochemical samples to the surface.

The solution for the analysis of target DNA sequences contained the corresponding QD-DNA conjugates, QD_{565}-T1 and QD_{655}-T2. The QD-conjugated target DNA sequences have 15 nucleobases complementary to their respective probe strands P1 and P2. Both quantum dot populations, QD_{565} and QD_{655}, could be excited with a green HeNe laser line $\lambda = 543$ nm), and the emitted fluorescence photons were recorded at $\lambda = 565$ nm and $\lambda = 655$ nm, respectively.

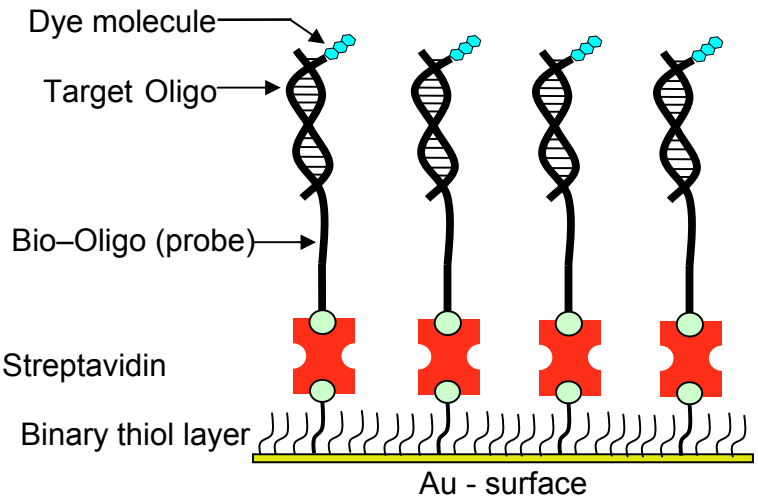

Figure 4.2: Schematic presentation of the sensor surface architecture: Onto an evaporated gold film a binary SAM of two thiols (OH-thiol and biotinylated thiol) was formed, which supported a streptavidin protein layer. Biotinylated oligonucleotides were finally immobilized and the hybridization reaction was monitored by measuring the fluorescence signal of he labeled target oligo.

4.2.2 Test of QD-DNA conjugates for their suitability in SPFS

As this work is based on the technique of surface plasmon enhanced fluorescence spectroscopy, experiments showing the suitability of QD-DNA conjugates for this technique had to be conducted as a basic step.

The conjugation of CdSe/ZnS core-shell quantum dots to DNA was done via the extreme strong streptavidin/biotin interaction (as shown in Figure 4.3). For this purpose, streptavidin-coupled QDs were purchased from Q-Dots Inc. 5'-Biotinylated single-stranded DNA

sequences (target DNA sequences) were applied to these QDs. After removal of nonbound excess DNA via ultrafiltration, pure QD-DNA conjugates could be attained. Via a combination of fluorometry for the determination of QD concentrations and UV spectroscopy for the quantitative determination of the attached DNA, a rough characterization of the conjugates showed a ratio of ~10 DNA sequences being coupled to one quantum dot.

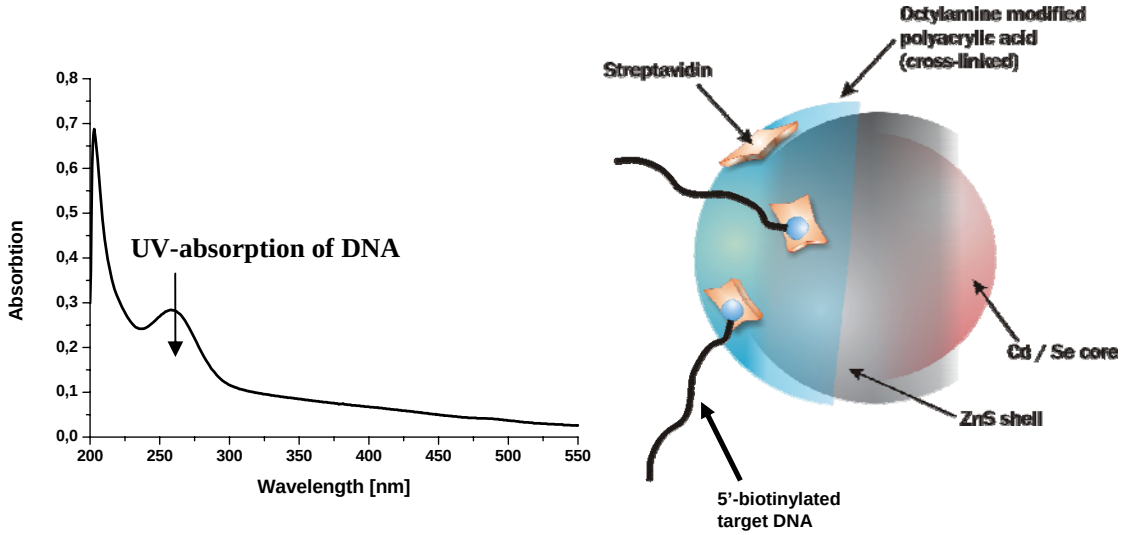

Figure 4.3: (a) Spectrum of UV-absorption of DNA and
(b) schematic representation of DNA conjugated core/shell QDs

For the basic SPR and SPFS experiments with these QD-DNA conjugates, samples of 20 nM QD-DNA conjugates in PBS were applied to the sensor surfaces in a standard SPFS setup.

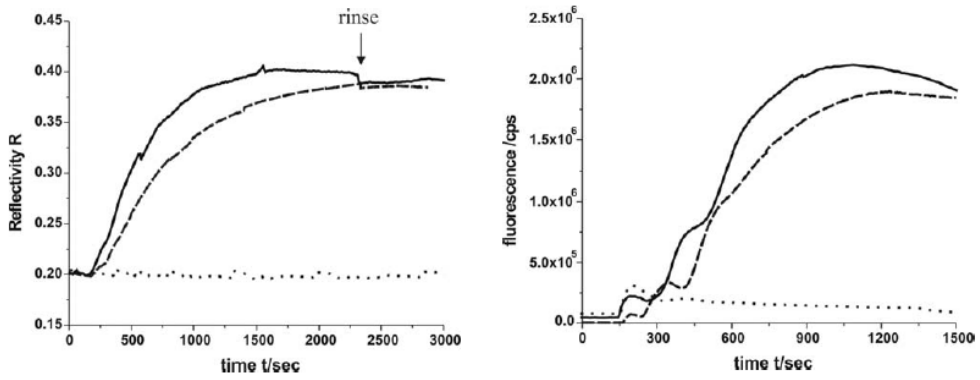

(a) (b)

Figure 4.4: SPR (a) and SPFS (b) measurements of the hybridization reactions of QD_{655}-T1 with P1 (full curve), QD_{565}-T2 with P2 (dashed curves) and QD_{655}-T1 with a surface containing no probe DNA (dotted curve).

The results of these experiments are summarized in Figure 4.4. Figure 4.4a shows the SPR signals generated by hybridizing two different QD-DNA conjugates (QD_{655}-T1 and QD_{565}-T2) with their corresponding complementary probe DNA matrixes (P1 and P2). A clear hybridization of QD-conjugated target DNA with the respective surface-bound probe DNA can be seen. The height of the hybridization signal (ΔR = 0.18 for QD565-T2/P2 and ΔR = 0.20 for QD_{655}-T1/P1), which would be about ΔR = 0.015 in case of a single 30-mer target DNA strand, shows that a relatively big mass must be attached to the target DNA strand. The unspecific binding of QD-DNA conjugates with the bare surface matrix of the sensor (shown for QD_{655}-T1 in Figure 4.4) and with noncomplementary probe DNA strands is very low.

The fluorescence signal generated by the target DNA-bound QDs once they are close enough to the sensor surface to be within the evanescent tail of the surface plasmon field is shown in Figure 4.4b. Both QD-DNA conjugates show a high fluorescence signal for the case of specific probe/target DNA hybridizations. A fluorescence signal deriving from unspecific interactions between the QD-DNA conjugates and the sensor is visible but low enough to allow for a clear discrimination of specific and unspecific binding events. Taking both the reflectivity and fluorescence signals, which result from a specific binding of complementary probe DNA with their corresponding QD-target DNA conjugate, the suitability of the described conjugation system for its use in SPR and SPFS could be demonstrated.

4.2.3 Surface Plasmon Enhanced Fluorescence Microscopy with an Oligonucleotide Array

Following these basic experiments, we investigated the possibility of conferring the system to a SPFM setup. The sensor surface was assembled in the same way as described above except for the layer of biotinylated probe DNA strands. This layer was spotted in a 3×4 microarray format. The arrangement of the resulting 12 spots and the composition of different probe DNA sequences is schematically depicted in Figure 4.2A. Rows 1 and 3 of the array consist of four spots of alternating P1 and P2 while row 2 holds spots with a 1/1 mixture of P1 + P2 and spots with P3, a probe DNA sequence that functions as a negative control because of its 14 mismatching bases for T1 and T2 DNAs.

After positioning the sensor array near the SPR reflectivity minimum, which corresponds to the angle of incidence for which the highest surface plasmon enhanced fluorescence intensities can be obtained, the QD-DNA conjugates were injected to the system. In a first series of experiments, the injection of a 20nM PBS solution of each of the two QD-DNA

samples was done sequentially with a rinsing step in between. The up-path in Figure 4.5 shows the results one obtains from this step-by-step addition experiment. An injection of QD_{565}-T2 resulted in the observation of green fluorescent spots, which were located exactly at the positions where the P2 target DNA and the P1 + P2 mixture were spotted on the microarray sensor (Figure 4.5b). All spots containing no P2 probe DNA remained dark. Subsequently, the second QD-DNA sample, QD_{655}-T1, was applied to the system. The red fluorescence of the QD_{655} could now be observed at the spots were P1 was located on the microarray (Figure 4.5c). Furthermore, the spots containing P1 + P2 changed their color from green to yellow. This is due to the RGB color addition of the green fluorescence caused by P2 hybridized QD_{565}-T2 and the red fluorescence arising from P1 hybridized QD_{655}-T1. Only the spots with P3, the probe DNA that is fully mismatching with both, T1 and T2, did not show any fluorescence signal. A slight red fluorescent background signal could be seen in this experiment, which originated from QDs excited by the evanescent surface plasmon field in the bulk phase. However, even without rinsing, this background fluorescence is low enough to allow for a clear visualization of the selective hybridization reaction of both QD-DNA populations with their respective array-bound complementary probe DNA sequences.

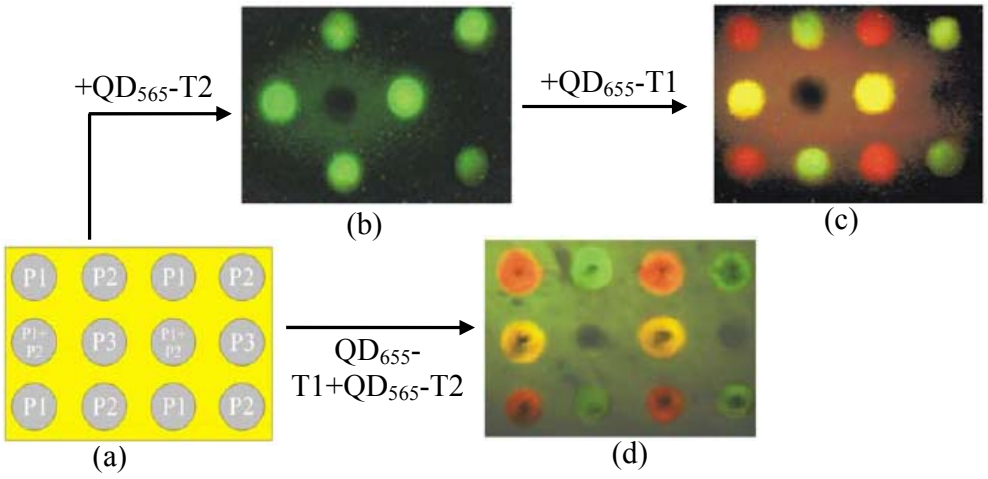

Figure 4.5: SPFM images of micro array sensor surface: (a) Schematic arrangement of different probe DNA spots on the gold/silver/SAMs micro array sensor surface; (b) and (c) Sequential injection of 20nM PBS solution of QD_{565}-T2 and QD_{655}-T1 conjugates, respectively, into the flow cell (2 min injection time each; integration time of the color CCD: 20sed); (d) Injection of a 1:1 mixture of a 20nM PBS solution of QD_{565}-T2 and QD_{655}-T1 (2 min injection time each; integration time of the color CCD: 20s)

In a second set of experiments, a 1:1 mixture of both QD-DNA conjugates was injected into the flow cell. After a reaction time of 2 min, the image given in Figure 4.5d could be seen. Equivalent to the step-by-step addition of the two QD-DNA conjugates, each target DNA hybridized with its complementary probe DNA sequence on the corresponding microarray spot of the sensor surface. Even the P1 + P2 probe DNA mixtures showed the same GB color addition of green and red fluorescence resulting in a yellow signal spot. This experiment showed clearly that a decomposition of mixed QD-DNA populations on the microarray and the qualitative analysis of the single conjugates via SPFM can be achieved.

4.2.4 Surface Plasmon Enhanced Fluorescence Spectrometry (SPFSm) of Oligonucleotide Array

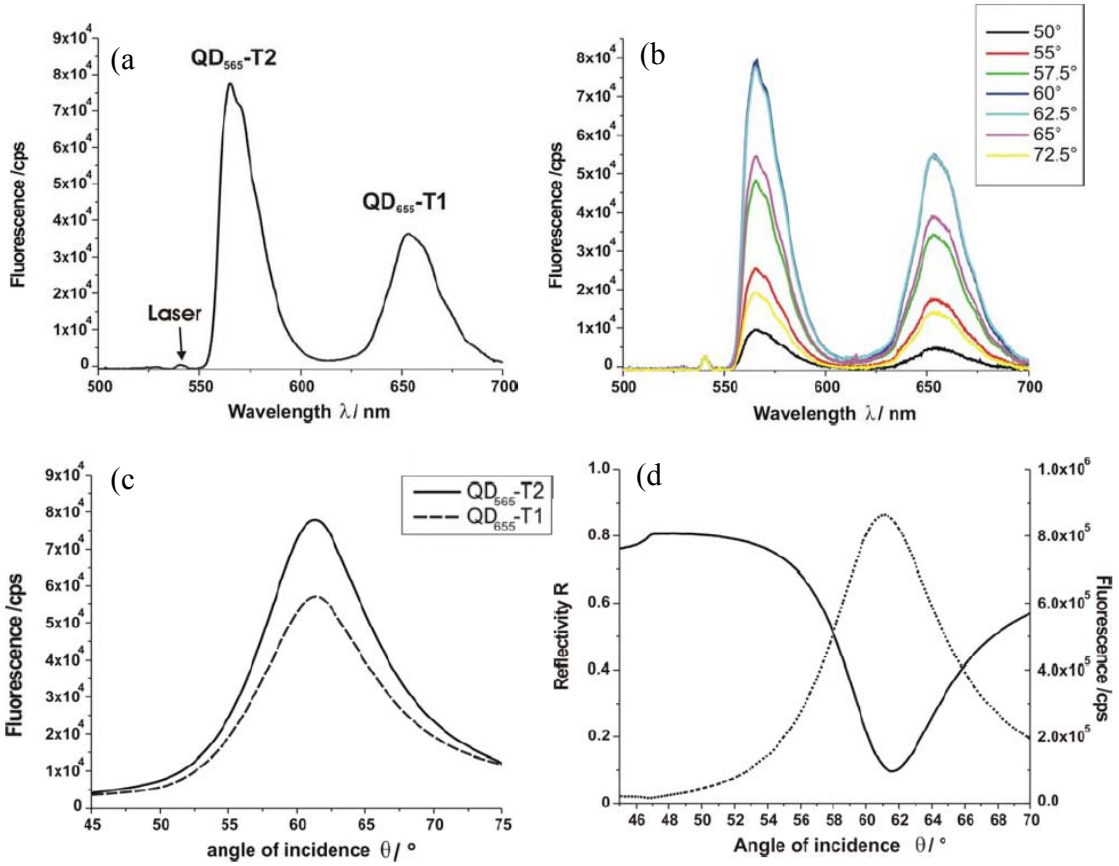

Figure 4.6: (a) Spectral resolution of the fluorescence signal generated by the surface hybridized QD_{565}-T2 / QD_{655}-T1 quantum dot mixture (injection time 10min); (b) Some of the spectrally resolved surface plasmon enhanced fluorescence spectra taken during an angular scan from $\theta = 45°$ to $\theta = 75°$ in $\Delta\theta = 2.5°$; Derived from this data (c) shows two fluorescence intensity angle scans of QD_{565}-T2 and QD_{655}-T1, respectively; In comparison (d) shows the reflectivity (solid line) and fluorescence intensity (dashed line) achieved from a SPFS angle scan of QD_{655}-T1 hybridized to a P1 loaded sensor surface.

In addition to the qualitative SPFM analysis of QD-labeled target DNA sequences, we implemented a more quantitative approach by exchanging the color CCD camera, which serves as an image-generating component in the SPFM setup (Figure 3.4b) with a fiber-optics coupled spectrograph (Figure 3.4c). Using this setup, the excitation of surface-bound fluorescently labeled analytes can be combined with the spectral resolution of the fluorescence signal. Thus, a simultaneous detection of diverse fluorophores with different emission wavelengths, as is the case of using different quantum dots, is possible.

In this case, a fiber-optics coupled spectrograph was used for the simultaneous detection of the QD_{565} and QD_{655} fluorescence on the above-described microarray sensor surface. After setting the angle of incidence for highest fluorescence intensity, a mixture of QD_{565}-T2 and QD_{655}-T1 (20 nM in PBS) was rinsed through the flow cell and, hence, brought in contact with the probe functionalized microarray for 10 min. No further change in the intensity of the fluorescence signal could be observed after this time. The spectrally resolved fluorescence signal is displayed in Figure 4.6a. As can be seen, the fluorescence signal can be split up into two bands with emission wavelengths of 565 nm (QD_{565}-T2) and 655 nm (QD_{655}-T1). The wavelength $\lambda = 543$ nm of the laser source, used for the excitation of the whole SPFS system, contributes only a negligible peak in the detected signal. The difference in the two fluorescence intensities is due to a slightly higher fluorescence quantum yield of the green fluorescent QD_{565} at the excitation wavelength $\lambda = 543$ nm. Next, the fluorescence signal was recorded over a spectral range from 500 nm to 700 nm starting from an angle of incidence of $\theta = 50°$ up to an angle of $\theta = 75°$ in 10 intervals of $\Delta\theta = 2.5°$. Figure 4.6b shows some of the spectra thus obtained. Plotting the highest intensities for both wavelengths, i.e., 565 nm and 655 nm, respectively, against the angle of incidence results in the angular fluorescence intensity scans given in Figure 4.6c. A comparison of these excitation scans with the ones obtained from a SPFS angular scan with a P1/QD_{655}-T1 hybrid (Figure 4.6d) shows the exact conformance of the angle with the highest total fluorescence signal reached at $\theta = 61.55°$.

4.2.5 Conclusion

The presented study is the first demonstration of an analytical combination of surface plasmon enhanced fluorescence spectroscopy with a fluorescent analyte tagged by semiconducting nano- crystals. These quantum dots show several advantages compared to the classic organic dyes, the biggest being their broad spectral absorption range and the well-defined sharp emission wavelength, which makes it possible to excite several quantum dot

populations simultaneously with a single light source and, hence, at a single angle of incidence for resonance surface plasmon excitation.

Our experiments showed clearly that a conjugation system consisting of 5'-biotin-tagged single-stranded DNA sequences attached to streptavidin coupled CdSe/ZnS core-shell quantum dots is suitable for analyte detection by SPR and SPFS. The specific hybridization of QD-conjugated DNA single strands to sensor-attached complementary sequences could be detected by a substantial shift in the angular reflectivity spectrum of the SPR, as well as by a high fluorescence signal, originating from the DNA-bound QDs.

The transfer of the system to the platform of surface plasmon enhanced fluorescence microscopy and the organization of the catcher probe DNA in a microarray format rendered a qualitative analytical approach of measuring the decomposition of QD*x*-DNA*y* mixtures possible. The spectral resolution of the obtained multicolor images with a spectrograph shows the potential of the combination of QD-DNA conjugates with SPFS for future applications in DNA chip analytics.

4.3 *Electrochemically Addressable Functionalization and Parallel Read-Out of a DNA Biosensor Array*

4.3.1. Motivations

Microscopic patterning of self-assembled monolayers (SAMs) on metal surfaces for applications of chemical screening and biological analysis has been in the center of interest for sensor technology for many years. Various patterning methods have been developed and commonly used including microwriting[64], microstamping[65-67], and micromachining[68]. We describe here another strategy based on the *in situ* assembly and electrochemical desorption of thiol SAMs which allows for the fabrication of addressable DNA sensor arrays. Our interests in developing this patterning strategy originates from the need to develop methods amenable to fabricate DNA arrays for parallel analysis in a micro-fluidic platform without experiencing problems associated with multiple mask alignments and/or loss of biological activity encountered with ex-situ techniques.

The electrochemical desorption of thiol monolayers from gold surfaces has been studied [69, 70] and used for the patterning of SAMs via phase-separated binary monolayers[71, 72], by STM tip-induced lithography[73] and in micro-arrays of gold electrodes[74]. The incorporation of a

wide variety of groups both in the alkyl chain and at the chain terminus of the thiol derivatives and their use as building blocks allow for the fabrication of (laterally patterned) supramolecular interfacial architectures. For example, gold electrodes modified by thiolated DNA have proven to be invaluable tools in both the study and the application for DNA mediated charge transport (CT)[75-78] and the electrochemical detection is with high sensitivity and much less expenses[78, 79].

In this work, we fabricate a patterned gold surface, i.e., an array of gold electrode stripes each of which works independently both as an electrode and as a specifically functionalized area. For simplicity, we present here a study of the fabrication and performance characterization of a 4-element addressable sensor system. Thiol terminated methoxy polyethylene glycol thiols (PEG thiols) were first assembled to form a hydrophilic protecting monolayer on all gold stripes. Electrochemical desorption of the PEG thiol from only one of those electrodes results in a bare gold surface on this stripe available for further functionalization. A sequence of thiolated biotin, streptavidin, and biotinylated oligonucleotide strand solutions are applied to this bare gold electrode to eventually functionalize this sensor element with the desired probe sequence. The other electrodes are then subject to the same electrochemical desorption and step-by-step build-up procedures until finally all electrodes are labeled with different probe oligonucleotides except one which works as an inert reference control for the DNA hybridization analysis. The whole preparation was performed in aqueous solution minimizing the risks of losing the molecules' bioactivity.

It should be noted that the total thickness of all these bio-functional building blocks on the gold electrodes adds up to only a few nanometers. However, by employing a surface plasmon microscope (SPM) [43, 44, 49, 80] approach and the related data-analyzing software one can document the interfacial build-up visually in real time and can gain quantitative information about the binding reactions.

Surface plasmon spectroscopy (SPR) and surface plasmon field-enhanced fluorescence spectroscopy (SPFS) were used to sensitively monitor interfacial binding events. Another recently developed, extremely sensitive detection approach, i.e., surface plasmon field-enhanced fluorescence microscopy (SPFM)[2, 3, 25, 81], was then applied to detect in parallel hybridization reactions on a series of individual sensor units simultaneously.

4.3.2. Materials

Thiolated methoxy polyethylene glycol, $CH_3O(CH_2CH_2O)_nCH_2CH_2SH$ ($M_w \approx 5{,}000$), referred to here as "PEG thiol" was purchased from NOF corporation and was used without further purification. The biotinylated thiol, HS-Prop-DADOO-X-Biotin ($M_w = 575.80$) was synthesized and purified in our laboratories at the Max-Plank Institute for Polymer Research (Mainz, Germany). The thiols were dissolved in phosphate-buffered saline solution (PBS buffer, pH7.4) at a concentration of 5×10^{-4} M. Streptavidin (Sigma) was also dissolved in PBS buffer at a concentration of 5×10^{-6} M. All highly purified salt-free oligonucleotides were obtained form Research Biolabs (Singapore) and diluted in PBS to a final concentration of $c_0 = 5\times10^{-7}$ M. The specific probe and target DNA sequences used in this study are given in the corresponding Figures (8, 9, and 11, respectively). All probe oligonucleotides were biotin-tagged at their 5'-end, allowing for the assembly of an oligonucleotide capture probe layer on the bound streptavidin surface layer. All targets were either commercially labeled with the organic chromophores Cy5, or were conjugated in our laboratories [19] with semiconducting quantum dots (Quantum Dot Corp.) emitting at different wavelengths, as indicated. Water used for the solutions was distilled and purified with a Milli-Q system (Millipore Co.).

Thin films of Cr (d = 2 nm) and Au (d = 44 nm) were evaporation-deposited onto a high refractive index glass slide (LaSFN9/Schott) at a pressure of about 5×10^{-5} Pa in a commercial evaporation set-up (Biemtron, Japan) using a mask for the definition of the electrodes on the sensor chip. For simplicity, we prepared only 4 gold stripes each of which acts as a working electrode as well as an addressable detector unit. The size of each electrode was 10 mm in length and 700 μm in width. Neighboring electrodes were separated by a (glass) gap of 200 μm.

Some details of the electrochemical flow cell design are shown in Figure 4.7a. The body of this single-compartment cell is made of Teflon, with a silica glass slide as cover window. The cuvette has two holes for inserting the reference and the counter electrodes, respectively, as well as an inlet and an outlet for liquid sample exchange and rinsing. Electrochemistry was conducted using an AutoLab (Type II μAutolab) potentiostat, with a coiled platinum wire used as counter electrode and an Ag/AgCl electrode as reference.

Figure 4.7b also gives a schematic cross-section of the flow cell attached to the prism coupling unit in the Kretschmann configuration for surface plasmon excitation. The flow cell is sealed by Viton O-rings against the multi-electrode sensor chip, on top of which a prism (LaSFN9, $\varepsilon = 3.4069$ @ $\lambda = 633$ nm) is index matched for surface plasmon resonance

spectroscopy (SPR), surface plasmon microscopy (SPM) and surface plasmon fluorescence microscopy (SPFM) measurements.

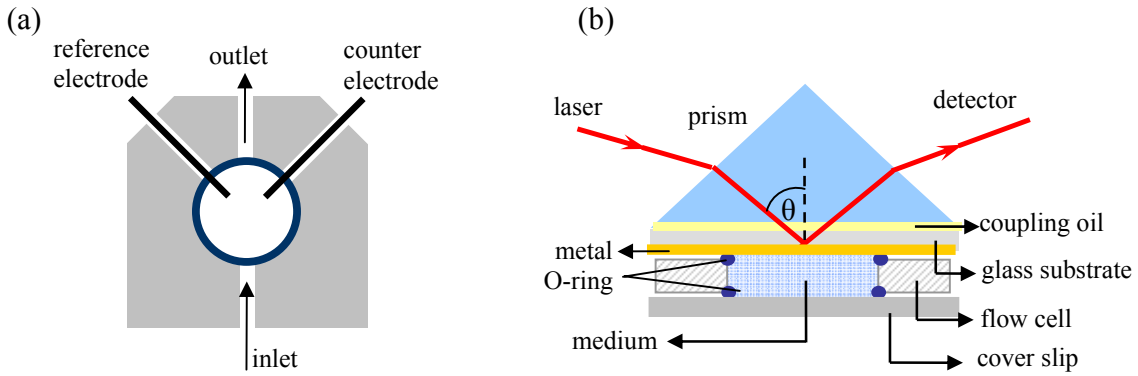

Figure 4.7: (a) Cross-section of the cell body with liquid inlet and outlet for fluid handling and with platinum wire as counter and Ag/AgCl as reference electrode. (b) Schematic of flow cell attached to prism coupling configuration.

As previously shown in Figure 3.3 is a simplified schematic diagram of the combination setup which is based on the Kretschmann configuration and which allows for the recording of both, SPM and SPFM, images. The reflected light is imaged via a biconvex lens onto a CCD camera (Opto). Sample cell and camera are mounted to a two-stage goniometer such that θ-2θ angular scans can be performed in the normal reflection mode of surface plasmon spectroscopy. The video signal of the camera is digitized by a frame grabber unit (Stemmer, ICP-AM-VS) and further analyzed by a PC.

Again, for the purpose of recording oligonucleotide hybridization reactions in the fluorescence microscopic mode, a particularly sensitive color CCD camera (Kappa optoelectronics, Gleichen, Germany) is mounted to that part of the goniometer that rotates the sample cell (θ) thus ensuring that the camera always mounted at a fixed angle normal to the substrate surface. The fluorescence light emitted from surface-bound chromophores is collected and imaged after passing through emission filters in order to discriminate fluorescence against scattered excitation light. The whole setup is controlled by a PC. The software package KAPPA Image Base Control (Kappa optoelectronics) allows for the recording of the fluorescence images. The camera is operated at an internal temperature of T = 25°C and with an integration time of Δt = 20sec.

4.3.3. Selective functionalization of individual electrodes

In a previous study, we described the formation of a self-assembled monolayer on a particular Au electrode of a whole array, while keeping at the same time the other electrodes free from any thiols by applying a potential to these electrodes sufficiently negative to prevent Au-S binding[82]. This strategy, however, can not work for the streptavidin coupling step applied here because this protein would not only bind specifically to the selected electrode via its biotinylated thiol layer, but would also stick non-specifically to all other bare Au electrodes, irrespective of the applied potential. This would lead to a complete loss of control over the addressability for the functionalization of individual sensor stripes. In order to overcome this difficulty, we choose therefore a strategy in which we first assemble a PEG thiol monolayer on all electrodes as a protective coating, followed by selective deprotection (desorption) steps.

For the preparation of the addressable DNA array, the gold coated multi-electrode sensor chip was mounted to the combined SPM and SPFM setup and connected to a potentiostat. The PEG thiol solution in PBS was applied to the sensor chip surface for 20min in order to allow for the formation of a compact, hydrophilic thiol layer on this 4-electrode system, protecting the surface from unwanted adhesion of molecules introduced during the following processing steps. In order to start the thiol desorption, one of the electrodes was connected to the potentiostat as working electrode and a constant potential of E = –1.1V was applied for 8mins followed by a thorough rinse on order to completely remove the PEG thiol producing a fresh, clean gold surface. Biotinylated thiols were then allowed to self-assemble at this bare Au electrode, resulting in a monolayer with a thickness after rinsing of ca. d = 1.5 nm (calculated with n = 1.50). Next, a streptavidin monolayer of ca. d = 4.0 nm in thickness was formed by specific binding from solution to the biotin-sites at the surface. Finally, a layer of biotinylated single-stranded oligonucleotide strands was assembled on the surface by occupying the free binding sites of the streptavidin monolayer. The same preparation cycles were then applied to the other electrodes until a total of three sensor elements were functionalized, each with a different oligonucleotide capture probe, while one electrode remained covered with a PEG thiol monolayer as reference as it is schematically depicted in Figure 4.8. Each interfacial reaction step was characterized by SPR or SPM measurements.

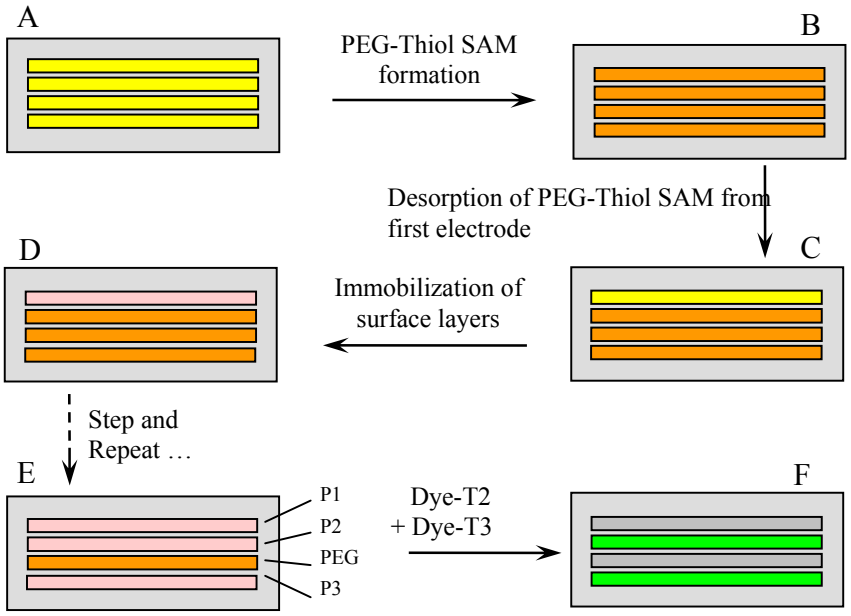

Figure 4.8: Schematic steps used for the fabrication of a series of DNA sensor elements on a patterned Au electrode array. Steps of B, C, D, and E are monitored by SPM; step F is recorded by SPFM. Firstly, PEG thiol solution was incubated on the multi-electrode sensor chip surface to form a compact protecting layer. Then a constant potential of –1.1V was applied on one of the electrodes to completely remove the PEG thiol, recovering a fresh, clean gold surface. Biotinylated thiol, streptavidin, and biotinylated single-stranded oligonucleotide solutions were sequentially applied to finally label this electrode with wanted oligo probe. Same procedures were also applied to the other electrodes, each labeled with a different oligonucleotide probe, while one electrode remained covered with a PEG thiol layer as reference.

4.3.4. Assembly and electrochemical desorption of PEG thiol blocking layers

The experimental results of the various assembly and electrochemically triggered desorption steps are summarized in Figures 4.9 and 4.10, respectively. Firstly, PEG thiol was allowed to assemble at the multi-electrode Au surface (cf. the kinetic mode SPR data in Fig. 4.9a), resulting in a monolayer with a thickness after rinsing of ca. d = 4.2nm (calculated with n = 1.5 from the angular shift of the SPR resonance as given in Fig. 4.9b). Next, the biotinylated thiol mixture and streptavidin were introduced to the system sequentially, causing no change to the interfacial architecture. Correspondingly, the angular scan SPR curves showed no shift in the resonance angle, but are perfectly superimposable as shown in Figure 4B and 4C, respectively. This indicates that PEG thiol is an ideal blocking agent, protecting

the surface from unwanted binding reactions of other building blocks of the interfacial multilayer assembly.

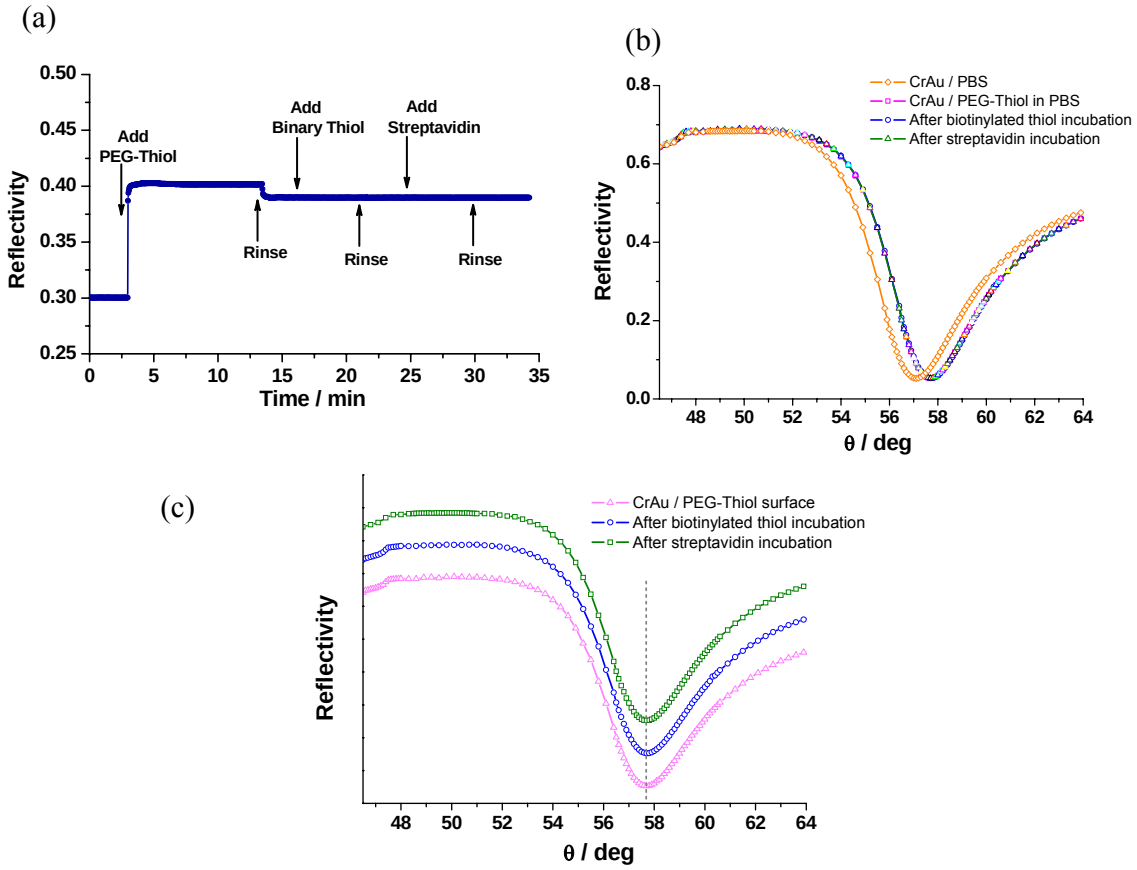

Figure 4.9: (a) Kinetic SPR curve taken at a fixed angle of observation during the formation of the PEG thiol SAM, documenting also its blocking effect against the non-specific adsorption of (incorporation of/ replacement by) biotinylated thiols and streptavidin. (b) Angular scans of the reflected intensity before and after binding of the PEG thiols. The resulting angular resonance shift is clearly visible. Also shown are scans after rinsing biotinylated thiol and streptavidin solutions through the flow cell sequentially and allowing them to interact with the surface. A resonance angle shift can hardly be seen, indicating the excellent blocking properties of the PEG SAM. (c) As B, however, with the individual scans shifted relative to each other for better clarity.

In addition to the adsorption also the irreversible reductive desorption of the (buffer soluble) PEG thiols from the Au substrate was monitored by SPR kinetic measurement (Figure 4.10). Before starting the PEG thiol absorption, the potential applied to the bare gold substrate was held at E = –1.1V in PBS for 4 min and then cycled 3 times between E = 0V and E = –1.1V. The observed rapid decrease in reflectivity upon applying E = –1.1V is attributed to changes in the electron density at the metal/solution interface as well as refractive index changes of the dielectric medium close to the Au substrate caused by the potential-induced ion redistribution [82]. Once the potential was reset to E = 0V, the reflectivity curve returns to the initial value indicating that no major irreversible adsorption to or desorption from the bare gold surface

happened. The slight drift seen in the reflectivity values upon potential cycling is attributed to desorption of some contaminants on the Au electrode surface.

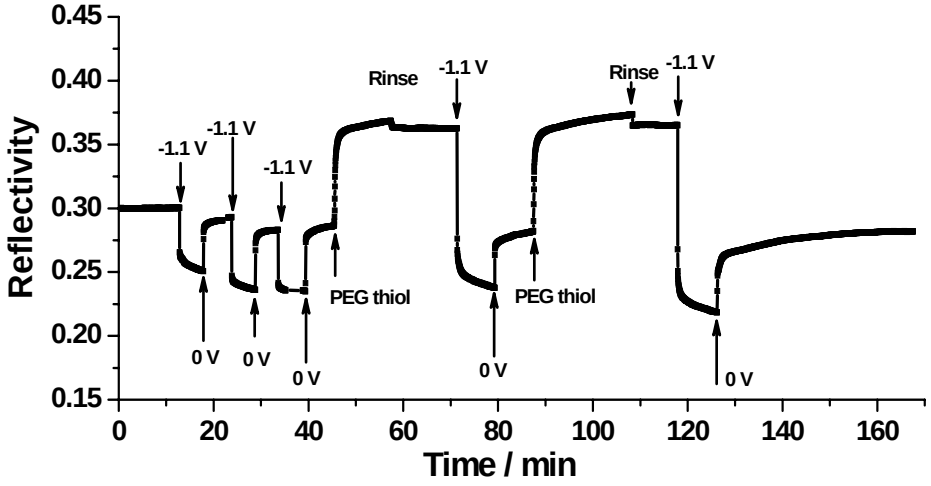

Figure 4.10: Repetitive adsorption and electrochemical desorption processes of PEG thiols on the Au electrode at various applied potentials, as recorded by a SPR kinetic measurement. Firstly, the potential of –1.1V was loaded and released on bare gold substrate for 3 cycles. The reflectivity curve returns to the initial value, indicating that no major adsorption to or desorption from this bare gold surface happened. Next, the introduction of PEG thiol aqueous solution results in a fast self-assembling process to the Au surface followed by quick saturation. The loading of a –1.1V potential causes a great reflectivity decrease so that upon releasing it to 0V, the reflectivity reaches again the value of bare Au, indicating the reductive desorption of the PEG thiol SAM from gold surface. The repeated adsorption/desorption cycle gives the same result.

Next, the aqueous solution of PEG thiol was introduced into the flow cell resulting in a fast self-assembling process to the Au surface followed by quick saturation (cf. Fig. 4.10). After rinsing the system with PBS in order to remove any free or loosely bound PEG thiol molecules from the surface and the cell, a potential of E = –1.1V was applied and held constant for 8mins. The reflectivity decreases rapidly to the value of the bare Au. Upon switching the applied potential to E = 0V, the reflectivity reaches again the value of bare Au indicating the successful reductive desorption of the PEG thiol SAM from that electrode. The identical adsorption/desorption cycle can be performed several times without any indication of a significant degradation of the Au surface or of the PEG thiol SAM (cf. Fig. 4.10).

4.3.5 Monitoring the functionalization of individual electrodes by SPM

Figure 4.11a shows a series of selected SPM images taken at different angles of incidence, θ, with two electrodes being still covered with the PEG thiol SAM (1st and 3rd electrode from top), while the other two electrodes (2nd and 4th from top) were electrochemically cleaned.

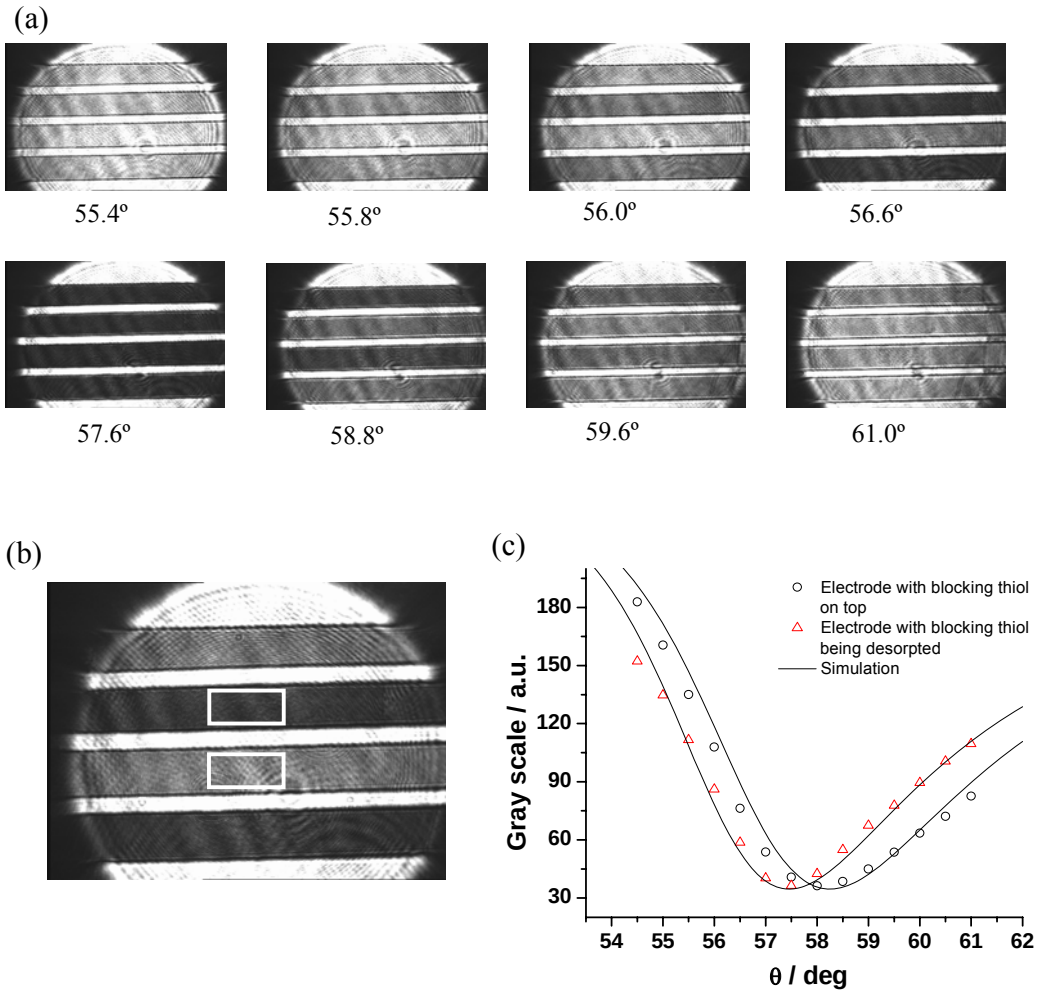

Figure 4.11: (a) A series of selected surface-plasmon optical images taken at different incidence angles. Two electrodes (1st and 3rd from top) were covered with PEG thiol SAM, the other two(2nd and 4th from top) were pure Au (obtained by the electrochemical desorption of the monolayer). (b) Representative image with the definition of a pixel field used then for the evaluation of a gray value histogram. (c) Average gray values of such pixel frames plotted as a function of the angle at which the respective images were taken, for areas with and without a PEG-thiol monolayer

One can see (Fig. 4.11a) that the bare Au electrodes tune into resonance first, i.e., at smaller incident angles, while the Au surfaces still covered with a SAM show the corresponding slight shift of their surface plasmon resonance angle, with the typical contrast inversion[43] seen at $\theta \approx 57.6^{\circ}$. Areas of interests in the images are framed (cf. Fig. 4.11b), and automatically analyzed by calculating simultaneously the pixel gray value histograms of these frames as a function of the incident angle. The obtained average gray values of the two areas of interest, i.e., with and without PEG thiol, were stored and plotted for both area (electrodes) as a function of the incidence angle at which the corresponding image was taken (Fig. 4.11c). The obtained curves agree well with the regular reflectivity curves recorded in the usual

Kretschmann configuration (cf. Fig. 4.9) and can be quantitatively analyzed in the identical way. The fit curves given in Fig. 6C yield a thickness for the PEG thiol layer of d ≈ 4.2nm, in agreement with the values derived from the SPR measurements (Fig. 4.9).

Monitoring the kinetics of these binding reactions on all four electrodes simultaneously in parallel can be achieved by recording SPM images with a frame grabber card as a function of time but at a fixed angle of observation. Following the protocol shown in Figure 4.8, we modified the 3 top electrodes with 3 different oligonucleotide capture probes while taking SPM images. Figure 4.12a gives the overview of the whole process. Two detailed examples of the (many) recorded pictures are given in Figure 4.12b. The left one was taken after the PEG thiol monolayer assembly (passivation) of all Au electrode surfaces but before any reductive desorption from a specific one. The right image shows the change in the pixel gray value of the third electrode from top from which the PEG thiol SAM had been desorbed by applying the required potential of E = –1.1V. The full protocol of the functionalization steps of this electrode is given in Fig. 4.12b, left frame. Plotted are the average reflected intensities of the pixel frames defined in the right image of Fig. 7A as they were calculated from the gray value histograms obtained as a function of time. The desorption of the PEG thiol layer can be clearly seen by the abrupt decrease of the reflected intensity in qualitative (and after the proper calibration also in quantitative) agreement with the reflectivities recorded in the SPR Kretschmann configuration shown in Fig.4.9. Also the short detours to zero applied potentials are reproduced in the SPM images (cf. Figs. 4.12b and 4.9, respectively).

After re-setting the time to zero, the formation of the biotinylated monolayer self-assembled onto the bare Au surface from the binary thiol solution, then the binding of the streptavidin layer, and finally the attachment of the biotinylated oligonucleotide layer can be followed in real time. We should mention that all the processing steps were done in-situ, i.e., all solutions were injected into the flow tubing connecting the bulk reservoirs with the flow cell attached to the SPR spectrometer, with rinsing steps in between solution applications. The whole protocol, hence, is completely compatible with the requirements for the in-situ functionalization of sensor electrodes in micro-fluidic devices.

Simultaneously to the preparation protocol of electrode 3 (from top) we followed the response of the bottom electrode which was not subject to any electrochemical desorption potentials, hence should give only a background signal indicating the successful passivation by the PEG thiol SAM. Indeed, the parallel recording of the response of this inert electrode showed no change of the interfacial architecture (cf. Fig. 4.12b, right plot) despite the fact that

it was also exposed to all the solutions that were injected for the desired functionalization of electrode 3. This confirms again the successful passivation of the Au electrodes by the PEG thiol layer.

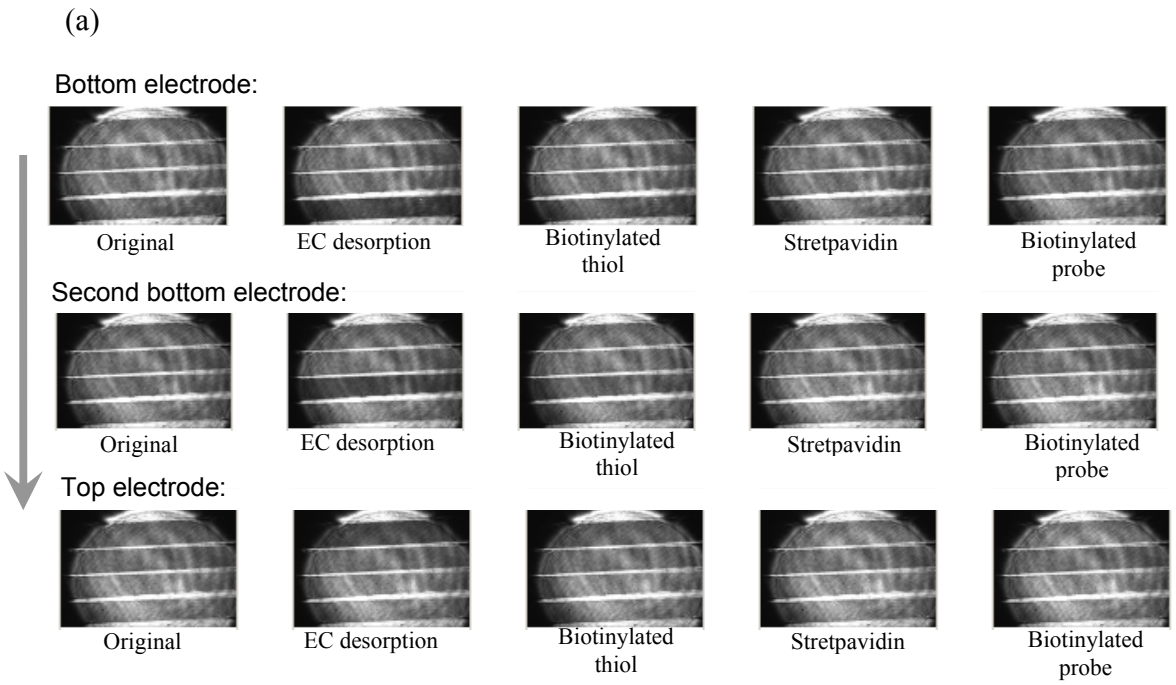

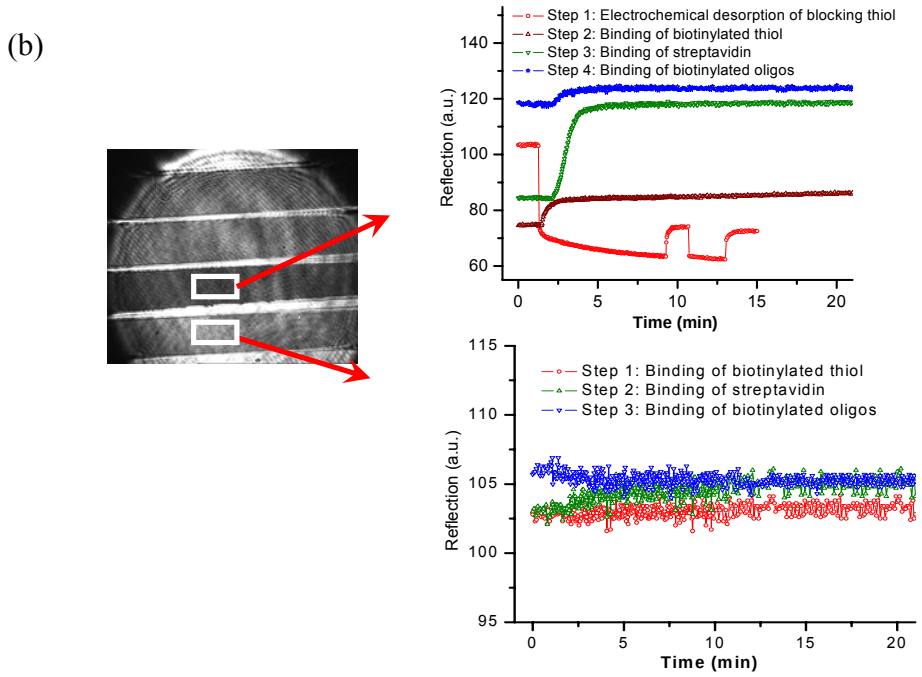

Figure 4.12: (a) A series of selected surface-plasmon optical images taken at fixed angle but different moments during the sensor biofunction process. (b) Quantitative grey-scale *vs* time analysis of areas during the biofunctioning session on the second bottom electrode.

4.3.6 Monitoring parallel DNA hybridization reactions by SPFM

With the sensor array being oriented relative to the exciting laser beam at an angle near the SPR reflectivity minimum corresponding to the incident angle with the highest surface plasmon field enhancement and thus the highest fluorescence intensities the target solutions were injected into the flow cell system. Upon hybridization of the targets to the various oligonucleotide capture probe-functionalized Au electrodes their chromophore tags will be excited by the evanescent tail of the propagating surface plasmon waves. The fluorescence photons emitted from the electrode array will then be imaged by a color CCD camera.

(a)

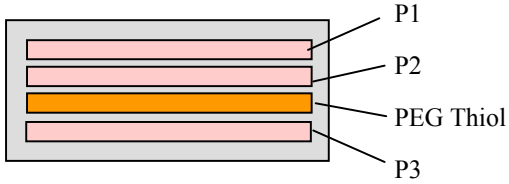

(b)

Name	Nucleotide Sequence
P1	5'-biotin-TTTTTTTTTTTTTTTGCACCTGACTCCTGT-3'
P2	5'-biotin-TTTTTTTTTTTTTTTTGTACATCACAACTA-3'
P3	5'-biotin-TTTTTTTTTTTTTTTTAGAGCTCGACTGAC-3'
T1	3'- CGTGGACTGAGGACA-Cy5 -5'
T2	3'- ACATGTAGTGTTGAT-Cy5 -5'
T3	3'- ATCTCGAGCTGACTG-Cy5 -5'

(c)

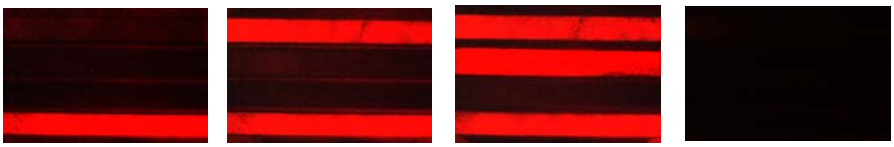

Figure 4.13: (a) Schematics of the arrangement of three different probe oligonucleotides and e PEG thiol SAM as reference on a 4-electrode chip. (b) Nucleotide sequences of the probe and target single stranded oligonucleotides used for the experiments. (c) SPFM images showing the electrode selective hybridization following the sequential introduction of the targets T3, T1, and T2, respectively.

In a first series of experiments, the 4-electrode array was prepared with three different capture sequences, P1, P2, and P3, respectively, (sequences are given in Figure 4.13b) and one PEG thiol SAM as the inert reference electrode, schematically depicted in Figure 8A. The

specific 15mer base recognition sequences were separated from the biotin anchor group by 15 thymine nucleotides acting as spacers. Each of the target strands carries a chromophore, Cy5, that can be excited by the red HeNe laser line @ λ = 632.8nm and emits fluorescence photons with a peak intensity @ λ = 656 nm. Injection of 200nM PBS solutions of each of the three single stranded targets was done sequentially with rinsing steps in between. Figure 4.13c shows the florescence microscopic images recorded during this step-after-step addition experiment. The injection of the target Cy5-T3 resulted in the observation of red fluorescence mostly from stripe P3 according to the high hybridization affinity of this MM0 duplex with all other probes being non-complementary. Hence, the other stripes remained almost dark. Subsequently, upon the application of the target Cy5-T1 the red fluorescent could now be observed only from the electrode functionalized with the probe P1 (Fig. 4.13c, second frame). And finally, the injection of the target Cy5-T2 leads to the decoration of the stripe electrode with the probe P2 (Fig. 4.13c, third frame). During the time of these injections and rinsing steps all hybrids are stable and the targets do not dissociate because the k_{off} rate constants for these MM0 duplexes are sufficiently low. Hence, the fluorescence intensities remain constant. However, the surface could be regenerated by rinsing a 10mM NaOH solution through the flow cell for a few minutes followed by a thorough rinse with pure buffer. This procedure leads to the immediate loss of the fluorescence intensity from the bound targets. By this procedure, the probe array can be regenerated for the next test cycle.

In a second series of experiments, another 4-electrode array was then prepared by the same approach with three different probe sequences P4, P2, and P5, respectively, as shown in Figure 4.14a. The corresponding target strands, T4, T2, and T5, exhibited each a full complementarity to their respective probe strands but were mismatched in 1 or 2 base pairs upon cross-hybridization (cf. Fig. 4.14b). Earlier studies had shown that the nature and the location of the mismatch base pair controls the kinetics of the association and dissociation processes and results in a significantly different stability and, hence, different affinity constant of the hybrid.[25, 60]

Figure 4.15 shows a series of selected SPFM images recorded after hybridization during the dissociation phase, following the sequential application of the targets T2 (Fig. 4.15a), T4 (Fig. 4.15b), and T5 (Fig. 4.15c), respectively, with rinsing and regeneration steps in between. Images were taken with an integration time of 15s over a longer time period, covering roughly 20 min for each dissociation phase. Regeneration was done in each case for a time period of c. 15 min.

(a)

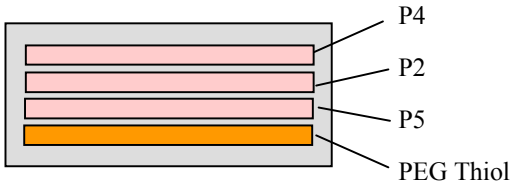

(b)

Name	Nucleotide Sequence
P4:	5'-biotin-TTTTTTTTTTTTTTTTGTACGTCACAACTA-3'
P2:	5'-biotin-TTTTTTTTTTTTTTTTGTACATCACAACTA-3'
P5:	5'-biotin-TTTTTTTTTTTTTTTTGTACGTGACAACTA-3'
T4	3'- ACATGCAGTGTTGAT-Cy5 -5'
T2	3'- ACATGTAGTGTTGAT-Cy5 -5'
T5	3'- ACATGCACTGTTGAT-Cy5 -5'

Figure 4.14: (a) A series of selected surface-plasmon optical images taken at fixed angle but different moments during the sensor biofunction process. (b) Quantitative grey-scale *vs* time analysis of areas during the biofunctioning session on the second bottom electrode.

One can see that following the injection of a 0.5 μM solution of the target Cy5-T2, all of the three electrodes are "decorated" with fluorophores by the hybridizing targets and, hence, emit fluorescence light, with only the PEG thiol SAM coated electrode as the reference remaining totally dark. However, when the flow cell is rinsed with pure buffer, the P5-functionalized electrode, with two mismatches relative to target T2, loses its intensity quickly as a consequence of the rapid dissociation. The color on the P4-functionalized electrode fades away over a relatively long time during the continuous buffer rinse. Only the P2-functionalized electrode keeps its high fluorescence intensity until the 8mM NaOH solution is applied to the cell in order to accelerate the dissociation and, thus, regenerate the whole array.

In the second phase of the experiment, the Cy5-T4 target solution was introduced into the flow cell, (Fig. 4.15b). Again, all 3 oligonucleotide-labeled electrodes are initially "decorated". Rinsing with pure buffer leads to a gradual dissociation from the two MM1 probes (P2 and P5), whereas the MM0 hybrid (P4) again is stable until the NaOH rinse during the regeneration phase.

Finally, applying the Cy5-T5 target solution results in a strong hybrid on the P5-functionalized electrode (MM0), a relatively weaker hybrid on the P4-functionalized electrode (MM1) and very weak hybrid on P2 electrode (MM2). The time needed for the target to dissociate, i.e., the relative duration of the decay of the fluorescence intensity is a qualitative measure of the dissociation rate constant k_{off}, which, of course, could be

quantitatively analyzed by integrating the emitted fluorescence from the various electrodes, again defining appropriate pixel fields on the camera images, cf. Fig. 4.11 and 12, respectively, and plotting the resulting intensities as a function of the (rinsing) time.

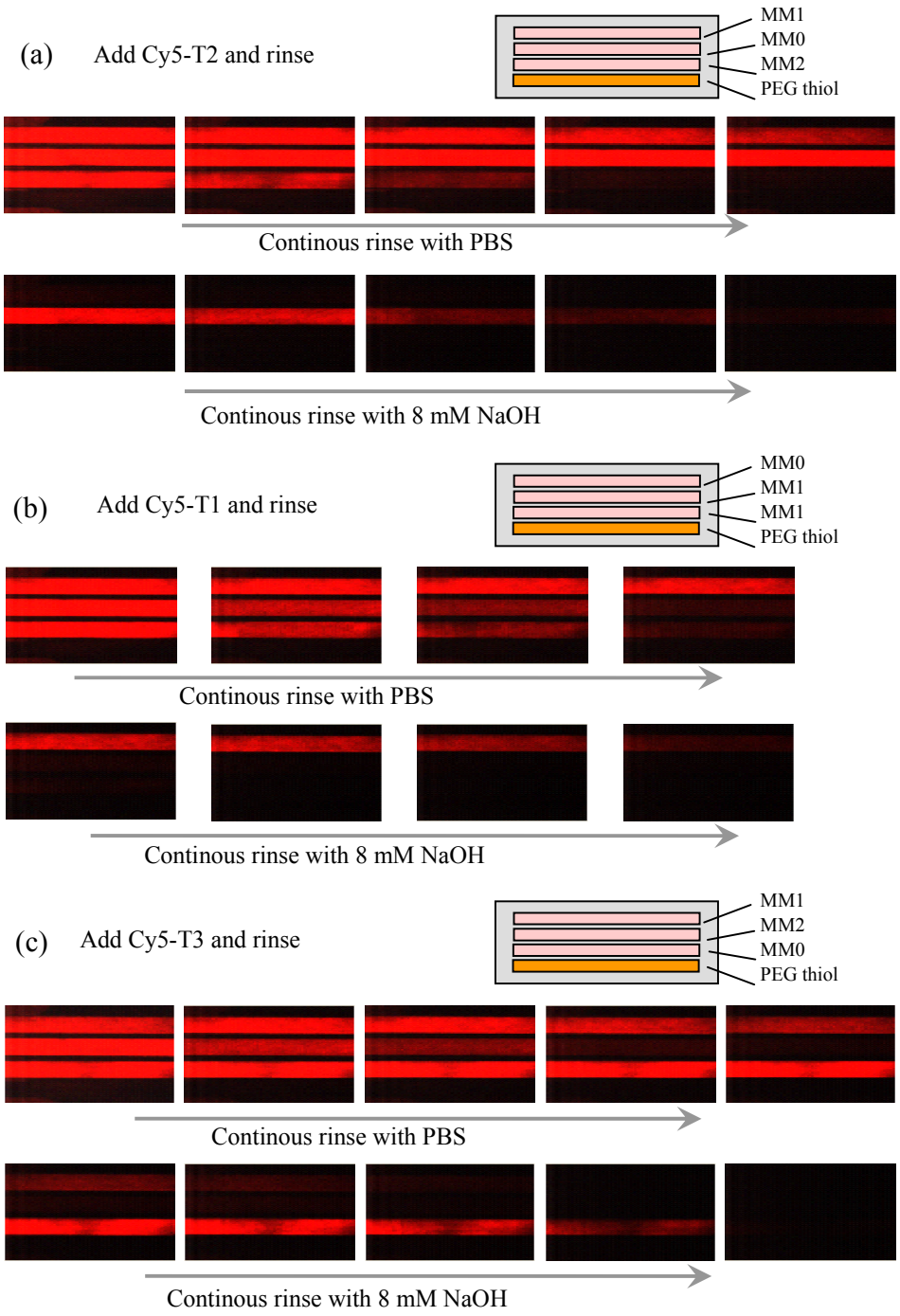

Figure 4.15. Series of time-lapse SPFM images recording the surface DNA hybridization and dissociation of different targets, T1-T3, on their respective electrodes.

In the last example for the use of surface plasmon fluorescence microscopy for hybridization studies we present data obtained from experiments with quantum dots as fluorescent probes.

(a)

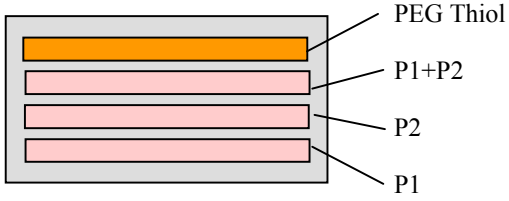

(b)

Name	Nucleotide Sequence
P1:	5'-biotin-TTTTTTTTTTTTTTTTGTACGTCACAACTA-3'
P2:	5'-biotin-TTTTTTTTTTTTTTTTGTACATCACAACTA-3'
T1:	5'-QD655 - TAGTTGTGACGTACA-3'
T2:	5'-QD565 - TAGTTGTGATGTACA-3'

(c)

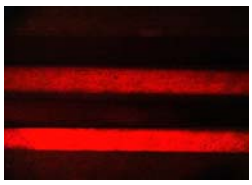

Add T1-QD655
Integration time of 15s

Add T2-QD565
Integration time of 80s

Figure 4.16: (a) Schematic arrangement of the probe oligos on 4-electrode chip for hybridization studies with target oligos being labeled with Quantum Dots. (b) Nucleotide sequences of the probe and target single stranded DNAs. (c) SPFM images showing the sequential hybridizations following the sequential introduction of T1 and T2.

The functionality of the 4 electrodes (Figure 4.16a) was chosen as follows: the top one was covered by the PEG-thiol passivated SAM, working as a negative control. The other three electrodes were, from the bottom, functionalized with P4, P2 and a mixture of P4 and P2, respectively (cf. the sequences given in Fig. 4.16b). The target sequence T4 conjugated with quantum dots emitting at λ = 655nm (T4'-QD_{655} with a red color) and the targets T2, coupled to quantum dots with an emission wavelength of λ=565nm (T2'-QD_{565} emitting in the green) (sequences also given in Fig. 4.16b) could both be excited with a green HeNe laser @ λ = 543nm as the light source, using Cr/Ag/Au (2nm/ 30nm/ 7 nm) as a multi-layer metal film

thermally evaporated via a mask onto the glass slide for the preparation of the 4-electrode array.

The final DNA hybridizing experiment presented here was initiated by injecting firstly a c_0 = 200 nM solution of the red-emitting T4'-QD_{655} target sample in PBS. Figure 11C shows the results: the red fluorescence is seen on the electrodes that are functionalized with probe strand P4, either in a single-component SAM or in a mixture with P2 (cf. Fig. 4.16c, left frame). The other two electrodes covered by a layer of the P2 probe DNA or by the PEG-thiol SAM remained dark at the employed target concentration of c_0 = 200 nM. Subsequently, the T2'-QD_{565} solution was applied to the system and allowed to hybridize to the surface for some time. Now the green fluorescence of the QD_{565} could be observed from the electrode that was exclusively P2-functionalized. The electrode containing a mixture of P4 and P2, however, changed its color from red to yellow due to the RGB color addition of the green fluorescence originating from T2'-QD_{565} with the red fluorescence from the targets T4'-QD_{655} as it has been observed in a similar way for the case of ink-jet prepared sensor spots[19]. Only the electrode protected with the PEG-thiol again doesn't show any fluorescence signal.

4.3.7 CONCLUSION

It has been demonstrated by using an electrochemical method that single Au electrodes in a whole array can be functionalized individually with different single stranded DNA probes without cross-contamination to or from the neighboring electrodes. The documented approach is also compatible with the in-situ functionalization of arrays that are part of an assembled micro-fluidic device, e.g., in a lab-on-chip platform. Surface plasmon microscopy combined with image analysis software can be employed for the on-line recording and quantification of the individual preparation steps of the desired multilayer architecture assembled on the various elements of a 2D matrix array on a sensor chip. Quantitative information of the adsorption or desorption processes on the individual sensor elements can be obtained. Surface plasmon fluorescence microscopy has been shown to be a sensitive method to monitor hybridization reactions to this addressable DNA array platform in a quantitative and parallel way. Association and dissociation rate constants and the corresponding affinities can thus be derived for multiple analyte reactions in-situ and in real time.

5. The construction of tethered bilayer lipid membranes and their optical and electrochemical characterization

5.1 *Introduction*

All living organisms consist of cells as the fundamental building unit. Cells are surrounded and protected by the plasma membrane. The ability provided by the cell membrane to continuously uphold chemical and electrical gradients is a fundamental and necessary capability of life. Furthermore, the membrane acts as a supporting matrix for proteins and other functional components of the cell. Specialized proteins are localized inside the membrane or attached to it, performing a variety of tasks such as energy conversion, storage, communication in and between cells and as a site for molecular recognition and synthesis.[83-86]

The diverse functions of the membrane are primarily due to the associated proteins. Membrane proteins can be divided into two subgroups: transmembrane (spanning the membrane) and membrane bound proteins (bound to or strongly associated with one side of the membrane). A range of models with varying degrees of refinement were proposed for the organization of proteins in the lipid bilayer structure. According to the fluid mosaic model proposed by S.J. Singer and G.L. Nicolson in 1972,[87] there is a continuous bilayer of phospholipid molecules in which proteins are embedded to various degrees.

In addition to the lipids, providing the structure and barrier properties, and the proteins, guaranteeing the selectivity and functionality, there is also carbohydrates (mainly oligosaccharides) attached to proteins and lipids in the membrane.[86] While the carbohydrates attached to proteins seem to play an important role for folding, carbohydrates attached to lipids rather seem to play a decisive role in membrane recognition and adhesion. This part of the membrane is not well investigated, but it is known that this carbohydrate shell is almost exclusively found on the surface membrane of the cell facing outwards. It is the main contributor to the net negative surface charge of most animal cells and plays an important role in determining the response of the immune system to foreign cells. For example the antigens for the different blood groups correlate with differences in the oligosaccharide composition.[86]

Membrane proteins, especially transmembrane proteins are extremely important for key biological processes ranging from photosynthesis, to energy production and to signaling cascades. However there is only limited knowledge about their structure and function, because the functional structure of the proteins is destroyed if they are removed from their native membrane environment. Only a few membrane proteins have been crystallized so far. Another complication seems to be that for a single task in the membrane to be performed often many different kinds of molecules interact. This means that even if a single transmembrane protein is isolated and reconstituted, it may not perform its assumed function without supporting tasks being executed by other membrane proteins and surrounding lipids. Trying to capture the dynamics of membranes and the structure and functionality of its active parts is where biological membrane research struggles today. Even though a huge effort is made to realized this agenda, science still lacks the right tools to accomplish the set goals in a generic way, allowing for example high throughput screening.

Starting from the molecular details, we will move to the exploration of models of the cell membrane in this chapter. These models might not only help us find the fundamental knowledge we are lacking, but also give us a generic platform to realized some of the technological applications in, *e.g.*, sensing surfaces with controlled biological response and drug delivery.

5.2 *Artificial biomembranes*

5.2.1 Lipids

Lipids are amphiphilic molecules. One part of the molecule, the long hydrocarbon tails, finds it energetically unfavorable to be close to water molecules and the other part, the head group, likes water. There is a great diversity of alkyl chains (the hydrophobic part) and the head groups (the hydrophilic part) in naturally occurring lipids. The head groups can have different chemical composition. They can be non-charged, charged or zwitterionic (the charge depends on pH) [84, 88]. Most lipids have two alkyl chains, the length is typically 16, 18 or 20 carbons; with one chain often 2 carbons longer than the other and with one or more unsaturated bonds introducing kinks in the otherwise straight chain. However, the length of the chains and saturation of the bonds might vary substantially.

The most common type of lipid is glycerophospholipids. In this thesis almost all work is done with a glycerophospholipid called phosphatidylcholine. A glycerol moiety is linked to

two alkyl chains and one phosphate group. The phosphate group is linked to a polar head group. The head group of phosphatidylcholines is zwitterionic and it is neutral in the pH range 3-10. The cross sectional area of the phophatidylcholine head group is ~50Å^2. [89, 90]

That one end of the lipids likes water and the other does not, makes lipids want to protect their tails from being exposed to water by forming ordered assemblies. The clustering of hydrophobic molecules in water, which hide the hydrophobic tails behind a screen of hydrophilic head groups, is often referred to as the hydrophobic interaction, although the main driving force behind it is the entropy of the surrounding water molecules. Water molecules form hydrogen bonds with each other, but are able to replace a bond with a new one on a short time-scale, making high entropy (large degree of disorder) possible. If a hydrophobic molecule is introduced among the water molecules, they have to arrange in a cage-like structure around the molecule to maximize the number of hydrogen bonds.[86] The high degree of order forced upon the water molecules by this structure decreases the entropy and increases the total energy. Thus, the more the hydrophobic parts can be hidden from the surrounding water, the lower the energy, and this is the driving force of the self-assembly. The interfacial free energy between hydrocarbon and water is as high as ~50 mJ/m^2. while the end interfacial tension between the polar headgroups and water is as low as ~0.1 mJ/m^2.[91]

Depending on the mixture of lipids they will aggregate to form different structures, where the biologically most important and by far most common is the double-layer, henceforth called bilayer. In a bilayer the hydrophilic head groups are exposed on both sides of the membrane and the hydrophobic tails are hidden within the membrane. These assemblies, although ordered, actually decrease the total energy of the lipids, due to the decreased order of the surrounding water.[84, 92] A bilayer often forms in the shape of a sphere with water on both the inside and the outside. A spherical bilayer is called a liposome or lipid vesicle.

In addition to the hydrophobic interaction bringing the lipids together, there are also interactions between the headgroups, including ionic, dipole-dipole and steric repulsion. Depending on the number, size and saturation of the hydrocarbon tails of the lipids, they might also contribute to a repulsive interaction, but in most cases repulsion is controlled by the properties of the headgroup.

Lipid molecules can be in different phases.[84] The transition temperature from the lamellar gel phase, where lipids are more tightly packed the mobility lower and the alkyl chains are highly ordered (straightened), to the lamellar liquid crystalline phase is called the melting point. The melting point has a well defined transition temperature, T_c, for single-component

bilayers, but is less well characterized for mixtures. The number of unsaturated bonds together with the mixture of lipids and interactions between the head groups decide the melting point of the membrane. The melting point is higher for longer alkyl chains and lower with an increase in the number of double bonds.[93] Other environmental variables than temperature, like pressure, ion composition and concentration also affect the phase transitions.

Lipid bilayers are able to act as a barrier to the diffusion of moleculars and ions. The energy required to move an ion from the aqueous solution to the hydrocarbon interior of the bilayer can to a first approximation be calculated from the Born energy of the image force when the ion approaches the low dielectric interior:[94]

$$W_B = \frac{Z^2 e^2}{8\pi\varepsilon_0 r}\left[\frac{1}{\varepsilon_m} - \frac{1}{\varepsilon_W}\right] \qquad (5.2.1)$$

where r is the radius of the ion, Z is the valency of the ion, $\varepsilon_m \approx 2$ is the dielectric constant of the hydrocarbons and $\varepsilon_W \approx 78$ is the dielectric constant of water. For a K^+ ion W_B is on the order 3eV, which indicates a very low electrical conductance for a bilayer membrane, because of lack of carriers in the membrane.[95]

Actually, when experimentally determined, the permeabilities of virtually all ions and other larger polar species is extremely low, but still much higher than what is expected from the Born energy above. The reason is that in reality pores are formed in the membrane and the permeability of a membrane is in effect that of the pores.[96] Factors determining the permeability in addition to those in Eq. 5.2.1 are hydrophobicity, sign of the charges and counter-ion permeability.[97-100] Hydrophobic molecules may diffuse through the membrane, while small charged molecules and ions are believed to jump between intra-bilayer water cavities to the other side. Large charged transient pore formation must be considered. Thus, it has been shown that the permeability of pure lipid bilayers can be reduced even further by inclusion of cholesterol or other molecules increasing chain ordering, which leads to an increase in cohesiveness and reduction in the number of defects.[101, 102] On the other hand the permeability can be increase through increasing the number of defects by, e.g., phase separation of different lipids in the membrane, by keeping the membrane close to T_c., or the introduction of surfactants that stabilize pores.[103-106]

An ideal bilayer can be modeled as a capacitor, where the two liquid interfaces at the polar headgroups act as the conductor plates and the hydrocarbon chains as the dielectric layer.[107, 108] The capacitance of a parallel-plate capacitor is given by

$$C = \frac{\varepsilon_r \varepsilon_0 A}{d}$$

where ε_r is the relative dielectric constant of the lipid bilayer, ε_0 the permittivity of vacuum, A the area and d the dielectric thickness of the membrane.

Defects and pore formation in the membranes always produce leakage currents and the most common equivalent circuit to interpret the impedance response of bilayers is composed of a resistor R_m and a capacitor C_m in parallel[109, 110], where the membrane resistance, R_m, is very high.

If the applied electric field is high enough it will cause a localized breakdown of the integrity of the membrane and a pore will form. Although the pore is only stable for milliseconds, this procedure has found great use, e.g., to increase the permeability or in micropipette assisted manipulation of vesicles.[111] The mechanism for electroporation is till debated, but its great practical importance has renewed the effort to understand pore formation in lipid bilayers. Pore formation probably also plays an important role in the first stage of membrane rupture and fusion.

5.2.2 Model membranes

Scientific research on detergent and lipid membranes and their use as models for biological membranes date back to the early sixties. Below, the historically most used types of model membranes will be introduced, and their pros and cons in some of experimental situations will be discussed. The last section will focus on the most recent model, tethered bilayer lipid membrane, with which this work is mainly concerned.

5.2.2.1 Multilamellar vesicles

The lipid bilayer structure, historically most commonly used for scientific and industrial purposes, has been the spherical bilayer shell, the vesicle or liposome. Vesicles are classified by their size and the number of bilayers they are composed of. The simplest model membranes to manufacture are so called mutilamellar vesicles (MLVs). They are vesicles with one or more bilayer membranes. The control of vesicle size or number of bilayers per vesicle by this method is very limited, which severely limits its use in scientific studies today. However, MLVs are common in industrial applications like cosmetics and as drug delivery vehicles.[112]

5.2.2.2 Unilamellar vesicles

Unilamellar vesicles are composed of only one bilayer. Usually they are calssified in three different size regimes: giant (GUV, >1μm), large (LUV, 50-1000nm) and small (SUV, 10-50 nm).[112] Unilamellar vesicles can be manufactured in a number ways, including detergent dialysis,[113] dilution from organic solvents,[114] electroformation,[115] thin film hydration,[116] sonication[117] and extrusion[118, 119]. Of these, electroformation, thin film hydration, dilution and detergent dialysis are mostly used to form GUV and large LUV, while extrusion and sonication are predominant for creating vesicles in the 10-400 nm size range.

Making MLVs is the first preparative step to form unilamellar vesicles by both sonication and extrusion. Both protocols are presented in more detail in the experimental section. In this thesis, vesicles with 50nm in diameter are prepared by extrusion because a vesicle this small is in a highly strained configuration. It encapsulates a very small amount of water and approximately two thirds of the lipid molecules are in the outer monolayer. The high curvature gives the vesicle a high elastic energy, which probably facilitates rupture.

The size distribution of a solution of unilamellar vesicles can be determined by light-scattering techniques like dynamic light scattering (DLS), freeze-fracture electron microscopy, ultra-centrifugation, or atomic force microscoy (AFM). The lipid concentration of the vesicle solution can be determined by measuring the phosphate content spectroscopically after converting it to inorganic phosphate.[88]

5.2.2.3 Black lipid membranes (BLM)

When using membranes in research, or for many applications, access to the volumes on both sides of the membrane is often crucial.[91] For example, investigation of all charge transfer processes, which are the most commonly investigated type of process, requires an electrode on each side. To make this possible with vesicles, the interior has to be accessed through a micropipette, which requires the vesicle to be microns large and excludes the use of surface sensitive probes. An important step in membrane research was the creation of planar membranes separating two large volumes. These membranes are formed as free-hanging bilayers over micrometer sized apertures in thin hydrophobic substrates with buffer on each side, and are called Black Lipid Membranes (BLMs).[120-122] They are generally created by continuous thinning from an *n*-alkane solvent of a multilamellar membrane deposited by painting with a thin brush across the aperture, originated by Mueller *et al*.[123, 124] Other methods of preparation are spreading lipids on top of the buffer surface, by lowering the buffer level and rising again bilayer is thus formed.[125]

Black lipid membranes are very suitable for electro-chemical measurements, since there is easy access to both sides of the membrane. In addition, there is no perturbing surface, and both the membrane and incorporated functionalities are likely to be close to their native state.

The major drawbacks of BLMs are the difficult preparation and the lack of stability. It takes time to create a free-hanging bilayer because of the slow thinning and once created it is unstable in the presence of little amount of contaminants and generally has a life span of less then a few hours before it ruptured.[84] The thinning from solvent also leaves a residue of alkenes inside the bilayer, which is in equilibrium with the bulk concentration. The residual solvent has been shown to quite strongly affect the material properties of the bilayer like thickness, elasticity and electrical properties. It is also impossible to prepare large area BLMs. Their typical size is only ~0.002cm^2.[126] Furthermore, BLMs are not as compatible with most surface sensitive probes as supported bilayers.

5.2.2.4 Supported bilayer lipid membranes (sBLM)

It is desirable to form lipid bilayers on a solid support.[40] The most common ways to assemble supported bilayers are self-assembly from vesicles in solution (vesicle fusion),[127, 128] Langmuir-Blodgett deposition (LB),[39, 42] self-assembly from lipid dispersion directly on electrodes (*e.g.* solvent exchange)[129-131] and detergent dialysis[132-134].

Among these, self-assembling by spontaneous rupture of vesicles upon interaction with a surface has gained most interest during the last couple of years because of simplicity, the high surface coverage and reproducibility and the low number of defects. In addition, this method is attractive for easy integration of functional components, *e.g.*, membrane proteins. Proteins can be reconstituted into vesicles with a high degree of orientation using detergent dilution protocols, and these proteoliposomes can then be fused to form protein integrated solid supported membranes.

The major advantage of a supported membrane is its attachment to a solid support, resulting in a high mechanical stability. This kind of membrane formation can also be accessed by variety of sensitive surface analysis techniques such as surface plasmon resonance spectroscopy, quartz crystal microbalance, scanning probe microscopy, as well as electrochemical measurements, which makes supported bilayers easily integrated into sensing platforms. This concept, however, suffers from a number of intrinsic difficulties: the mere physical coupling of the lipid bilayer to the solid support eventually may lead to a detachment or replacement by other surface-active components, thus rendering the membrane's lifetime

too short for practical purposes. The lipid/substrate interactions and their specific separation distance dependence results in the rather low equilibrium thickness of the intermediate water layer (d~1-2 nm) thus, generating a steric problem for integral proteins. Some of the proteins envisaged from basic biophysical studies or for sensor applications are known to protrude much further out from the bilayer surface into the adjacent water phase. The lack of a well-defined ionic reservoir on the substrate side of the bilayer leads to a situation where parts of these functional units would interact strongly with the substrate leading to a partial loss of functionality or even to a complete denaturation.

5.2.2.5 Tethered bilayer lipid membranes (tBLM)

The concepts that have been developed to overcome limitations of sBLMs involve an additional structural element, a tethering layer, which has a twofold purpose.[135] On the one hand, it links the membrane to the substrate in a mechanically and chemically stable way establishing covalent bonds between the lipid molecules in the proximal monolayer of the membrane and the tethering units and, in a similar way, to specific reactive groups on the modified substrate surface.[136, 137] A chemical stabilization of the whole complex architecture is expected to result in the desired long-term stability. On the other hand, this tethering system leads to the required spatial and functional decoupling of membrane and substrate. As a result, a sufficient separation can be built into the multilayer architecture allowing for the unperturbed incorporation of even bulky proteins.

Vogel *et al.* firstly reported tBLM architecture using so-called thiolipids with linked hydrophilic ethoxy spacer group in 1994. [138] Cornell and coworkers[41] were the first using half-membrane spanning tether lipids with benzyl disulphide (DPL) and synthetic archaea analogue full membrane spanning lipids with phytanol chains to stabilize the structure and polyethyleneglycol units as a hydrophilic spacer. Knoll and co-workers[139-141] were the first to introduce to use oligopeptide sequences as hydrophilic spacers attached to the head group of lipid, resulting in the formation of peptide-tethered bilayers.

For the preparation of tBLMs, the substrate is first modified by a linker layer, in many cases a self-assembling bi-functional system that has one chain end with a reactive endgroup that can specifically bind to the particular substrate surface. Typical examples are thiols, sulfides or disulfides for the modification of noble metal surfaces like Ag or Au, or silane groups (trichloro- or trimethoxy- silanes) for coupling reactions to SiO_2 or TiO_2 surfaces. A stable, partially covalently bound tethered monolayer is obtained.

The outer leaflet can be deposited by Langmuir-Blodgett transfer, vesicle fusion, or solvent exchange, with the polar headgroups remaining permanently in contact with the aqueous phase. The vesicle fusion process is particularly attractive because it allows one to integrate functional proteins into the tethered membrane matrix simultaneous with the bilayer formation by fusing vesicles that contain the reconstituted protein of interest. Thus, one builds on the rich experience of protein reconstitution, which was for many years an active research topic in the model membrane community.

The tBLMs mostly reported are supplemented with polar peptide,[142] oligomer,[138] or polymer[143-145] spacers. Poly- or oligomeric tether molecules based on poly- or oligo(ethylene glycol) modified with dialkyl lipids tails have been employed in many cases. However, the capacitance and impedance of these tBLMs were found in the ranges 0.5-0.8 μFcm^{-2} and 0.01-0.1 $M\Omega cm^2$, respectively, insufficient to match the electrical properties of biological membranes. The model system that best reflects the electrical properties of the biomembrane is the bilayer lipid membrane (BLM), which shows capacitance values of around 0.5 μFcm^{-2} and impedance values of >10 $M\Omega cm^2$.[135, 146] tBLMs with good electrical insulation properties were presented by Cornell *et al.*,[147] who used a multicomponent system consisting of a monophytanoyl spacer lipid together with a transmembrane lipid.

5.3 *Materials and experiments*

5.3.1 Lipids and thiolipids

The tBLMs presented in this thesis are based on self-assembled monolayers of thiolipid molecules named DPTL (2,3-di-O-phytanyl-sn-glycerol-1-tetraethylen glycol-DL-α-lipoic acid ester) synthesized by Petia Atanasova from MPIP, Mainz. The synthesis and purification were described earlier.[148, 149] Phytanyl chains were chosen as hydrophobic tails instead of alkyl chains because of their low phase transition temperature and their influence on the density and stability of biological membranes.[150] The phase-transition temperature of 2,3-di-O-phytanyl- sn-glycerol-1-tetraethylene glycol was determined to be < -80 ℃ by differential scanning calorimetry (DSC). In contrast to the system of Cornell *et al.*[147] which bears one phytanyl chain, our system has two phytanyl chains bound to the spacer through a chiral glycerol unit since it is known that a single hydrophobic chain does not guarantee a stable insertion of molecules into a lipid membrane.[151] Furthermore, the 2,3-di-O-phytanyl-sn-

glycerol unit contains only ether linkages to prevent hydrolytic cleaving. This moiety is known to form stable biomembranes under the extreme living conditions (*e.g.* high temperatures) of extremophiles or archaea.[152] The importance of the ether linkage and the absence of esters and polar phosphatidyl groups to form highly impermeable membranes was experimentally demonstrated by Mathai et al.[153]

(a)

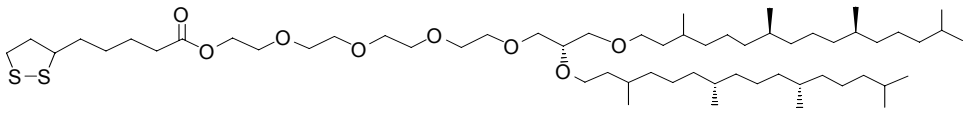

2,3-di-O-phytanyl-sn-glycerol-1-tetraethylen glycol-DL-α-lipoic acid ester (DPTL), tethered molecule, thiolipid

(b)

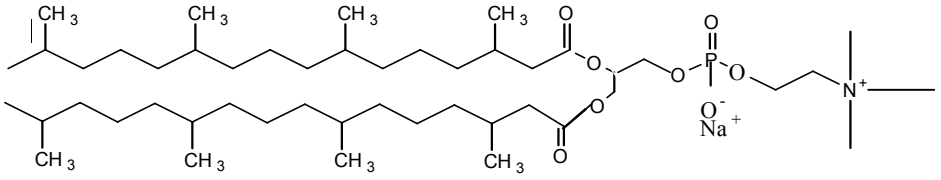

1,2-diphytanoyl-*sn*-Glycero-3-Phosphocholine (DPhyPC)

(c)

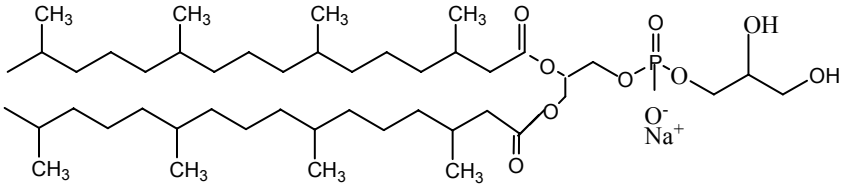

1,2-diphytanoyl-sn-glycero-3-phosphate (DPhyPG)

Figure 5.1: Chemical structure of (a) DPTL; (b) DPhyPC; (c) DPhyPG

The ethyleneoxy spacer unit separates the lipid layer from the gold surface, serving as a reservoir underneath the membrane to prevent the impairment of embedded proteins. Surface-immobilisation is achieved by sulphur anchor group, which forms a covalent bond with Au coated substrate surface.

In addition, the lipid composition of vesicle also shows an influence on the fusion process. Composition and molecular shape of the lipids determine the physical properties of the lipid membrane (e.g., membrane fluidity, bilayer thickness, surface charge distribution, and lateral pressure). Consequently, these properties may affect the structure and function of the incorporated ion channels. In this work, diphytanoylphosphatidyl choline (DPhyPC), and 1,2-Diphytanoyl-*sn*-Glycero-3-[Phospho-*rac*-(1-glycerol)] (DPhyPG) have been chosen to

prepare pure and mixed liposomes. All the compounds are shown in Figure 5.1. Furthermore, by using liposomes prepared in pure water, additional osmotic shock was utilized to promote the fusion process since a relatively high ionic strength electrolyte was used for the bathing solution.

5.3.2 Preparation of template stripped gold

Since the dimensions of the tBLMs are in the nm range, having a very smooth substrate is crucial for the tethered membrane to achieve good electric sealing property. For this purpose, template stripped gold (TSG) was used.[154, 155]

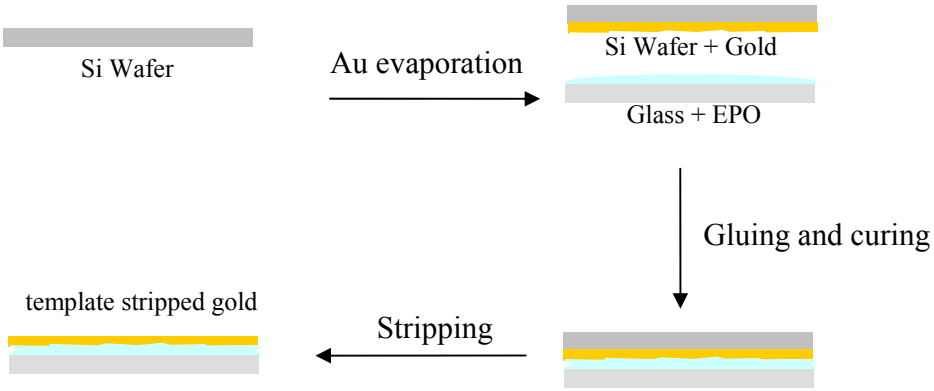

Figure 5.2: Schematic illustration of template stripped gold fabrication

A scheme of the preparation is shown in Figure 5.2. Silicon wafers were carefully cleaned with $NH_3 : H_2O_2 : H_2O$ (1:1:5) at 75°C for 15 min, then extensively rinsing with Mill-Q water. On the cleaned silicon wafers 50nm thick gold films were deposited by electrothermal evaporation (rate 0.01 nm/sec -0.05 nm/sec, 2×10^{-6} mbar) under vacuum in a commercial instrument (Edwards). Gold films on silicon wafers were then glued with EPO-TEK 353ND-4, (n = 1.5922 at 633 nm) to glass slides and cured for 60 min at 150°C. The silicon wafers were detached from the gold film immediately before use. Stripped gold on the glass slide, templated by silicon wafer, shows a roughness of <0.3 nm as determined by AFM.

5.3.3 Construction of tBLMs

DPTL was dissolved in ethanol at a concentration of 0.2 mg/ml. Template stripped gold (TSG) slides were then placed in the solution at room temperature for 24 hours to assemble

the monolayer. The samples were then rinsed in ethanol and dried in a stream of nitrogen. The slide was immediately mounted to an electrochemical cell for use.

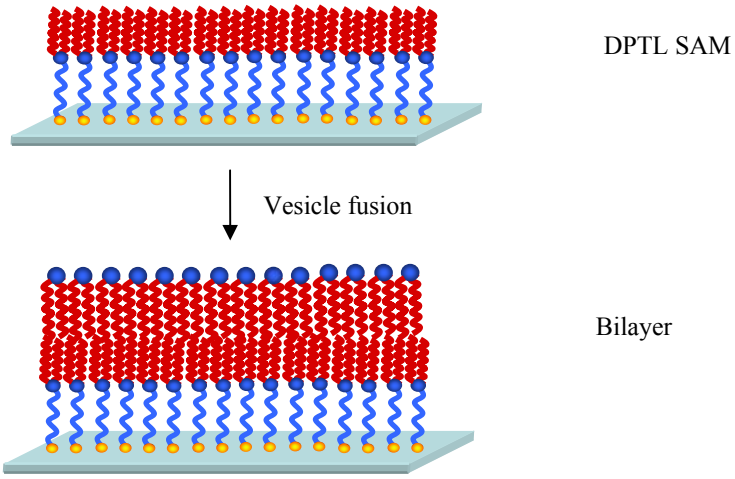

Figure 5.3: Schematic illustration of the formation of a tethered lipid bilayer membrane.

The mobile lipid outer leaflet was then formed by fusion of a liposome mixture. In this work, the assay depends on a source of unilamellar vesicles prepared under standard conditions to ensure maximum reproducibility. A phospholipid composed of either diphytanoylphosphatidyl choline (DPhyPC), or 1,2-Diphytanoyl-*sn*-Glycero-3-[Phospho-*rac*-(1-glycerol)] (DPhyPG), or the mixture of both at certain ratios were used. The lipid mixture was dissolved in chloroform and stored in a refrigerator as a stock solution. The solvent was lyophilized and the dried lipids were dissolved in MilliQ water at a concentration of 2 mg/ml and the hydration was conducted at 70°C for 2 hours, followed by 4 cycles of freeze-thawing. Thereafter liposomes were prepared by extrusion up to 21 times through a 50 nm polycarbonate membrane to obtain a clear solution of vesicles. The vesicle solution was always used freshly, as the small-size vesicles tend to fuse, aggregate and adsorb on the vial surfaces. The solution was then diluted with Milli-Q water to a final working concentration of 0.05 mg/ml. Vesicle fusion on DPTL monolayer was left for 4-10 hours to obtain the equilibrium of increase in resistance and decrease in capacitance.

5.3.4 Optical and electrochemical characterization of vesicle fusion

Starting with the DPTL SAMs, the fusion process was then followed by prism coupled SPS. Spectra were recorded before and after vesicle fusion when the DPTL SAMs were exposed to

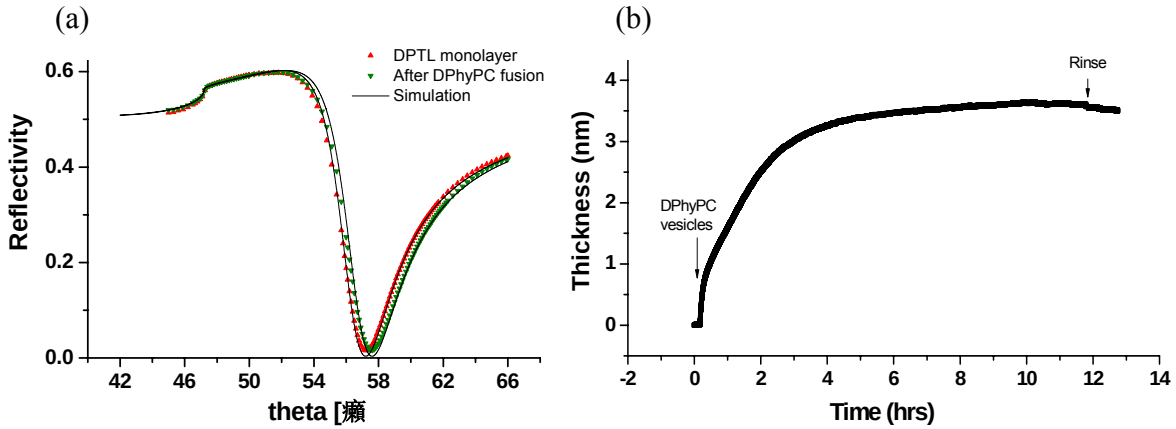

Figure 5.4: The formation of lipid bilayer as monitored by surface plasmon resonance spectroscopy (SPS): (a) angular SPR scans of mono- and bilayer and the corresponding theoretical fits; (b) kinetic trace shows the fusion process of vesicles.chematic illustration of template stripped gold fabrication

the suspension of liposomes. They were analyzed according to the Fresnel equations as shown by the simulated curves. The layer thickness was calculated using a two layer model comprising the tethered thiolipid and free lipid layer with refractive indices of n = 1.41 and n = 1.5, respectively. If measurements were carried out at a constant angle of incidence, reflectivity shifts were directly transformed into the layer thickness, which was monitored as a function of time. For example in figure 5.4 showing the increase in the layer thickness at the angle of 56.2°, when a monolayer was brought in contact with a suspension of liposomes, the fusion process was monitored as a function of time.

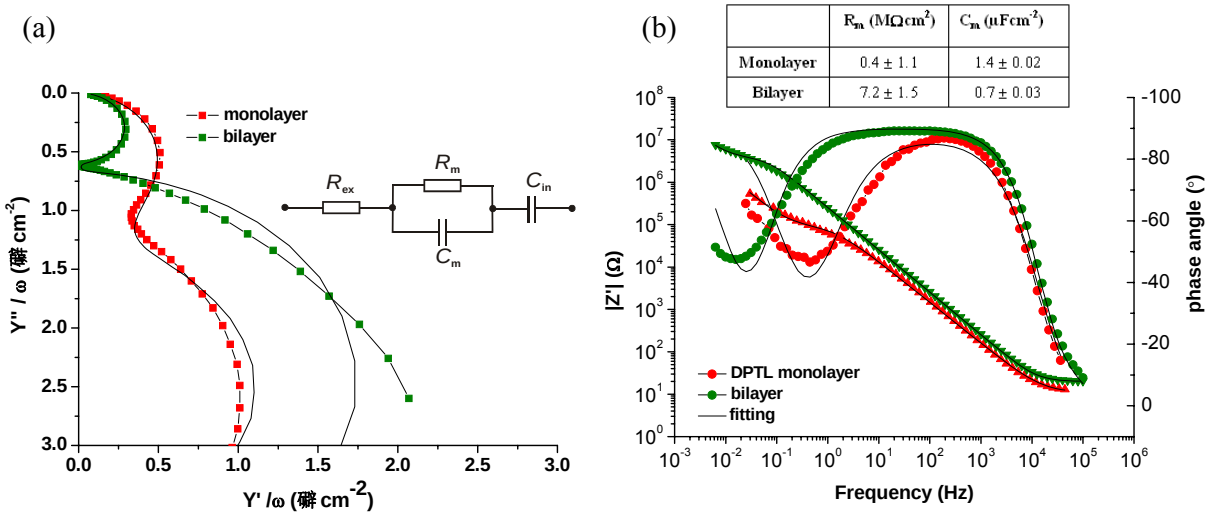

Figure 5.5: EIS spectra of DPTL SAM before and after vesicle fusion. The Nyquist plot (a) and Bode plot (b). Inset is the equivalent circuit used to fit the experimental curves.

Vesicle fusion can also be monitored electrically as a drop in the membrane capacitance and a steady increase in resistance. Selected Bode plots of impedance spectra after vesicle addition are shown in Figure 5.5 (a). The values for the resistances and capacitances calculated from fits to the equivalent circuit are summarized in the plot in Figure 5.5 (b).

A fast increase in resistance can be observed at the first stage, followed by a relatively slow change for a long period. This implies that the change in impedance is a process of rearrangement of the lipids to reach the lowest energy state by forming a tighter membrane.

5.4 *Ion carrier valinomycin in tBLM*

For the study of ion transport processes due to protein activity, a high background resistance of the membrane is essential. After ascertaining the formation of a lipid bilayer, it is important to verify whether this platform is able to host membrane proteins in a functionally active manner. Key features are the high electrical sealing properties of the bilayer, to allow for ion transport due only to protein action, and an ion reservoir between bilayer and substrate. The ion carrier valinomycin was used for this test.

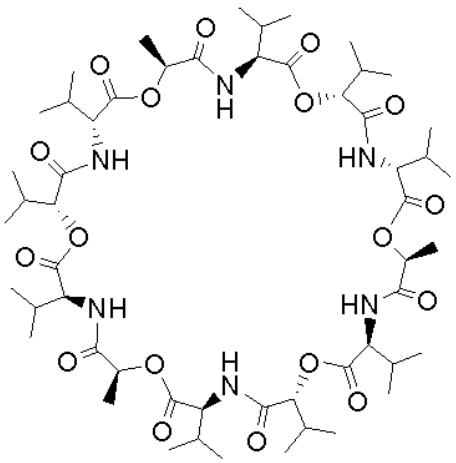

Figure 5.6: Structure of valinomycin.

Valinomycin is a dodecadepsipeptide obtained from the cells of several Streptomyces strains.[156] It is made of twelve alternating amino acids and esters, 3 repeats of the sequence shown in Figure 5.6, to form a macrocyclic molecule, hydrophilic in the inside, and hydrophobic outside. Puckering of the ring, stabilized by H-bonds, allows valinomycin to closely surround a single unhydrated K^+ ion, with six oxygen atoms of the ionophore interacting with the bound K^+, replacing oxygen atoms of waters of hydration.[157] The 9 isopropyl groups and 3 methyl groups contribute to a low solubility in water but relatively

(a)

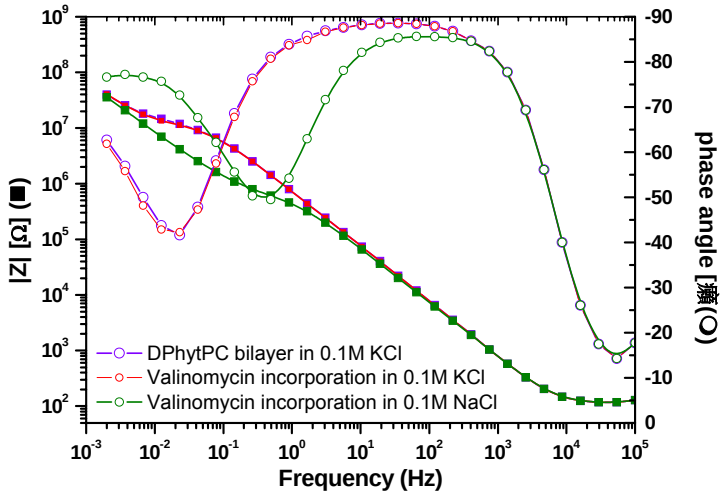

(b)

	R [MΩcm^2]	C [μFcm^{-2}]
Bilayer in 0.1M KCl	4.88	0.71
Valinomycin/Bilayer in 0.1M KCl	0.37	0.71
Valinomycin/Bilayer in 0.1M NaCl	4.92	0.71

Figure 5.7: (a) EIS spectra of valinomycin incorporated tBLM by changing buffer solution; (b) Resistance increase and capacitance fitted from equivalent circuit.

high solubility in lipids. The high affinity for potassium gives this compound utility as an antibiotic, an insecticide, a nematodicide, and an ionophore in K^+ specific electrode.

Valinomycin is a dodecadepsipeptide obtained from the cells of several Streptomyces strains.[156] It is made of twelve alternating amino acids and esters, 3 repeats of the sequence shown in Figure 5.6, to form a macrocyclic molecule, hydrophilic in the inside, and hydrophobic outside. Puckering of the ring, stabilized by H-bonds, allows valinomycin to closely surround a single unhydrated K^+ ion, with six oxygen atoms of the ionophore interacting with the bound K^+, replacing oxygen atoms of waters of hydration.[157] The 9 isopropyl groups and 3 methyl groups contribute to a low solubility in water but relatively high solubility in lipids. The high affinity for potassium gives this compound utility as an antibiotic, an insecticide, a nematodicide, and an ionophore in K^+ specific electrode.

As a potassium selective ionophore, valinomycin is commonly used as a tool in biochemical studies. It can bind or release K^+ when it encounters the membrane surface. The direction of net flux depends on the electrochemical K^+ gradient.

In practice, a tethered DPhyPC lipid bilayer based on a DPTL monolayer was established in 0.1M NaCl (refer to 5.3.3). Valinomycin spontaneously partitions into the bilayer if an

aliquot (10 µl, 9 µM) of an ethanolic stock solution (c = 2 mg/ml) is added to the measurement cell. As a potassium carrier, its conductivity of K^+ over Na^+ is 10^3 higher in BLMs.[158]

Figure 5.7 shows a series of EIS spectra of valinomycin containing tBLM at different electrolyte buffer solution. The experiment was initially conducted in 0.1M KCl. As can be seen from the graph, the resistance decreased 10 fold if a small amount of valinomycin was incorporated into the membrane. However, after changing the buffer solution thoroughly with 0.1M NaCl, the membrane resistance increased back to the level before valinomycin incorporation. If the buffer solution was again replaced with 0.1M KCl, the membrane again showed much lower resistance compared with the value in NaCl, which clearly displays the selectivity for potassium ions of this ion carrier. In all cases, the capacitance stays constant, which illustrates the integrity of the membrane. Therefore no loss of the sealing properties of the membrane could be observed.

If the ionic strength was kept constant, while the buffer was exchanged stepwise with higher concentration of potassium ions, one can see valinomycin's function as a potassium-specific transporter more clearly as shown in Figure 5.8. A decrease of the resistance can be observed upon increasing potassium concentration, while the other components of the equivalent circuit remain rather constant.

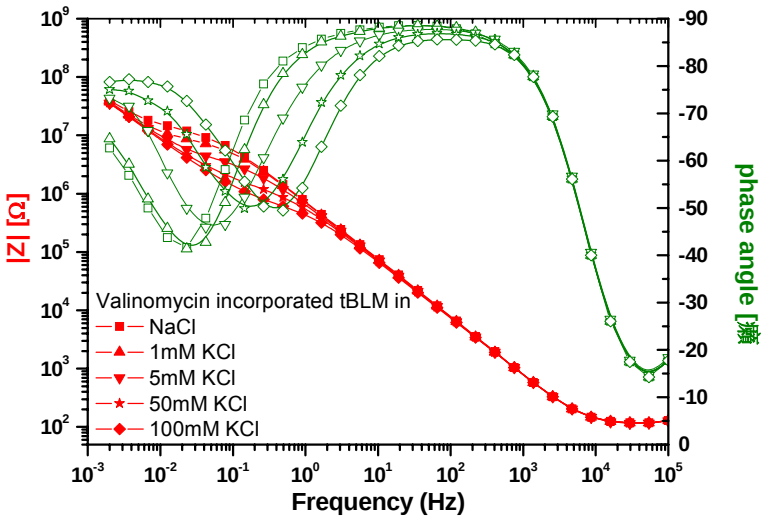

Figure 5.8: (a) EIS spectra of valinomycin incorporated tBLM at different potassium concentrations.

6. INCORPORATION OF THE CHANNEL FORMING PEPTIDE ALAMETHICIN IN tBLMS

6.1 *Introduction*

Transmembrane pores formed by integral membrane proteins selectively enable ions to move across lipid bilayers at high rate (~10^7 ions s^{-1} $channel^{-1}$). They are important in numerous cellular processes, including electrical signaling, fusion events, maintenance of osmotic balance, and drug and antibody delivery into cells.

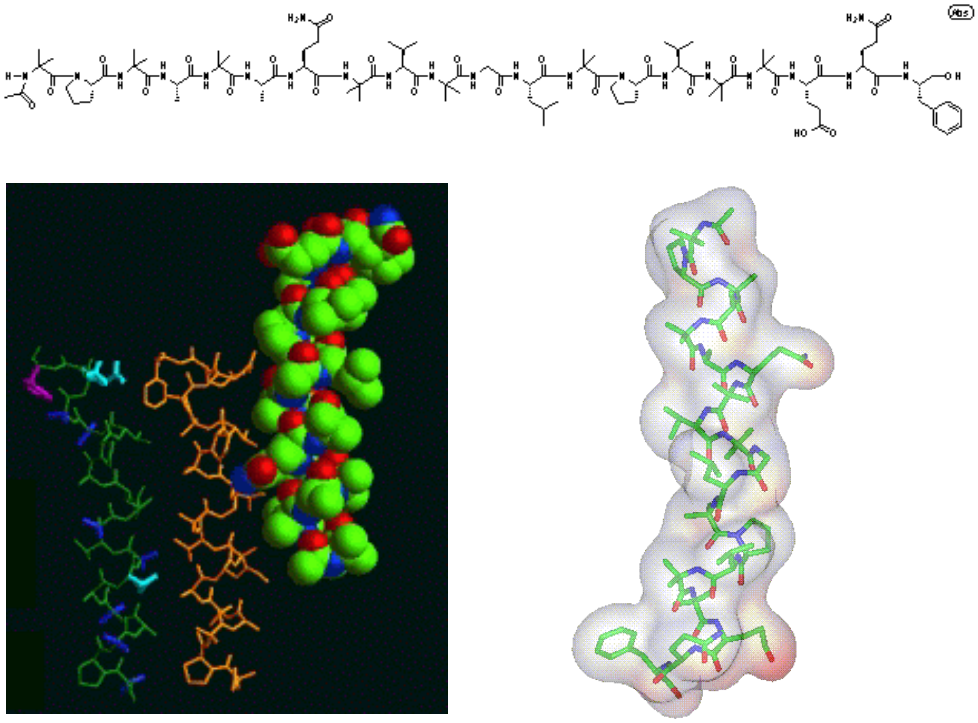

Figure 6.1: Structure of alamethicin.[159, 160]

Alamethicin (Alm) is a simple linear ion channel forming peptide isolated from the fungus *Trichoderma viride*. It consists of 20 residues, with the C-terminal being Phe, and the N-terminus being acetylated.[159, 160] The structure of Alm has been studied intensively.[161-164] Alm serves as a complex and interesting model for channel activity. The sequence of Alm is Ac-AibPro-Aib-Ala-Aib-Ala-Gln[7]-Aib-Val-Aib-Gly-Leu-Aib-Pro[14]Val-Aib-Aib-Glu[18]-Gln-Phe. Aib residues generally restrict the possible orientation of peptides so that the Alm

molecule adopts a predominantly α-helical conformation, in the crystal, in nonaqueous solvents, and in the presence of lipid bilayers.

Alm can either bind to the lipid bilayer surface or insert into the membranes, which depends on several factors such as peptide concentration, peptide/lipid (P/L) molar ratio, type of lipid bilayer regarding elasticity and structure, and hydration level of the membrane. After insertion, Alm monomers can multimerize to form channels characterized by multiple conductance states in a variety of artificial lipid bilayers and natural cell membranes.[165]

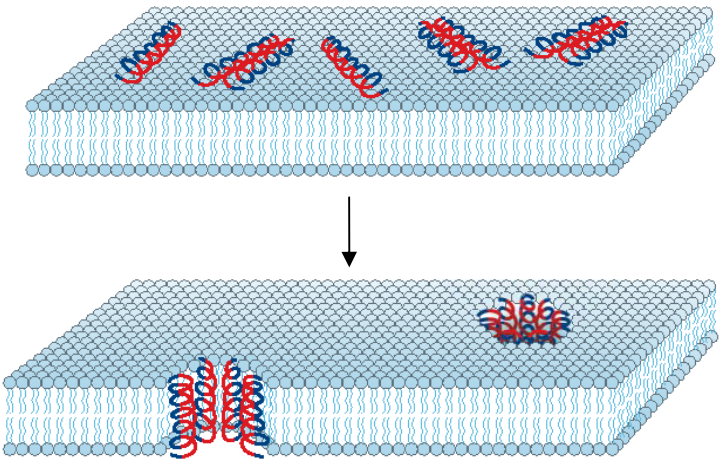

Figure 6.2: The barrel-stave model of alamethicin and bilayer membrane interaction. [174]

Alm forms voltage-gated multiconductance channels. A comprehensive description of the electrical activity of Alm can be found in several earlier articles. [165-167] The proposed models for voltage-dependent gating of alamethicin channel include voltage-dependent conformational change,[168, 169] voltage-dependent dipole change,[166, 170] voltage-dependent phase partitioning,[171] and voltage insertion.[172, 173] Among these, the most widely accepted is the "barrel-stave" model.[168, 170] According to this model, the Alm helical monomers are multimerized to form parallel transmembrane bundles surrounding a central aqueous pore, which is composed of 3-11 Alm molecules. Different conductance levels are determined by the different number of Alm monomers in the bundle. The peptide is preaggregated and bent at Pro 14. Ion channel gating occurs as a result of a voltage-dependent structural change which reorients the C terminus kink at Pro 14, leading to the conductive form of the channel. The channel is depicted as: the N-terminal parts of the helices pack together in a parallel

manner, while the pore widens at the C-terminus due to the kink generated by Pro 14, their helix dipole repulsions being overcome by their favorable interaction with the electrostatic field across the bilayer. Strong evidence that supports this model is the asymmetry of voltage activation of Alm channels. A positive potential on the *cis* side (the side where Alm is added) produces greater conductance than a *trans* positive potential, which indicates that reverse gating or insertion of the C-terminus is unfavorable. Due to the amphipathic nature of the Alm helices, the hydrophilic parts are oriented toward the central pore, while the hydrophobic parts are in contact with the surrounding lipids.[174] Furthermore, this model suggests that intermolecular H-bonds could be formed between the side chains of Gln7 of neighboring ALM monomers, further stabilizing the channels.

6.2 *Experimental*

The incorporation of Alm channels into tBLMs was probed in three ways.

One way is by solvent exchange. This method was introduced by Miller et al.[175] In a solvent exchange process, amphiphilic component or a mixture of different amphiphilic components is initially dissolved in a good solvent that is also miscible with water. The proper amount of solution is applied then onto a hydrophobic surface and allowed to incubate for a few minutes. When injected into an aqueous environment, the water-miscible solvent is replaced by water, and the amphiphilic molecules self-organize to form a monolayer on top of hydrophobic surface. In real experiments, the measuring cell is filled with the appropriate composition of lipids dissolved in ethanol (c =5 mg/ml). The formation of the lipid monolayer was initiated spontaneously by rinsing the measuring cell with standard buffer at a very slow speed. During several hours, impedance spectra were recorded until the system reaches a steady state. In practice, alamethicin and DPhyPC lipid were mixed in ethanol at different molar ratios. Again, for the build-up of the surface, the proximal lipid layer of tBLM was self-assembled from an ethanol solution of DPTL for 24 hrs on template stripped gold (TSG). The slide was then mounted onto the flow-cell for SPR and EIS measurements. The surface area determined by the electrochemical flow chamber is 0.28 cm^2. 0.15 µl ethanolic mixture of alamethicin and DPhyPC were applied to the DPTL/Au surface and incubated for 15 min. Then the measuring cell was rinsed with buffer very slowly.

Another way is first the formation of a DPhyPC tBLM by vesicle fusion, followed by the addition of an aliquot of alamethicin ethanolic stock solution. In practice, 20 µl of the

DPhyPC vesicle solution was injected in the measuring chamber filled with 1 ml 0.1M KCl solution, getting a final concentration of 0.04 mg/ml. After 4 to 12h the fusion process was complete. An aliquot of alamethicin ethanolic stock solution (2mg/ml, 2mM) was added to the membrane. The functional incorporation and channel formation could be shown by the change of resistance studied by EIS. The blocking effect of channels by channel inhibitor was also tested by exposure of channel containing tBLM to inhibitor amiloride.

In the third method of incorporation, alamethicin molecules were preloaded into vesicles to obtain the so-called proteoliposomes by the following procedure: DPhyPC and alamethicin at molar ratio of 15:1 were mixed in choloroform in a glass flask. The solution was frozen in liquid nitrogen while the solvent was vacuum-pumped for 24 hrs. Hydration of the dried mixed lipid film/cake was accomplished simply by adding proper amount of MilliQ water to obtain a lipid mixture of 2mg/ml. During the 1 hour hydration period with vigorous agitating at 60℃, a suspension of large multilamellar vesicles was formed. The suspension then went 6 times through shock freezing in dry ice and thawing at room temperature. Before use, the suspension was extruded 21 times through two stacked 50nm polycarbonate filters and the alamethicin proteoliposomes were applied to the DPTL monolayer surface in aqueous buffer and the second leaflet was formed by vesicle fusion. By this way, Alm was readily incorporated into tBLMs.

6.3 *Fusion of alamethicin containing proteoliposomes onto DPTL monolayer*

A series of measurements was conducted on the same TSG slide but at different areas to minimize the influence of difference of the slide. The experimental data are depicted as Bode plots in Figure 6.3(a) for alamethicin containing DPhyPC tBLMs prepared by solvent exchange at different Alm content. The obtained values are fitted using the model circuit, normalized to the surface area, and listed in the column plot of Figure 6.3(b). The background resistance of the pure DPhyPC bilayer itself is quite high, showing good electric sealing property. As the alamethicin percentage gets higher in the mixed tBLMs, the membrane resistance decreases.

The alamethicin molecule adopts a largely α-helical conformation, in the crystal, in nonaqueous solvents, and in the presence of lipid bilayers. During the exposure of DPTL

monolayer to an alcoholic solution of alm and DPhyPC mixture, the hydrophobic alkyl chains of DPTL and DPhyPC are extensively stretched (because ethanol is a good solvent) and interact adequately with the laterally hydrophobic region of peptide helices. Subsequent washing with electrolyte results in the formation of a distal layer, with the hydrophobic peptide regions aligning with the lipid core region of the lipid bilayer and the hydrophilic peptide regions form the interior region of the pore. From Figure 6.3, one can see that in the Alm containing tBLMs prepared by solvent exchange, the alamethicin channels are readily present and display their functionality of ion transport. At high peptide/lipid ratios, there are definitely more transmembrane pores present in tBLM, given the high conductivity of electrical current generated through the membrane.

(a) (b)

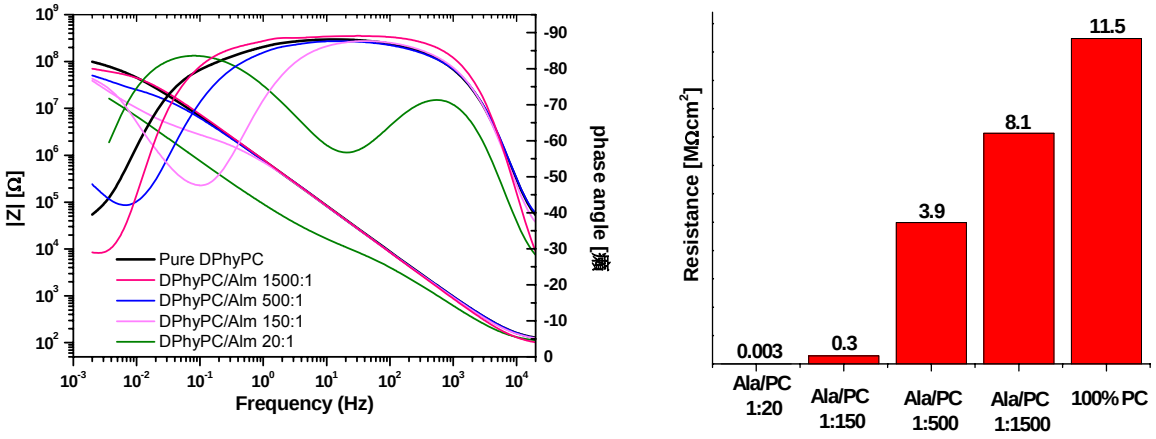

Figure 6.3: (a) EIS spectra of DPhyPC/DPTL tBLMs incorporated with Alms prepared by solvent exchange. All measurements were done in 0.1M KCl; (b) Membrane resistances as a function of mixing ration.

6.4 *Addition of Alamethicin onto the already formed DPhyPC tBLMs*

In a second series of experiments, a tBLM was formed by DPhyPC lipids. Alamethicin was added afterwards, as described in section 6.2. A typical situation after the alamethicin addition is shown in this figure 6.4. 25µl of an alamethicin stock solution (2mg/ml) were added to the membranes to give a final concentration of 0.05mg/ml in the measurement cell.

EIS is a very sensitive method to detect the membrane electrical conductivity. Here, only incorporated peptides that form transmembrane pores contribute to the measured decrease in the membrane resistance. One can see that even though there is no voltage applied, when Alm monomers at relatively high concentration were added to a preformed tBLM, the resistance of bilayer decreased very quickly (Figure 6.4a). The membrane resistance decreased further as a function of time. Upon equilibrium, a decrease by a factor of 100 compared to preformed DPhyPC tBLM can be seen. At the same time, an increase in capacitance can also be observed and the phase shift did not reach -90° anymore. It is assumed that the large number of incorporated channels give further influence to distribution of RC elements and therefore is seen as a deviative from an ideal capacitor.

(a)

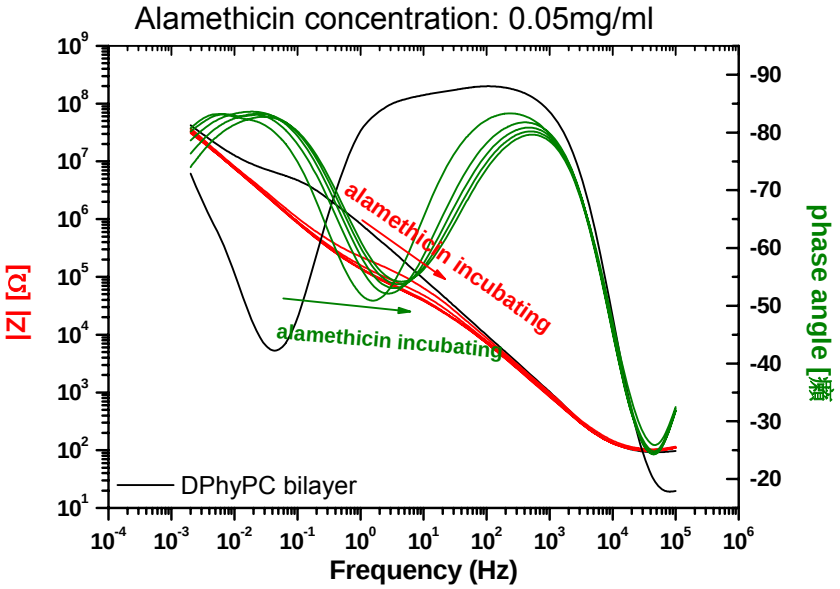

(b)

Incubating time (h)	R [MΩcm2]	R error	C [μF/cm2]	C error
0	1.49	12.1%	0.88	5.9%
0.5	0.046	8.5%	0.88	4.5%
1	0.023	8.8%	0.89	4.8%
1.5	0.018	9.3%	0.95	5.1%
2	0.016	9.7%	0.94	5.4%

Figure 6.4: (a) EIS plots of DPhyPC/DPTL tBLMs with Alms incorporation afterwards. All measurements were done in 0.1M KCl; (b) Membrane resistances as a function of incubating time.

Alamethicin is proposed to aggregate and insert into the bilayer in a concentration and voltage dependent manner. In this experiment, no voltage was applied during Alm adsorption. Only by applying a high concentration, channel formation can be triggered.

For EIS Bode plots it takes around 20 mins to run one cycle measurement along the preset frequency range and one might miss the most crucial kinetic information during the frequency sweep. Another series of experiments were conducted aiming to capture the real-time process of peptide-membrane interaction.

To know how the kinetics was measured, one needs to firstly take a look at the bode plot of DPhyPC tBLM, choose three reasonable frequencies at which impedance is most sensitive to kinetic changes of the bilayer impedance, and set up the potentiostat to measure the impedance and phase as a function of time at these three frequencies. The reason to take 3 frequencies is that if the change is large, at the fixed frequency, the impedance value may already reach the minimum while the change is still going on.

In this case, 3 frequencies, 10, 1, and 0.1 Hz were chosen to record the kinetic process as shown in Figure 6.5(a). The impedance kinetics obtained is presented in Figure 6.5(b).

As one can see from Figure 6.5(b), at a relatively low Alm concentration the impedance change is very small at 0.1Hz, and almost invisible at 1 Hz and 10 Hz. If a much higher concentration is applied a change can be seen for all 3 frequencies. The 0.1 Hz curve reaches minimum first, then followed by the 1 Hz curve, which is within expectation if one imagines

(a)

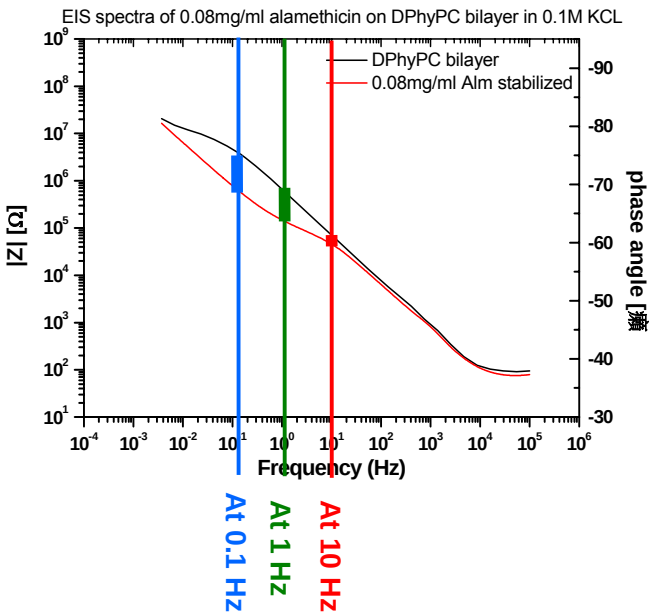

the trend of impedance change. The cell was rinsed before the 10 Hz curve was stabilized.

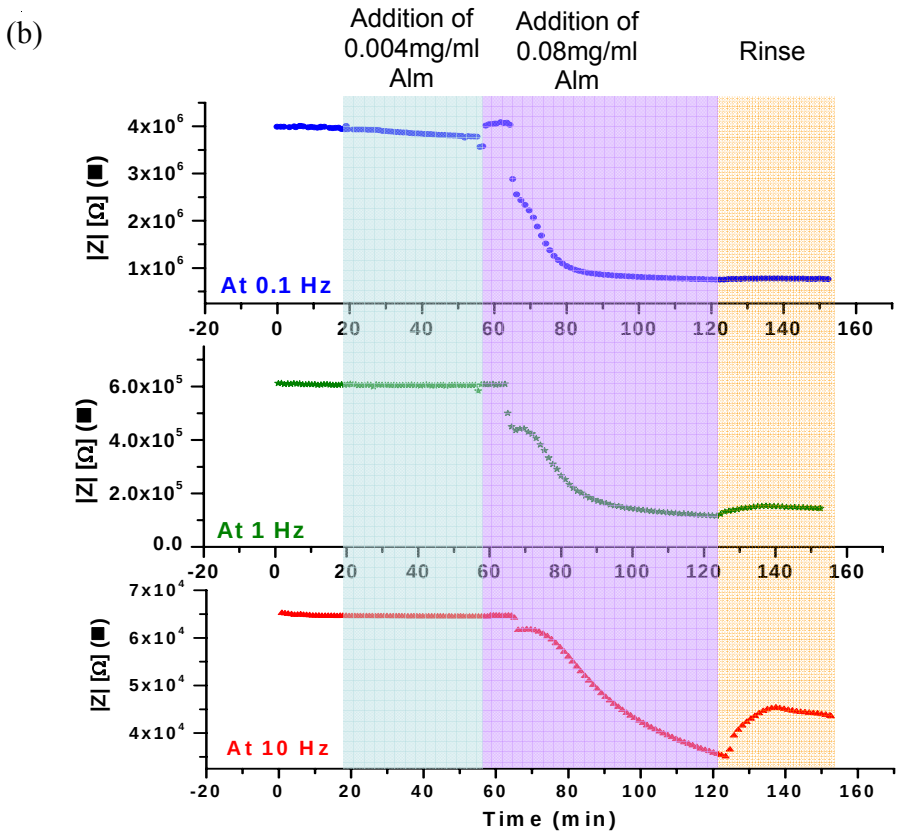

Figure 6.5: (a) Selection of frequencies at EIS Bode plots at which kinetics is most sensitive to impedance changes; (b) Kinetics of Alm additon onto preformed DPhyPC tBLM (at 0V) seen by impedence as function of time at different frequencies.

The voltage dependence of the conductance was measured afterwards and is shown in Figure 6.6. Typical bode plots were selected. The black curve refers to sealed DPhyPC bilayer prepared by solvent exchange. The red one corresponds the layer after alm incorporation which happened without applying a voltage. The blue and green curves represent measurements conducted at 0.3V and -0.2V, respectively. The simulated bilayer resistance and capacitance values averaged by 3 measuring cycles are summarized below. Impedance values measured at different voltages for 3 cycles indicate a reversible dependence of membrane resistance on applied voltages. The resistance values at a fixed voltage drift slightly, but still within an acceptable range. The drift can be accounted for by changes in the electrical potential distribution as ions accumulate in the submembrane space during the forward or backward potential sweep. The accumulation of potassium cations in the

submembrane space is expected to cause the applied potential to drop across the oxyethylene spacer rather than the lipid layer.

(a)

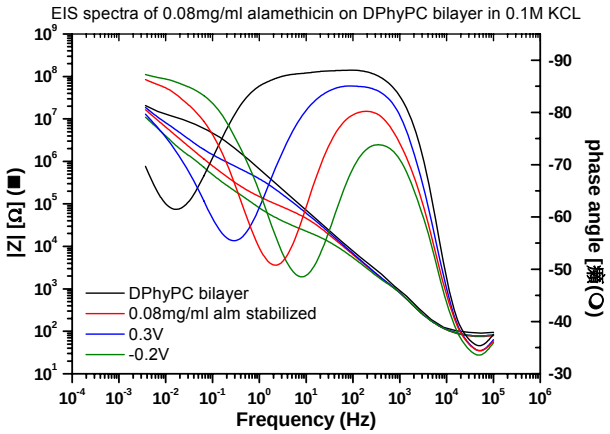

(b)

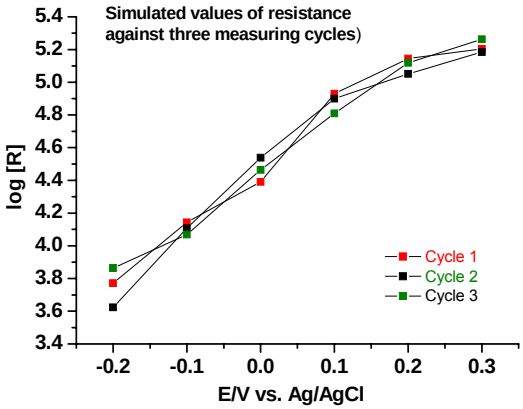

(c)

State	R [MΩcm2]	R error	C [μF/cm2]	C error
DPhyPC bilayer	3.1592	4.50%	0.8754	2.50%
Alm stabilized 0V	0.0246	5.20%	0.9047	3.20%
Alm stabilized 0.3V	0.1602	6.70%	0.9317	3.60%
Alm stabilized -0.2V	0.0059	5.90%	0.9568	4.50%

Figure 6.6: (a) EIS spectra of Alm incorporated tBLM at different bias; (b) Simulated resistance at different bias for 3 cycles; (c) Membrane resistances as a function of applied bias

Based on the experimental results, we propose the following: On a tBLM platform, in the absence of a bias voltage, the addition of Alm at high peptide/lipid ratio from membrane top (*cis* addition) may result in some Alm monomers binding parallelly to lipid bilayer surface and some of them inserting into the bilayer, forming transmembrane pores. If a negative bias is applied to Au electrode (equal to *cis* positive potential), the transmembrane electric field induces more laid Alm monomers to insert into the lipid bilayer, overcoming their helix dipole repulsions and encouraging higher degree of aggregation (in size and number of aggregates) in the membrane. This results in the increase of macroscopic conductance of the planar bilayer. If a positive bias is applied to Au working electrode (equal to *cis* negative potential), the transmembrane electric field interacts with the pore-widening C-terminus of transmembrane peptides and this either reduces the number of peptide aggregates or reduces

the number of peptides in the aggregate, which may finally result in the increase in membrane resistance to current flow.

Amiloride is an inhibitor for alamethicin channels.[176] The measurement of the amiloride blocking effect on Alm channels is displayed in Figure 6.7. The addition of amiloride did cause an increase in membrane resistance, indicating the partial blocking of the conducting channels. After inhibition, the resistance of the membrane shows much less dependence on the applied voltages.

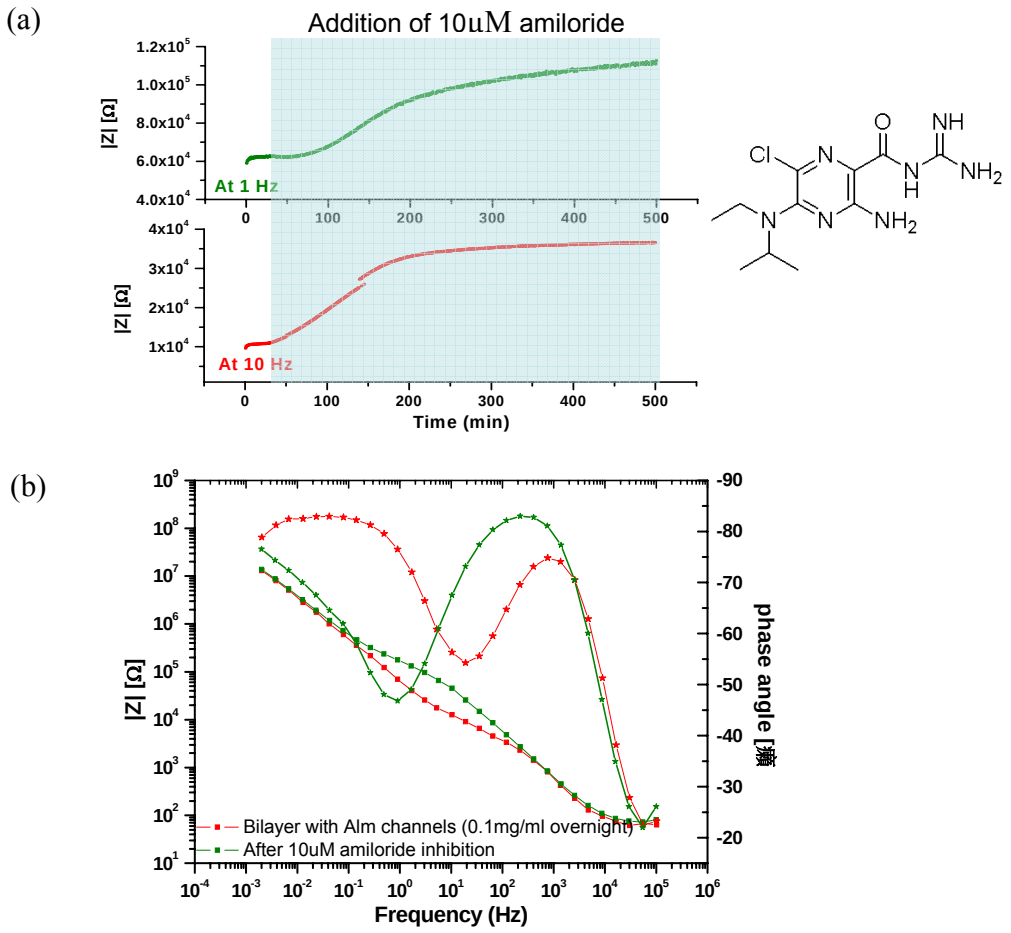

Figure 6.7: (a) Chemical structure of amiloride and EIS kinetics of inhibition by 10μM amiloride; (b) EIS spectra of before and after amiloride inhibition on Alm/DPhyPC bilayer.

6.5 *Fusion of alamethicin containing proteoliposomes onto DPTL monolayer*

In this series of experiments, monolayers were prepared from ethanol solution of DPTL. Alamethicin molecules were reconstructed into DPhyPC vesicles at a molar ration of 1:15 (refer to section 6.2 for details). Bilayers were formed by fusion of alamethicin reconstructed proteoliposomes. A typical experimental result is shown in Figure 6.8.

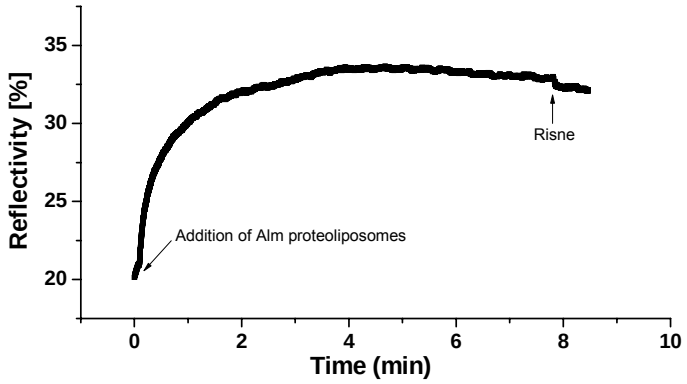

Figure 6.8: SPR kinetics of the Alm preloaded vesicle fusion and bilayer formation.

The liposome fusion process with DPTL monolayer was monitored by SPR (Figure 6.8). The reflectivity increased with time, first rapidly over about 1.5 hrs followed by a long period before the process reached equilibrium. Angular scans before and after fusion was analyzed using a multilayer simulating system. Taking a refractive index of n = 1.45 for DPhyPC, the obtained increase of membrane thickness is 3.3±0.1 nm, which agrees with the estimated length of fully stretched lipid DPhyPC molecule.

EIS was also utilized to record the fusion process where an increase in resistance and a decrease in capacitance could be observed. Typical DPhyPC tBLMs have resistances around 2-12 MΩcm^2. However, an EIS sweep taken after the liposome fusion equilibrium results in a resistance of only 0.24 MΩcm^2, which clearly is due to the incorporation of functional alamethicin peptides that permit the transport of ions through the membrane and therefore reduce its resistance.

Once the incorporation of Alm channels was achieved by fusion of preloaded liposomes, the voltage-dependence of channel conductance was further studied by EIS. As shown in Figure 6.9, the Au working electrode was biased at different potentials and the corresponding EIS curves in 0.1M KCl and 0.1M TMAC (Tetramethyl ammonium chloride, $(CH_3)_4N^+Cl^-$) were thus recorded.

Figure 6.9 (a) and (b) refer to EIS measurements done at different dc potentials from -0.2V to 0.4V in KCl and TMAC buffer solutions, respectively. For both buffers, when the applied voltage was increased, the impedance of the bilayer also increased. The resistance of alamethicin reconstructed bilayer displays strong dependence on applied voltage.

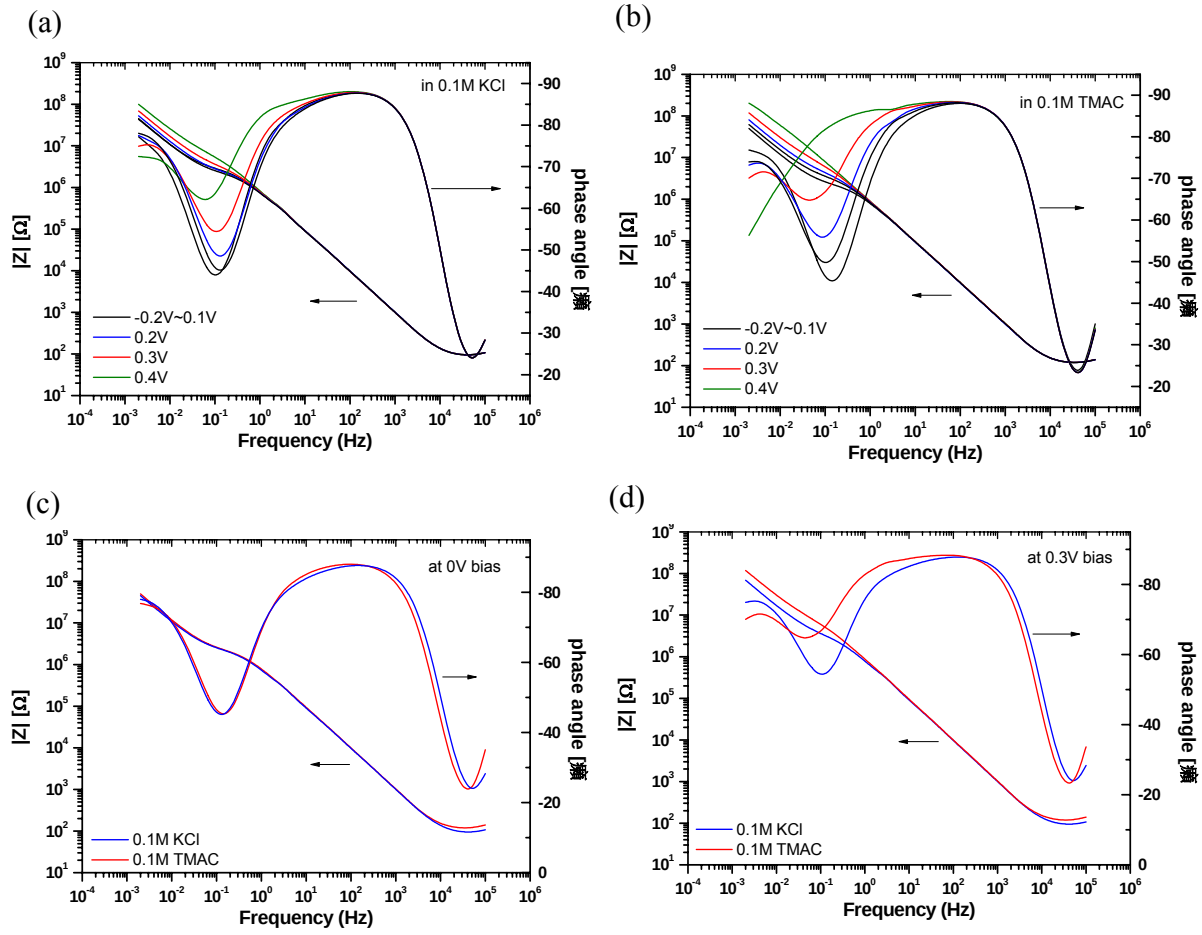

Figure 6.9: EIS spectra of the so- formed Alm incorporated tBLM at different bias in (a) 0.1M KCl and (b) 0.1M TMAC; For easy comparison, EIS spectra in KCl and TMAC are put together at bias of (c) 0V and (d) 0.3V.

For easy comparison, the EIS plots are compiled in a different way. Measurements in the two different buffers at the same dc potencial were put in one graph, Figure 6.9c at 0V, and Figure 6.9d at 0.3V. One can see that at 0V, the alamethicin reconstructed bilayer shows almost the same resistance in the two buffers, indicating a high level of conductance state, with almost the same high permeability to K^+ and also to much more bulky TMA^+. As the dc potential is increased, the resistance of layer displays difference, much higher in TMAC than

in KCl. This might be an indication that as the potential increases, alamethicin is going through the transition from high conductance state to low conductance state, and gradually displays the different permeability to ions with different size.

Here is some comparison of the two cases of alamethicin incorporation, one is DPhyPC bilayer formation first and alamethicin addition afterwards, the other case is mixing DPhyPC and alamethicin thoroughly to prepare proteoliposomes and obtaining the alamethicin containing bilayer spontaneously by proteoliposome fusion. In case 1, the resistance of the bilayer after alamethicin addition show dependence on dc potential in all measured voltage range from -0.2V to +0.3V. In case 2, the resistance only displays this voltage dependence from 0.1V on.

A possible explanation is that in case 2, during the proteoliposome preparation, alamethicin and DPhyPC were thoroughly mixed and the extraction of solvent was done in freezing condition. This might help to better keep the well ordered orientation of alamethicin in bilayer. When vesicles fuse on the surface, the pores formed by alamethicin aggregates in bilayer might already have been in a state of high conductance. A negative voltage stimulus will not be able to further promote the permeability level, at least for K^+ and TMA^+ ions. But a positive voltage stimulus can result in a more rapid pore disturbance or disappearance compare to the rate of pore formation.

6.6 *Conclusion*

The functional incorporation of the ion channel alamethicin by different methods into the here used tBLMs was demonstrated. Electrochemical impedance spectroscopy displays the direct relationship between the membrane sealing property and the amount of peptide incorporated by changing the ratio of Alm and lipid during solvent exchange. If Alm was added into the preformed tBLMs from the top side, the pores' voltage dependence could be investigated by EIS with a dc bias. The addition of inhibitor amiloride can partially block the Alm channels and results in increase of membrane resistance. The macroscopic selectivity of Alm channels for small potassium cations and bulky tetramethylammonium cations was also studied at different bias and it was shown that at high positive dc bias (*cis* negative) Alm channels stay at relatively low conductance levels and show higher permeability to potassium than to tetramethylammonium. The presented tBLMs provide a platform for the study of ion transport phenomenaIn of channel peptide alamethicin.

7. Mimicking bacterial membranes: a model platform to study antimicrobial peptides

7.1 *Introduction*

Lipopolysaccharides (LPS) are a major constituent of the outer cell wall of gram-negative bacteria. They are the active component of gram-negative bacterial endotoxins [177-179] with profound immunostimulatory and inflammatory capacity. LPS plays also a major role in pathogenesis.[180] The amphiphilic structure of LPS consists of a hydrophilic polysaccharide part, which is covalently bound to the hydrophobic lipid A.[181-184] The structures of LPS and lipid A are schematically given in Figure 7.1a and b. The polysaccharide part can be divided into two subdomains, the core region and the side chain, called O-antigen that is composed of a sequence of repeating units of identical oligosaccharides.[185, 186]

The O-antigen has been shown to be immunogenic [187, 188] while toxicity of the molecule is associated with the lipid component.[189] The lipid A component is in general composed of a phosphorylated β-1,6-linked D-glucosamine disaccharide that carries up to six or seven acyl residues.[190]

Antibiotics are widely applied to food and clinical uses to control many bacterial infections. However the increasing antibiotic resistance, which is caused by extensive and unnecessary clinical use, as well as the lack of new classes of antibiotics make it necessary to look for and develop new antimicrobial drugs.[191] Emerging potent candidates are antimicrobial peptides. Different from conventional antibiotics which either disrupt the bacterial wall synthesis or destroy peptide synthesis, antimicrobial peptides mainly target the bacterial membrane, make it permeable and eventually lead to bacterial death. Because it is difficult for bacteria to develop a new membrane system to survive, antimicrobial peptides have been considered a promising drug candidate as a substitute or addition for conventional antibiotics.

Antimicrobial peptides have been widely found in nature including insects, amphibians, mammals and humans. Antimicrobial peptides have the ability to defend against a variety of microorganisms, including gram-positive bacteria, gram-negative bacteria, fungi, protozoa, some tumors and viruses. Antimicrobial peptides are believed to perform their functions via a non-specific mechanism by directly targeting bacterial membranes to induce non-receptor-mediated membrane permeation.[192] They either perturb the membrane to form pores/channels

and permit a leakage of cellular components as well as dissipating the electrical potential of the membranes or disrupt the membrane in a detergent like manner.[193]

Because many natural antimicrobial peptides kill bacteria and are toxic to mammalian cells, few of them are available for medical use. An alterative way to develop new drugs is to design new antimicrobial peptides based on known peptide sequences and structures. Regardless of the distinct origins, primary sequences, biological activities and secondary structures, most antimicrobial peptides share some common characteristics. They are short peptides, consisting of less than 50 amino acids in length. Their small size makes chemical synthesis possible for a variety of investigations. Most antimicrobial peptides are cationic with +2 to +9 charges due to the presence of lysine and arginine residues and have amphipathic structures, which spatially separate hydrophobic and hydrophilic amino acids to facilitate the interaction with membranes. The charge and the amphipathicity are crucial factors for determining the biological activities of antimicrobial peptides.

A lot of effort has been put to design novel antimicrobial peptides in the past years.[189] Among these, the peptide named V4 has been shown to have high antimicrobial activity, low cytotoxic activity and low hemolytic activity compared with other designed and natural peptides.[194, 195] V4 shows an amphipathic cationic pattern BHPHB (B: basic; H: hydrophobic; P: polar residue, respectively) with a β-sheet conformation, which is proposed to have a high affinity to the endotoxin LPS.[195] The proposed interaction mechanism of V4 and a membrane includes several steps.[196] V4 binds or absorbs driven by electrostatic interactions onto the bacteria membrane surface. Therefore, the charge of the membrane plays a crucial role whether or not interaction occurs. With increasing peptide concentration on the membrane surface, V4 begins to insert into the membrane and undergoes translocation. Hydrophobic interaction plays an important role during this process. If the peptide/lipid ratio further increases, V4 completes the translocation from the outer layer of the membrane to the inner layer and disrupts the membrane eventually. This membrane disruption causes the leakage and final bacterial death.

The different degrees of membrane disruptions caused by V4 might be based on a variety of different factors: membrane charge, membrane surface topography, or types of lipid fatty acid. The membrane charge is proposed to be an important aspect because of the strong electrostatic interaction between the negative charges of the membrane and positive charges of the V4 peptide. However, the fully detailed pathways of peptide/membrane interactions are still unclear.

Screening for high antimicrobial activity, low cytotoxicity and low hemolytic activity can be used for selection of potential drug candidates. Therefore, we used the well defined model artificial membrane -- tethered bilayer lipid membrane (tBLM) architecture in order to probe the interaction of the peptide with various lipid compositions. tBLMs are robust and versatile model membrane architectures that can mimic certain properties of biological membranes.[41, 135, 138, 139, 197, 198] A tBLM with incorporated LPS and lipid A has been used to mimic bacteria membranes and probe the interaction of the designed peptide V4 to different membranes. The aim is to examine the selectivity of antimicrobial peptides killing bacteria, not harming mammalian cells, and to unravel the mechanism of the action of antimicrobial peptides, which are the keys for the rational design of novel antimicrobial drugs.

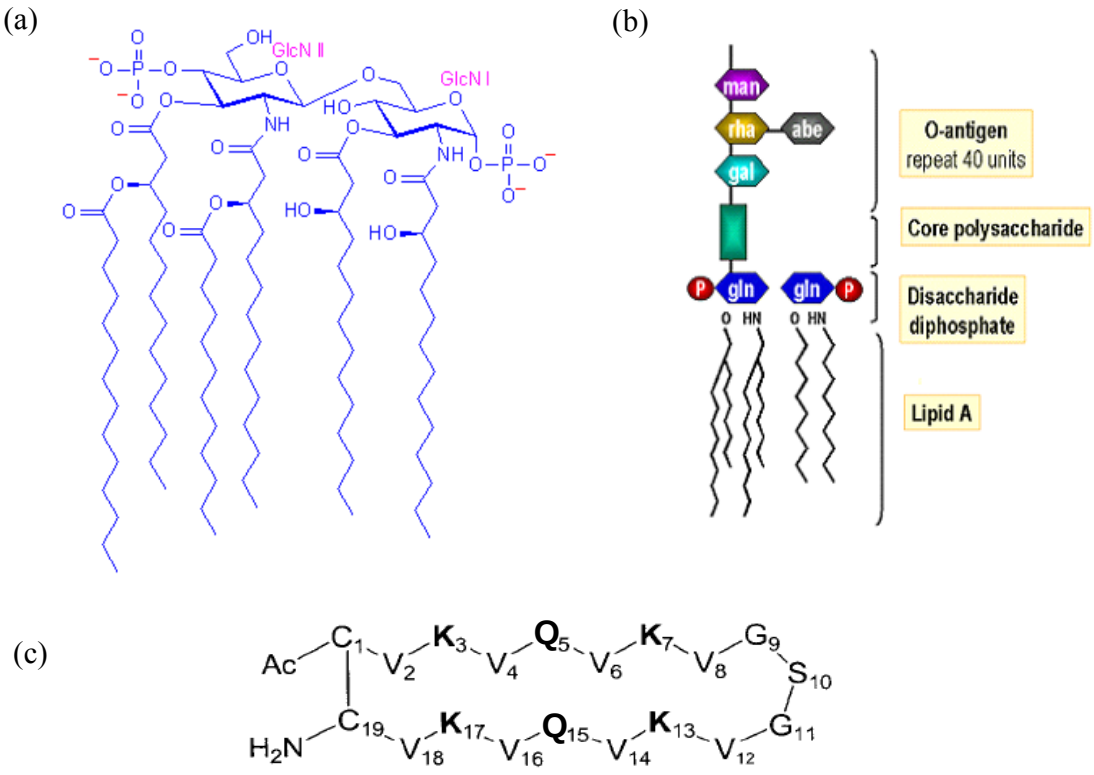

Figure 7.1: (a) Structure of lipid A; (b) Schematic of LPS, consisting of lipid A, polysaccharide and O-antigen; (c) Sequence of cyclic cationic peptide V4.

7.2 *Experiments*

The anchorlipid DPTL has been synthesized as described earlier. 1,2-Di-O-Phytanyl-sn-Glycero-3-Phosphocholine (DPhyPC) and 1,2-Diphytanoyl-sn-Glycero-3-[Phospho-rac-(1-

glycerol)] (DPhyPG) (Avanti Polar Lipids, Inc., Alabaster, AL) were used as received for the preparation of liposomes. Lipopolysaccharide from Escherichia coli strain 0111:B4 (LPS) and lipid A (LA) were purchased from Sigma. Preparations of rabbit polyclonal antibodies (pABs) of IgG isotype specific for E. *coli* O111 O-antigen and Cy5-labeled goat pABs to rabbit IgG as secondary antibodies were obtained from Abcam (Cambridge, MA).

The sequence of V4 is CVKVQVKVGSGVKVQVKVC with cyclization by a disulfide bond at the two terminal cysteines (C) [194, 195]. Four lysine (K) residues provide high net positive charge and eight valine (V) residues make this peptide highly hydrophobic. The peptide V4 and its chromophore-labeled form V4-S0387 (S0387 λ_{EX} = 646nm, λ_{EM} = 667nm) were synthesized by PANATecs (PANATecs GmbH, Tübingen) with a purity of about 95%.

The inner leaflet of the tBLM was formed by self-assembly of DPTL thiolipids on gold coated substrates. The second leaflet was prepared either by liposome fusion or by solvent exchange. For the LPS antibody detection, the outer leaflet was completed by fusion with small unilamellar DPhyPC vesicles containing LPS molecules at a molar ratio of 1:30. For the peptide V4's antimicrobial behavior investigation, the outer leaflet containing the lipid A moiety was prepared by fusion of DPhyPC vesicles loaded with lipid A at a molar ratio of 1:20. Solvent exchange was utilized to prepare DPhyPG/DPhyPC hybrid tBLMs. Briefly, 15µl lipid ethanolic solution (5mg/ml) was applied on DPTL monolayer (with surface area of 0.28 cm^2) and incubated for 10 min, followed by a very slow rinsing with buffer solution.

DPhyPC, Lipid A/DPhyPC (1:20) vesicles were prepared in the following way: Lipids were thoroughly dissolved in chloroform. The solution was dried under a stream of Argon and then freeze-dried in vacuum. MilliQ water was added to re-dissolve the lyophilized lipids to obtain an aqueous suspension at a concentration of 2mg/ml. The resulting multilamellar vesicles were subject to 5 freeze/thaw cycles followed by extrusion through 50nm polycarbonate membrane filters 20 times using a mini-extruder syringe device (Avanti Polar Lipids). Fusion of vesicles was carried out at 30°C at a final concentration of 0.02 mg/ml.

Since LPS has a low solubility in organic solvents, LPS were mixed with DPhyPC vesicles in MilliQ water at mole ratio of 1:30 and sonicated for 10 min in order to obtain LPS/DPhyPC vesicles.

7.3 *Results and discussion*

7.3.1 SPFS detection of LPS antibodies with tBLM

We studied the binding of antibodies against LPS by using a tBLM with LPS mixed in the distal leaflet of the membrane. Therefore, the O-antigen part of the polysaccharide is exposed

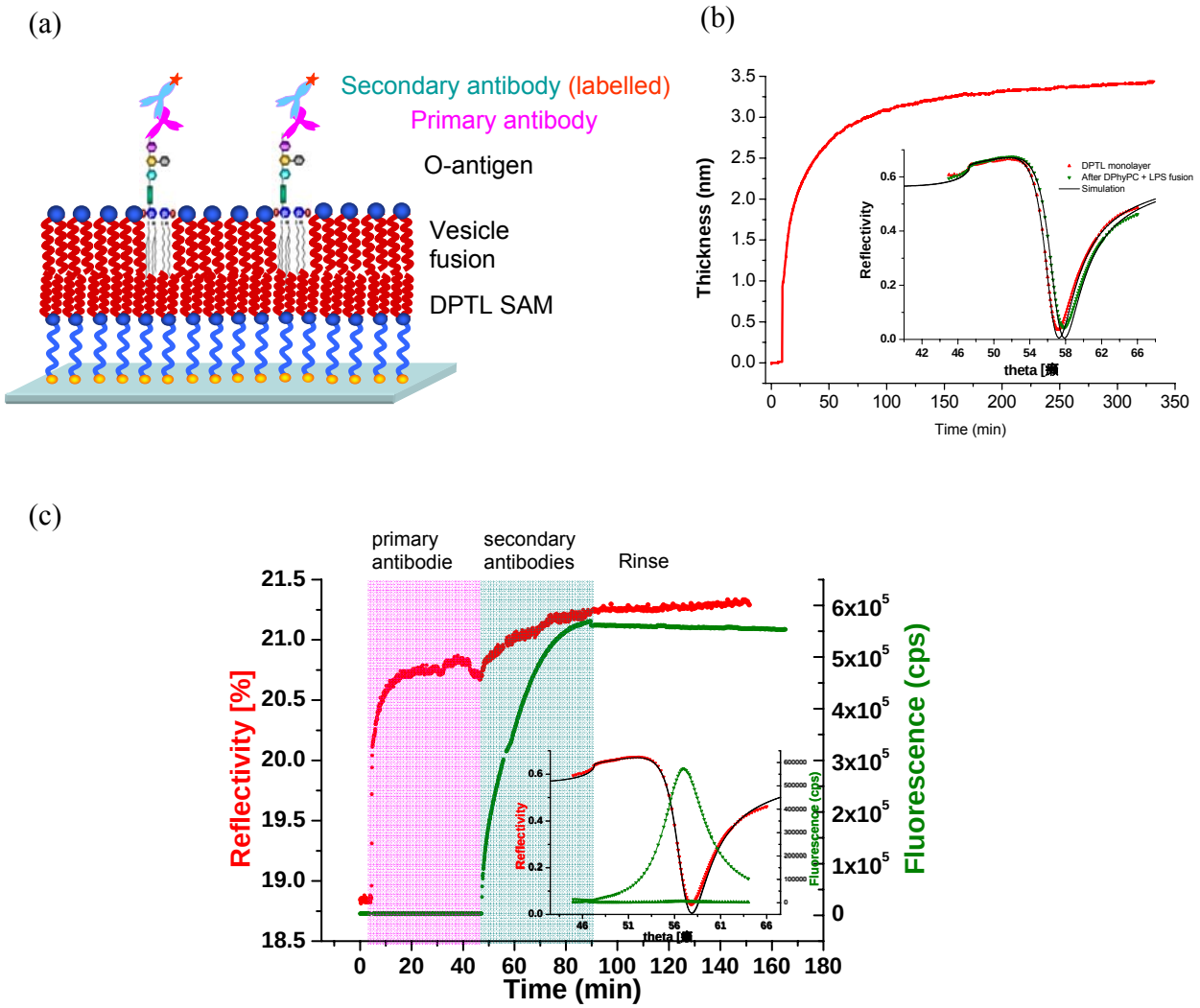

Figure 7.2: (a) Schematic presentation of the sensor surface architecture: Onto an evaporated gold film a DPTL SAM was formed, which supported the outer phosphor lipid layer to complete tBLM. The O-antigen part of the incorporated LPS is exposed to buffer solution for antibody binding. (b) Kinetic SPFS curve taken at a fixed angle of observation during vesicle fusion, documenting also at inset the angular scans of the reflected intensity before and after vesicle fusion. The resulting angular resonance shift is clearly visible. (C) Kinetic SPFS curve taken at a fixed angle of observation during additions of primary and labeled secondary antibodies. The inset angular scans indicate the fluorescence emission at the maximum surface plasmon excitation.

to the buffer solution (Fig 7.2a). The binding kinetics could be studied by SPR (Fig 7.2b), the thickness of the film was evaluated from angular scans before and after vesicle fusion. (Fig 7.2b inset) The thickness of the membrane increases with time until a final thickness of the distal layer of 3.5±0.1 nm is reached, slightly higher than a pure DPhyPC layer (~3.3nm), which is, probably due to the presence of LPS.

SPR and SPFS were then used to monitor the specific binding of the primary and labeled secondary antibodies to the O-antigen fraction of LPS-containing tBLM interface (Fig 7.2c). Due to the rather diluted LPS in the membrane, the addition of primary antibodies leads to a small shift in the SPR signal. Similarly, the SPR signal hardly changes upon addition of the secondary antibody. SPR is proportional to the amount of bound material on the surface, which in the present case is rather limited. However, the fluorescence signal shows a significant increase upon binding of the labeled antibody. The SPFS signal is in accordance with the excitation of surface plasmon and stable upon rinsing (Fig 7.2c inset). The control experiment with addition of the antibodies to a pure DPhyPC membrane showed only little non-specific binding (data not shown).

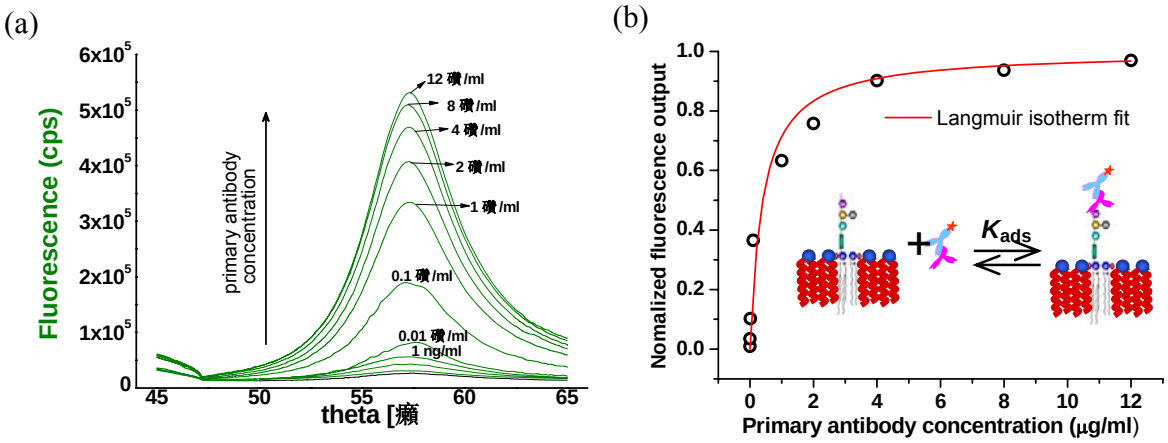

Figure 7.3: (a) Series of SPFS angular scan curves taken at different concentrations of primary antibodies. (b) Normalized FI versus concentration for the adsorption of LPS primary antibody to LPS-embedded tBLM. The solid line is fit of the data to Langmuir isotherm. The figure inset shows a schematic of antibody adsorption onto surface-attached antigens.

The quantitative analysis of the binding affinity of a specific antibody is important both for the understanding of the limits of detection in real biological samples and for the development of better antibodies for the antigens. Therefore, a series of SPFS measurements with various primary antibody concentrations ranging from 1×10^{-13} M to 8×10^{-8} M have been performed (Fig 7.3 a). The specific adsorption of the 130 kDa antibodies can be detected easily down to concentrations of 1 ng/ml. The fluorescence intensity (FI) increases with increasing antibody concentration up until it reaches a saturation level. In order to obtain a quantitative analysis of the binding, the SPFS signals were normalized between the background level and the saturated intensity corresponding to full binding site coverage. Each data point was obtained

at equilibrium and is the average of measurements on three different SPFS chips. If plotted against the antibody concentration, the FI can be analyzed using a Langmuir isotherm. An affinity constant of $K_A = 3\times10^8$ M^{-1} could thus be obtained (Fig 7.3b).

7.3.2 V4 binding to DPhyPC/DPhyPG mixed tBLMs

The influence of charges in the membrane on the interaction with the V4 peptide has been

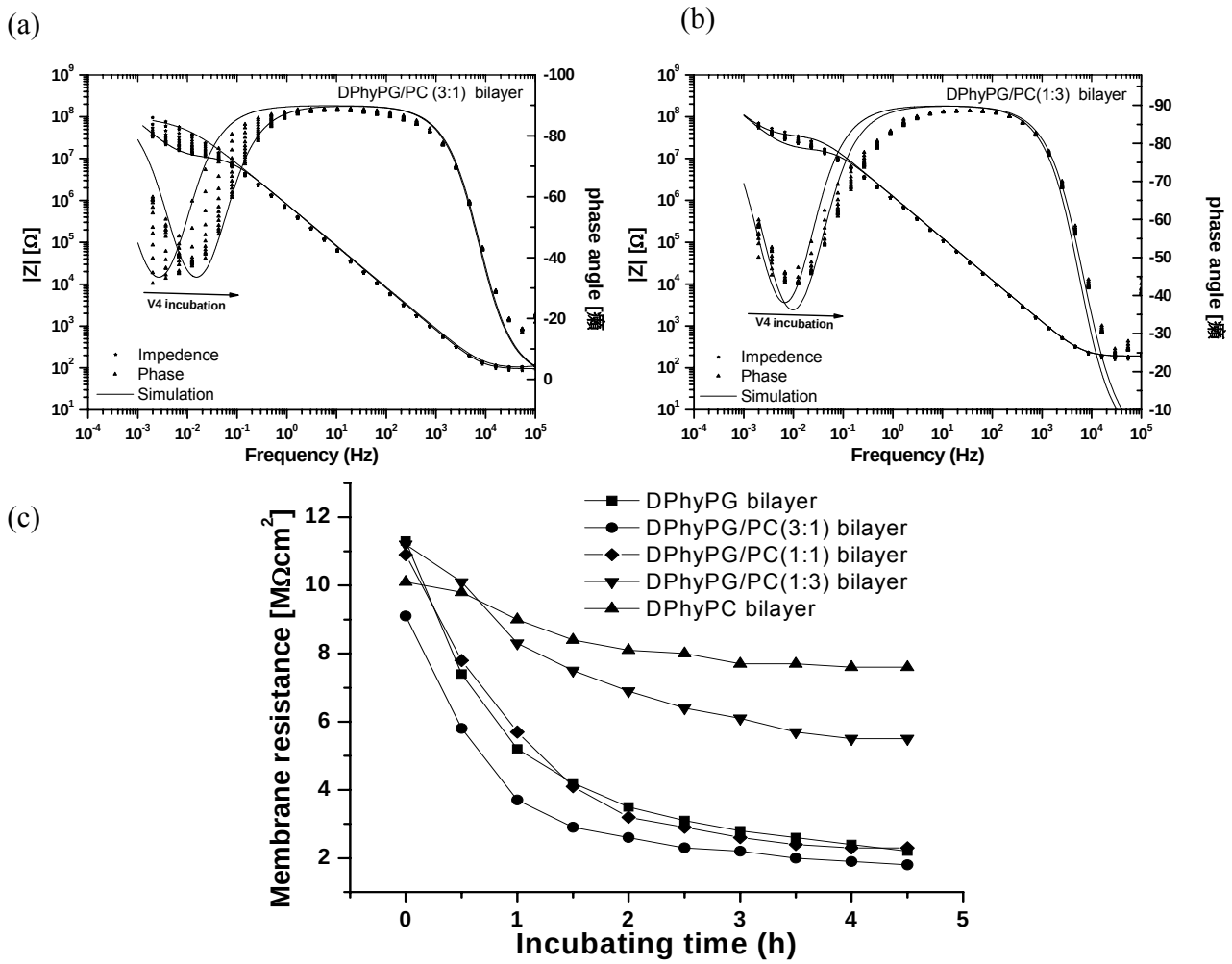

Figure 7.4: Representative Bode plots from EIS measurements recording the change of membrane electric properties by addition of 10 μM V4 into (a) DPhyPG/DPhyPC 3:1 tBLM and (B) 100% DPhyPC tBLM. (C) Comparison of V4 caused disruptions of membranes with PG/PC ratios. The concentration of V4 is 10 μM.

studied using EIS. Membranes with different DPhcPC/DPhyPG ratios and therefore different charge densities have been prepared. DPhyPG and DPhyPC have the same length and structure of fatty acid, but DPhyPG is terminated by a glycerol unit and has a net negative

charge, while the choline group of DPhyPC leads to a zwitterionic lipid. Bilayers were prepared by solvent exchange.

The interaction of the peptide with the membrane can be clearly seen in the impedance data. The data can be analyzed using a simple R(RC)C equivalent circuit. The tBLMs before addition of the peptide show a high initial resistance in the order of 7-12 MΩ cm^2, which is in good agreement with previous experiments and corresponds to values known from planar lipid bilayer, when normalized to the surface area. The electrical properties of the membrane change with increasing incubation time (Fig 7.4a and b). The membrane resistance shows a clear decrease with increasing incubation time (Fig 7.4c). The effect is significantly more pronounced in DPhyPG rich membranes, showing a preference of the peptide for negatively charged surfaces. It is not absolutely clear yet, whether the peptide incorporates into the membrane to form conductive pathways or whether it disturbs the membrane and thus causing a decrease in resistance. However, the findings reveal that electrostatics plays a significant role in the interaction between V4 and the membrane. The positive charges of V4 (4 lysines), similar to many antimicrobial peptides, facilitate the absorption or binding to the negatively charged lipid head groups and cause thus higher peptide-membrane interactions.

7.3.3 V4 binding to DPhyPC/Lipid A mixed tBLMs

In order to further elucidate the influence of the lipid composition on the peptide binding, we incorporated the lipid A in a molar ration of 1:20 into a DPhyPC-tBLM. This should mimic a bacterial cell membrane more than pure DPhyPC membranes. Impedance spectra of the lipid A/DPhyPC and of pure DPhyPC tBLMs were recorded before and after the addition of V4 (Fig 7.5a and b). The data could be again analyzed by an equivalent circuit and the obtained values for membrane resistance and capacitance were normalized to the surface area of the electrode. The membrane resistances were in the order of 5-11 MΩcm^2, both for the mixed as well as for the pure membranes. Upon addition of the peptide to the membrane, the resistance dropped rapidly by more than an order of magnitude within two hours in the case of the lipid A containing membrane. The pure DPhyPC membrane showed for the same amount of added peptide only a slight decrease in membrane resistance, indicating that V4 has a higher affinity and more disruptive effects for the lipid A-containing tBLM.

Compared to the mixed DPhyPG/DPhyPC membranes, V4 shows a higher affinity to the mixed lipid A containing membranes. This suggests that not only the charge is the driving force for the peptide/membrane interactions. One possibility might be steric effects. The

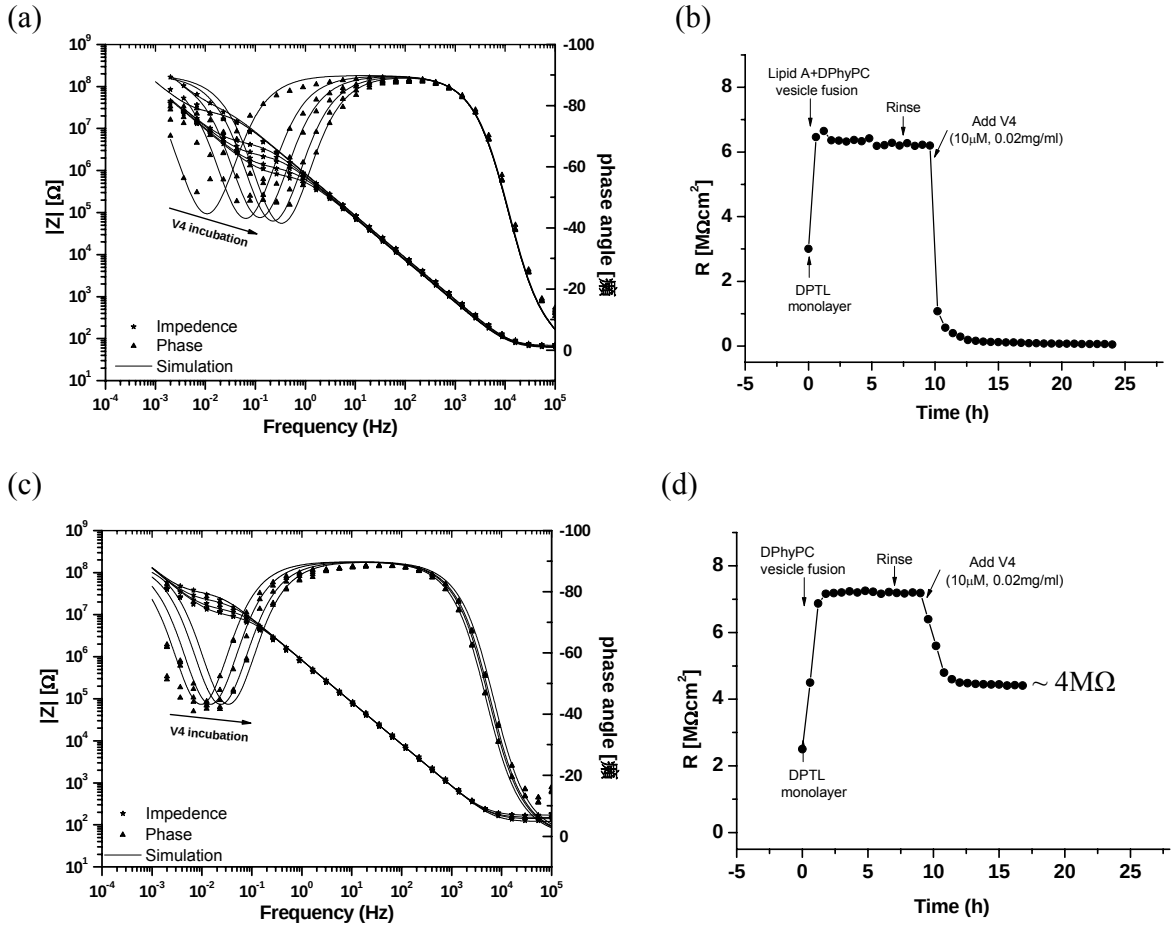

Figure 7.5: Representative Bode plots from EIS measurements recording the change of membrane electric properties by of 5 μM V4 into (a) Lipid A/DPhyPC (1:20) tBLM and (B) 100% DPhyPC tBLM. Documented also are calculated resistance plots from fitted EIS data as a function of peptide-membrane reaction time.

multiple charges of the lipid A are located further off the bilayer than in the phospholipid bilayer. This might favor the interaction with the peptide through the formation of ion-pairs between the anionic phosphates of lipid A and the cationic side chains of V4. V4 induces membrane disruption; however the detailed pathway on the molecular level is still not clear. Nevertheless, we could clearly distinguish between membrane disrupting, penetrating or disturbing effect of the V4 peptide in negatively charged membranes compared to uncharged membranes. These findings can give useful information for the design of novel antimicrobial

peptides that combine a high efficiency against bacteria and a low toxic activity for mammalian cells.

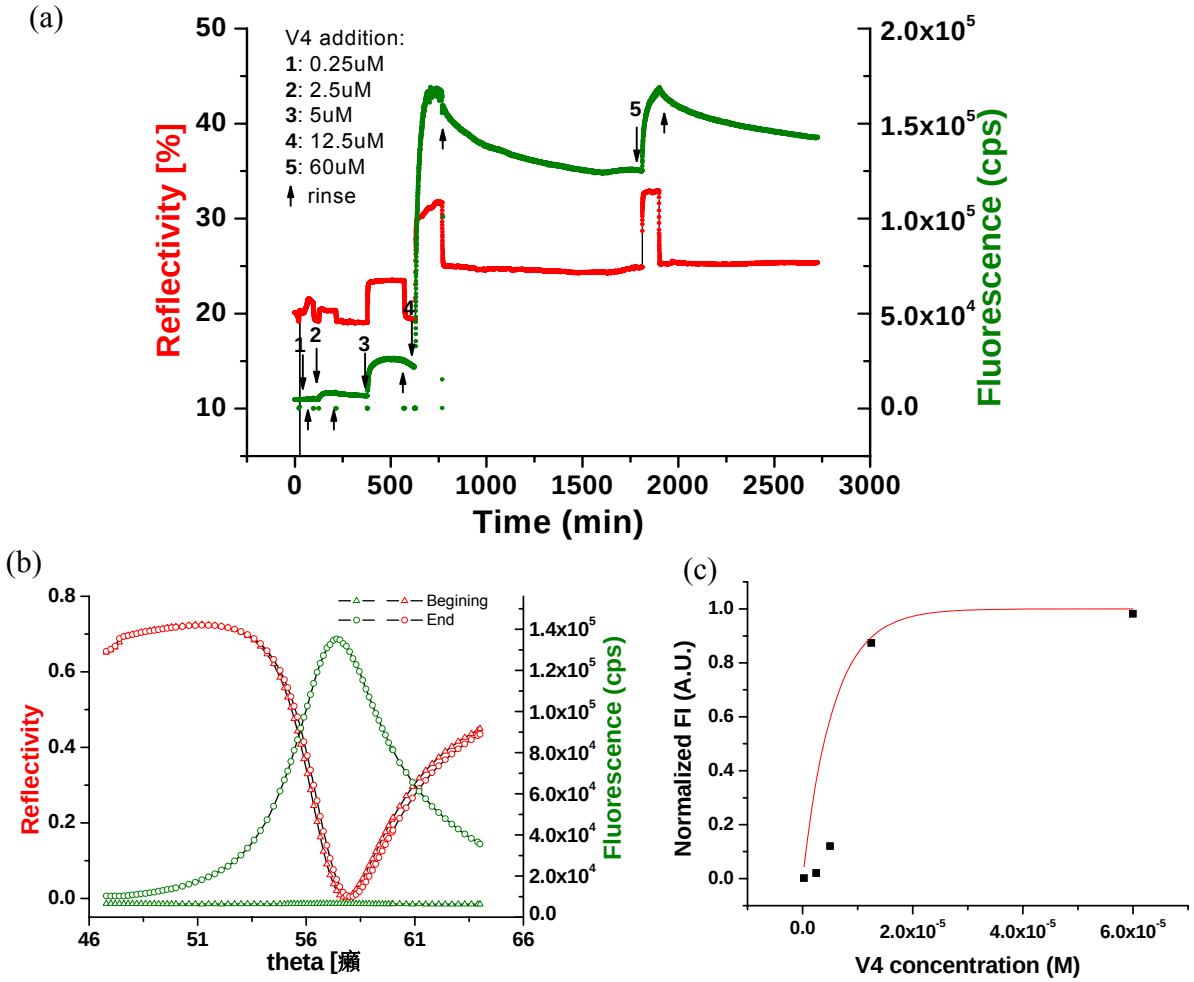

Figure 7.6: (a) Kinetic SPFS curve taken at a fixed angle of observation during step-wise additions of V4 at different concentration; (b) the angular scans at the beginning and the end of the kinetics; (c) Normalized FI versus concentration for the adsorption of V4 to lipid A-embedded tBLM. The solid line is fit of the data to Langmuir isotherm.

The affinity constants K_A of the peptide V4-S0387 on lipid A were also determined by recording the equilibrium binding to the probe surface at different bulk target concentrations c_0. Figure 7.6a shows the corresponding SPR and SPFS kinetic responses, respectively, as a function of time recorded after subsequent injection of different concentrations of V4-S0387 (0.25 µM, 2.5 µM, 5 µM, 12.5 µM, 60 µM, respectively) on the DPhyPC/lipid A mixed tBLM sensor surface. The SPR and SPFS optical response was measured by tuning the laser incident to an angle slightly smaller than the SPR minimum angle (at reflectivity of 20%) and monitoring the reflectivity and fluorescence intensity change.

The normalized equilibrium response of fluorescence intensity was plotted against the corresponding concentrations c_0, as shown in Figure 7.6b. It clearly shows a concentration-dependent increase in response units upon peptide binding. A non-linear steady-state fit, based on Langmuir adsorption model, allows for the determination of K_A, shown as the red fitting curve. The affinity constant of V4-S0387 to lipid A thus obtained is 1.8×10^5 M^{-1}, in good agreement with the affinity constants obtained from the fluorescence correlation spectroscopy (FCS) study.[196]

(a)

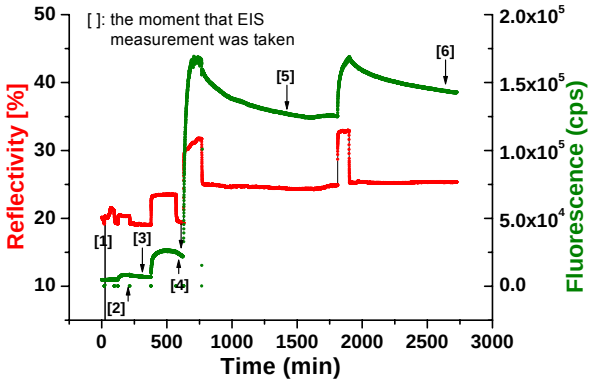

(b)

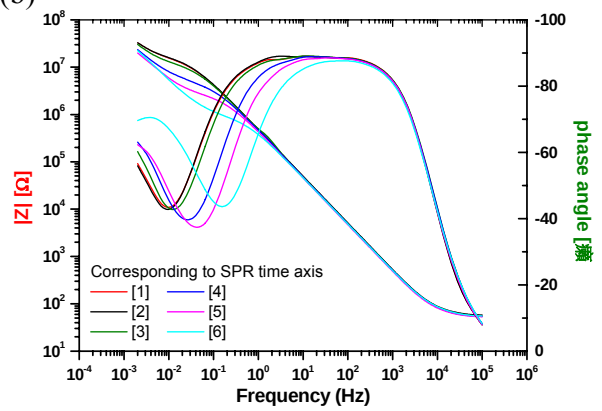

(c)

Code	R [MΩ cm2]	R error	C [μF/cm2]	C error
[1]	6.9	3.2%	0.72	1.9%
[2]	6.7	3.5%	0.72	1.9%
[3]	5.2	3.4%	0.72	2.1%
[4]	2.5	3.8%	0.72	2.2%
[5]	0.91	4.2%	0.74	2.9%
[6]	0.46	4.5%	0.74	3.1%

Figure 7.7: (a) Labeled moments on kinetic SPFS curve where EIS measurements were displayed in (b); (b) Selected EIS Bode plots corresponding to particular moments; (c) Table of calculated membrane resistance and capacitance from fitted EIS data.

Simultaneously, the step-wise titration process was also followed by EIS measurements (EIS and SPR combination, refer to Chapter 3). The Bode plots at selected moments are presented in Figure 7.7. The corresponding fitting results of the membrane electrical parameters to the equivalent circuit are also given in the table of 7.7c. At low peptide

concentration and after rinsing and equilibrium, the measured membrane resistance showed little change. At a peptide concentraiton of 5 µM, the resistance value decreased with increasing peptide concentration, which indicated that at this concentration, V4 peptide began to induce membrane leakage. At highest V4-S0387 concentration of 60 µM, the resistance even dropped down to 0.4 MΩcm^2.

V4 and V4-S0387 displayed different characteristics if one compares Figure 7.5 and 7.7. V4's addition to DPhyPC/lipid A tBLMs reduced membrane resistance down even lower than V4-S0387 did. It is believed that the dye S0387 labelling may slightly influence the V4 molecule's ability to disrupt the lipid A containing membrane.

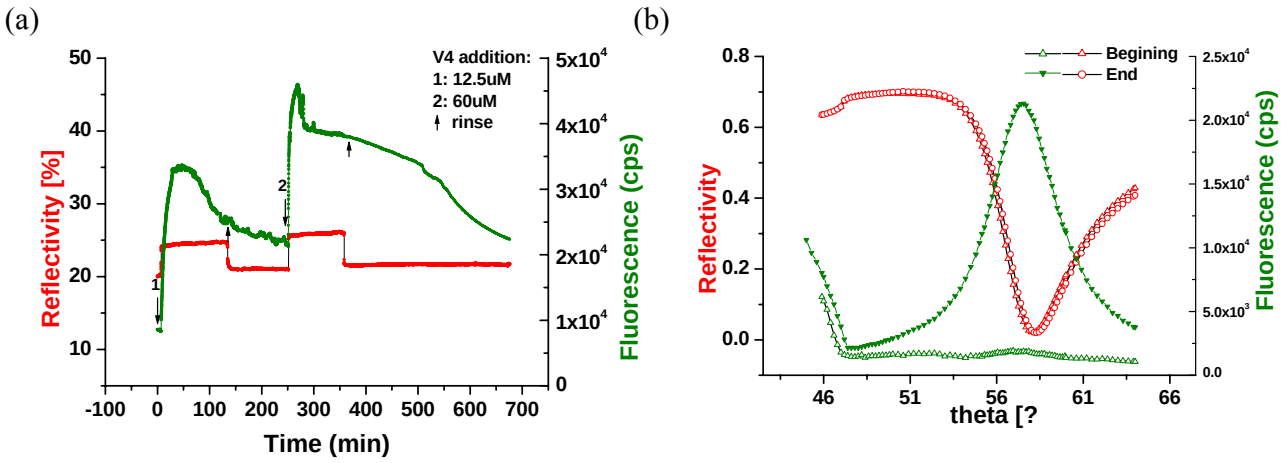

Figure 7.8: (a) Kinetic SPFS curve taken at a fixed angle of observation during step-wise additions of V4-S0387 at different concentration on DPhyPC tBLM; (b) the angular scans at the beginning and the end of the kinetics.

As a comparison, the combination of SPFS and EIS was also applied to investigate the interaction between V4-S0387 and DPhyPC tBLMs. The SPFS titration kinetics and angular scans are presented in Figure 7.8. Under the same experimental conditions, V4-S0387 showed much lower affinity to DPhyPC tBLMs than to DPhyPC/lipid A mixed tBLMs. At the same time, the EIS impedance spectra showed only slight change of membrane resistance during the whole process (data not shown).

7.3.4 V4 binding to DPhyPC/LPS mixed tBLMs

In a final step, we investigated the interaction of V4 with a membrane containing LPS (Figure 7.9). Again, a decrease in membrane resistance can be observed with increasing incubation time. However, the effect is smaller than in case of the Lipid A containing membrane, i.e. the resistance decreases from about 6 MΩcm^2 to about 1 MΩcm^2. The capsule

polysaccharide is believed to function as a cushion region and limit the interaction of the peptides with their membrane targets.

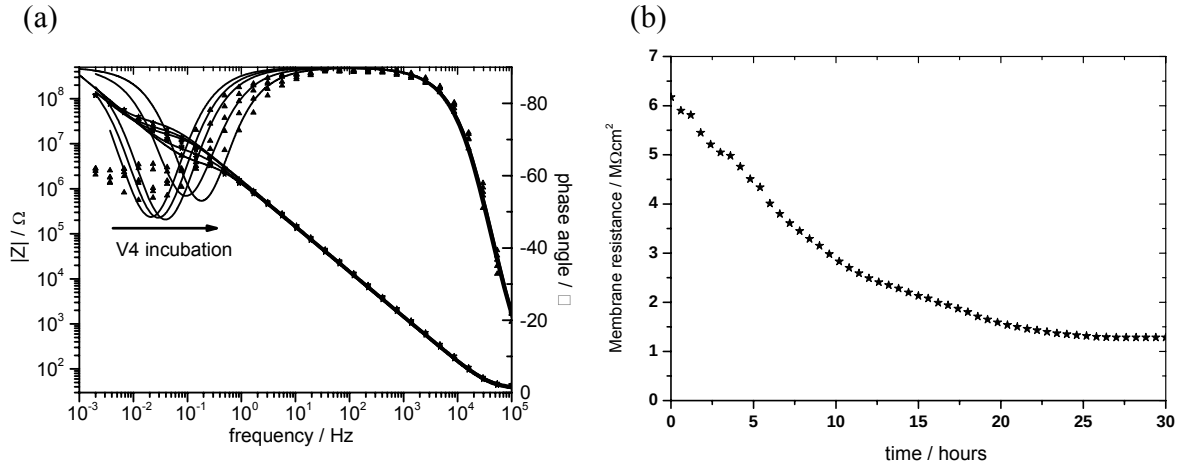

Figure 7.9: Incorporation of V4 in an LPS-containing tBLM. A) Selected Bode plots showing the successive incorporation. Solid lines represent fits to a simple equivalent circuit. B) Decrease in the fitted membrane resistance as a function of time.

7.4 *Conclusion*

We have demonstrated that by incorporating lipopolysaccharides into tBLMs, antigen-antibody assay can be conducted using SPFS with high sensitivity. The effects of antimicrobial peptide V4 on different membrane components have also been electrochemically investigated based on the tBLM platform. Membrane surface charge density has been tuned by mixing PC/PG terminated phosphor lipids at different ratios and the importance of electrostatics in the interaction between V4 and membranes has been emphasized.

Lipid A was incorporated into tBLMs as a more real mimic of bacterial outer membranes. The strong disruptive effect of V4 on the lipid A-containing membrane coincides with the high specificity in killing bacteria.

8. Summary

The development and characterization of biomolecule sensor formats based on the optical technique Surface Plasmon Resonance (SPR) Spectroscopy and electrochemical methods were investigated.

The study can be divided into two parts of different scope.

In the first part new novel detection schemes for labeled targets were developed on the basis of the investigations in Surface-plamon Field Enhanced Spectroscopy (SPFS). The first one is SPR fluorescence imaging formats, Surface-plamon Field Enhanced Fluorescence Microscopy (SPFM). Patterned self assembled monolayers (SAMs) were prepared and used to direct the spatial distribution of biomolecules immobilized on surfaces. Here the patterned monolayers would serve as molecular templates to secure different biomolecules to known locations on a surface. The binding processed of labeled target biomolecules from solution to sensor surface were visually and kinetically recorded by the fluorescence microscope, in which fluorescence was excited by the evanescent field of propagating plasmon surface polaritons. The second format which also originates from SPFS technique, Surface-plamon Field Enhanced Fluorescence Spectrometry (SPFSm), concerns the coupling of a fluorometry to normal SPR setup. A spectrograph mounted in place of photomultiplier or microscope can provide the information of fluorescence spectrum as well as fluorescence intensity. This study also firstly demonstrated the analytical combination of surface plasmon enhanced fluorescence detection with analyte tagged by semiconducting nano- crystals (QDs).

Electrochemically addressable fabrication of DNA biosensor arrays in aqueous environment was also developed. An electrochemical method was introduced for the directed *in-situ* assembly of various specific oligonucleotide catcher probes onto different sensing elements of a multi-electrode array in the aqueous environment of a flow cell. Surface plasmon microscopy (SPM) is utilized for the on-line recording of the various functionalization steps. Hybridization reactions between targets from solution to the different surface-bound complementary probes are monitored by surface-plasmon field-enhanced fluorescence microscopy (SPFM) using targets that are either labeled with organic dyes or with semiconducting quantum dots for color-multiplexing. This study provides a new approach for the fabrication of (small) DNA arrays and the recording and quantitative evaluation of parallel hybridization reactions.

In the second part of this work, the ideas of combining the SP optical and electrochemical characterization were extended to tethered bilayer lipid membrane (tBLM) format. Tethered bilayer lipid membranes provide a versatile model platform for the study of many membrane related processes.

The thiolipids were firstly self-assembled on ultraflat gold substrates. Fusion of the monolayers with small unilamellar vesicles (SUVs) formed the distal layer and the membranes thus obtained have the sealing properties comparable to those of natural membranes. The fusion could be monitored optically by SPR as an increase in reflectivity (thickness) upon formation of the outer leaflet of the bilayer. With EIS, a drop in capacitance and a steady increase in resistance could be observed leading to a tightly sealing membrane with low leakage currents.

The assembly of tBLMs and the subsequent incorporation of membrane proteins were investigated with respect to their potential use as a biosensing system. In the case of *valinomycin* the potassium transport mediated by the ion carrier could be shown by a decrease in resistance upon increasing potassium concentration. Potential mediation of membrane pores could be shown for the ion channel forming peptide alamethicin (Alm). It was shown that at high positive dc bias (*cis* negative) Alm channels stay at relatively low conductance levels and show higher permeability to potassium than to tetramethylammonium. The addition of inhibitor amiloride can partially block the Alm channels and results in increase of membrane resistance.

tBLMs are robust and versatile model membrane architectures that can mimic certain properties of biological membranes. tBLMs with incorporated lipopolysaccharide (LPS) and lipid A mimicking bacteria membranes were used to probe the interactions of antibodies against LPS and to investigate the binding and incorporation of the small antimicrobial peptide V4. The influence of membrane composition and charge on the behavior of V4 was also probed. This study displays the possibility of using tBLM platform to record and valuate the efficiency or potency of numerous synthesized antimicrobial peptides as potential drug candidates.

9. Supplementary

9.1 *Abbreviations*

Alm	alamethicin
AC	alternating current
AFM	atomic force microscopy
ATR	attenuated total reflection
BLMs	black lipid membranes
bp	base pairs
BSA	bovine serum albumin
CCD	charge coupled device
cps	counts per second
Cy	cyanine dye
Da	dalton (g/mol)
DLS	dynamic light scattering
DMSO	dimethyl sulfoxide $(CH_3)_2SO$
DNA	deoxyribonucleic acid
DPhyPC	1,2-diphytanoyl-*sn*-glycero-3-phosphocholine
DPhyPG	1,2-Diphytanoyl-sn-Glycero-3-[Phospho-rac-(1-glycerol)]
DPTL	2,3-di-O-phytanyl-sn-glycerol-1-tetraethylen glycol-DL-α-lipoic acid ester
E	potential
EC	electrochemistry
EDC	carbodiimide hydrochloride
EG	ethylene glycol
EIS	electrochemical impedance spectroscopy
FCS	fluorescence correlation spectroscopy
FI	fluorescence intensity
Fig.	figure
FRA	frequency response analyzer
GUV	giant unilamellar vesicles
HeNe	Helium-Heon
i	current response
IgG	immunoglobulin
LA	lipid A
LASFN9	high refractive index glass from Schott
LB	Langmuir-Blodgett

LPS	lipopolysaccharide
LUV	large unilamellar vesicles
MLVs	mutilamellar vesicles
MM	(base pair) mismatch
Mw	molecular weight
mV	millivolt, 10^{-3} V
nm	nanometer, 10^{-9} m
n	refractive index
NHS	N-hydroxy succinimide
NSB	non-specific binding
pABs	polyclonal antibodies
PBS	phosphate buffered saline (buffer)
PEG	polyethylene glycol
PMT	photo multiplier tube
QD	quantum dot
R	resistance
SA	streptavidin
SAM	self-assembed monolayer
sBLM	supported bilayer lipid membranes
SP	surface plasmon
SPFM	surface plasmon fluorescence microscopy
SPFS	surface plasmon fluorescence spectroscopy
SPFSm	surface plasmon fluorescence spectrometry
SPM	surface plasmon microscopy
SPR	surface plasmon resonance
SUV	small unilamellar vesicles
tBLM	tethered bilayer lipid membrane
TE	transversal electric (s-) polarization
TIR	total internal reflection
TM	transversal magnetic (p-) polarization
TMAC	tetramethyl ammonium chloride
TSG	template stripped gold
UV	ultraviolet
Z	impedance

9.2 *List of figures*

9.3 *Bibliography*

1. Caruso, A. F. C. a. F., Biosensors: recent advances *Reports on Progress in Physics* **1997,** 60, (11), 1397-1445.
2. Liebermann, T.; Knoll, W., Surface-plasmon field-enhanced fluorescence spectroscopy. *Colloids and Surfaces A: Physicochemical and Engineering Aspects* **2000,** 171, (1-3), 115-130.
3. Neumann, T.; Johansson, M. L.; Kambhampati, D.; Knoll, W., Surface-plasmon fluorescence spectroscopy. *Advanced Functional Materials* **2002,** 12, (9), 575-586.
4. Kwon, S. H.; Hong, B. J.; Park, H. Y.; Knoll, W.; Park, J. W., DNA-DNA interaction on dendron-functionalized sol-gel silica films followed with surface plasmon fluorescence spectroscopy. *Journal of Colloid and Interface Science* **2007,** 308, (2), 325-331.
5. Buckle, M.; Williams, R. M.; Negroni, M.; Buc, H., Real time measurements of elongation by a reverse transcriptase using surface plasmon resonance. *Proceedings of the National Academy of Sciences* **1996,** 93, (2), 889-894.
6. Ligler, F. S.; Rabbany, S. Y., *Synthetic microstructures in biological research* Plenum Press, New York: 1992; p 67-75.
7. Turner;, A. P.; Karube;, I.; Wilson, G. S., *Biosensors: Fundamentals and applications* Oxford University Press, New York: 1987.
8. Lowe, C. R., An introduction to the concepts and technology of biosensors. *Biosensors* **1985,** 1, (1), 3-16.
9. Buerk, D. G., *Biosensors*. Technomic Publishing AG, Lancaster, USA: 1992.
10. Hall, E. A. H., *Biosensors*. Springer, Heidelberg: 1990.
11. Raether, H., *Surface Plasmon on Smooth and Rough Surfaces and on Gratings* Springer, Berlin: 1988.
12. Levy, C. D. P.; Cocolios, T. E.; Behr, J. A.; Jayamanna, K.; Minamisono, K.; Pearson, M. R., Feasibility study of in-beam polarization of fluorine. *Nuclear Instruments and Methods in Physics Research Section A: Accelerators, Spectrometers, Detectors and Associated Equipment* **2007,** 580, (3), 1571-1577.
13. Mykytczuk, N. C. S.; Trevors, J. T.; Leduc, L. G.; Ferroni, G. D., Fluorescence polarization in studies of bacterial cytoplasmic membrane fluidity under environmental stress. *Progress in Biophysics and Molecular Biology* **2007,** 95, (1-3), 60-82.
14. Su, C.-C.; Nikaido, H.; Yu, E. W., Ligand-transporter interaction in the AcrB multidrug efflux pump determined by fluorescence polarization assay. *FEBS Letters* **2007,** 581, (25), 4972-4976.
15. Tomin, V. I.; Oncul, S.; Smolarczyk, G.; Demchenko, A. P., Dynamic quenching as a simple test for the mechanism of excited-state reaction. *Chemical Physics* **2007,** 342, (1-3), 126-134.
16. Hidalgo, J.; Sanchez-Coronilla, A.; Munoz, M. A.; Carmona, C.; Balon, M., Fluorescence quenching of betacarboline (9H-pyrido[3,4-b]indole) induced by intermolecular hydrogen bonding with pyridines. *Journal of Luminescence* **2007,** 127, (2), 671-677.
17. Ramanavicius, A.; Kurilcik, N.; Jursenas, S.; Finkelsteinas, A.; Ramanaviciene, A., Conducting polymer based fluorescence quenching as a new approach to increase the selectivity of immunosensors. *Biosensors and Bioelectronics* **2007,** 23, (4), 499-505.
18. Kumar, S.; Singh, P.; Kaur, S., A Cu2+ protein cavity mimicking fluorescent chemosensor for selective Cu2+ recognition: tuning of fluorescence quenching to enhancement through spatial placement of anthracene unit. *Tetrahedron* **2007,** 63, (47), 11724-11732.

19. Uemura, T.; Furumoto, M.; Nakano, T.; Akai-Kasaya, M.; Saito, A.; Aono, M.; Kuwahara, Y., Local-plasmon-enhanced up-conversion fluorescence from copper phthalocyanine. *Chemical Physics Letters* **2007,** 448, (4-6), 232-236.
20. Kiraz, A.; Doganay, S.; Kurt, A.; Demirel, A. L., Enhanced energy transfer in single glycerol/water microdroplets standing on a superhydrophobic surface. *Chemical Physics Letters* **2007,** 444, (1-3), 181-185.
21. Ma, Q.; Su, X.-G.; Wang, X.-Y.; Wan, Y.; Wang, C.-L.; Yang, B.; Jin, Q.-H., Fluorescence resonance energy transfer in doubly-quantum dot labeled IgG system. *Talanta* **2005,** 67, (5), 1029-1034.
22. Graham, C. R.; Leslie, D.; Squirrell, D. J., Gene probe assays on a fibre-optic evanescent wave biosensor. *Biosensors and Bioelectronics* **1992,** 7, (7), 487-493.
23. Piunno, P. A. E.; Krull, U. J.; Hudson, R. H. E.; Damha, M. J.; Cohen, H., Fiber-Optic DNA Sensor for Fluorometric Nucleic Acid Determination. *Anal. Chem.* **1995,** 67, (15), 2635-2643.
24. Abel, A. P.; Weller, M. G.; Duveneck, G. L.; Ehrat, M.; Widmer, H. M., Fiber-Optic Evanescent Wave Biosensor for the Detection of Oligonucleotides. *Anal. Chem.* **1996,** 68, (17), 2905-2912.
25. Liebermann, T.; Knoll, W.; Sluka, P.; Herrmann, R., Complement hybridization from solution to surface-attached probe-oligonucleotides observed by surface-plasmon-field-enhanced fluorescence spectroscopy. *Colloids and Surfaces A: Physicochemical and Engineering Aspects* **2000,** 169, (1-3), 337-350.
26. Krupka, S. S.; Wiltschi, B.; Reuning, U.; Holscher, K.; Hara, M.; Sinner, E.-K., In vivo detection of membrane protein expression using surface plasmon enhanced fluorescence spectroscopy (SPFS). *Biosensors and Bioelectronics* **2006,** 22, (2), 260-267.
27. Ekgasit, S.; Yu, F.; Knoll, W., Fluorescence intensity in surface-plasmon field-enhanced fluorescence spectroscopy. *Sensors and Actuators B: Chemical* **2005,** 104, (2), 294-301.
28. Matveeva, E.; Gryczynski, Z.; Malicka, J.; Gryczynski, I.; Lakowicz, J. R., Metal-enhanced fluorescence immunoassays using total internal reflection and silver island-coated surfaces. *Analytical Biochemistry* **2004,** 334, (2), 303-311.
29. Sinner, E.-K.; Reuning, U.; Kok, F. N.; Sacca, B.; Moroder, L.; Knoll, W.; Oesterhelt, D., Incorporation of integrins into artificial planar lipid membranes: characterization by plasmon-enhanced fluorescence spectroscopy. *Analytical Biochemistry* **2004,** 333, (2), 216-224.
30. Knoll, W.; Park, H.; Sinner, E.-K.; Yao, D.; Yu, F., Supramolecular interfacial architectures for optical biosensing with surface plasmons. *Surface Science* **2004,** 570, (1-2), 30-42.
31. Yeh, P., *Optical Waves in Layered Media* John Wiley & Sons, New York: 1988.
32. Agranovich, V. M., *Surface polaritonos*. North Hollan, Amsterdam: 1982.
33. Rothenhausler, B.; Knoll, W., On the influence of the propagation length of plasmon surface polaritons in the visible energy range for the optical characterization of heterogeneous thin films. *Surface Science Letters* **1987,** 191, (3), A533-A534.
34. Knoll, W., Interfaces and thin films as seen by bound electromagnetic waves. *Annual Review of Physical Chemistry* **1998,** 49, 569-638.
35. Valeur, B.; Querner, J.; Wolff, T., *Molecular Fluorescence. Principles and Applications*
Wiley-VCH: 2001.
36. Lakowicz, J. R., *Principles of fluorescence spectroscopy*. 1 ed.; Plenum Press, New York: 1983.

37. MacDonald, R. I., Characteristics of self-quenching of the fluorescence of lipid-conjugated rhodamine in membranes. *J. Biol. Chem.* **1990,** 265, (23), 13533-13539.
38. Tyagi, S.; Kramer, F. R., Molecular Beacons: Probes that Fluoresce upon Hybridization. *Nat Biotech* **1996,** 14, (3), 303-308.
39. Steinem, C.; Janshoff, A.; Ulrich, W.-P.; Sieber, M.; Galla, H.-J., Impedance analysis of supported lipid bilayer membranes: a scrutiny of different preparation techniques. *Biochimica et Biophysica Acta (BBA) - Biomembranes* **1996,** 1279, (2), 169-180.
40. Sackmann, E., Supported Membranes: Scientific and Practical Applications. *Science* **1996,** 271, (5245), 43-48.
41. Cornell, B. A.; BraachMaksvytis, V. L. B.; King, L. G.; Osman, P. D. J.; Raguse, B.; Wieczorek, L.; Pace, R. J., A biosensor that uses ion-channel switches. *Nature* **1997,** 387, (6633), 580-583.
42. Stelzle, M.; Weissmueller, G.; Sackmann, E., On the application of supported bilayers as receptive layers for biosensors with electrical detection. *J. Phys. Chem.* **1993,** 97, (12), 2974-2981.
43. Hickel, W.; Knoll, W., Surface plasmon microscopy of lipid layers. *Thin Solid Films* **1990,** 187, (2), 349-356.
44. Rothenhausler, B.; Knoll, W., SurfaceÂ–plasmon microscopy. *Nature* **1988,** 332, (6165), 615-617.
45. Corn, R. M.; Smith, E. A.; Wegner, G. J.; Goodrich, T. T.; Lee, H. J., SPR imaging measurements of DNA, peptide and protein microarrays. *Abstracts of Papers of the American Chemical Society* **2002,** 224, U151-U151.
46. Li, Y.; Lee, H. J.; Corn, R. M., Detection of protein biomarkers using RNA aptamer microarrays and enzymatically amplified surface plasmon resonance imaging. *Analytical Chemistry* **2007,** 79, (3), 1082-1088.
47. Lee, H. J.; Li, Y.; Wark, A. W.; Corn, R. M., Enzymatically Amplified Surface Plasmon Resonance Imaging Detection of DNA by Exonuclease III Digestion of DNA Microarrays. *Anal. Chem.* **2005,** 77, (16), 5096-5100.
48. Fang, S.; Lee, H. J.; Wark, A. W.; Kim, H. M.; Corn, R. M., Determination of ribonuclease H surface enzyme kinetics by surface plasmon resonance imaging and surface plasmon fluorescence spectroscopy. *Analytical Chemistry* **2005,** 77, (20), 6528-6534.
49. Hickel, W.; Kamp, D.; Knoll, W., Surface-plasmon microscopy. *Nature* **1989,** 339, (6221), 186-186.
50. Porter, M. D.; Bright, T. B.; Allara, D. L.; Chidsey, C. E. D., Spontaneously organized molecular assemblies. 4. Structural characterization of n-alkyl thiol monolayers on gold by optical ellipsometry, infrared spectroscopy, and electrochemistry. *J. Am. Chem. Soc.* **1987,** 109, (12), 3559-3568.
51. Whitesides, G. M.; Laibinis, P. E., Wet chemical approaches to the characterization of organic surfaces: self-assembled monolayers, wetting, and the physical-organic chemistry of the solid-liquid interface. *Langmuir* **1990,** 6, (1), 87-96.
52. Bain, C. D.; Troughton, E. B.; Tao, Y. T.; Evall, J.; Whitesides, G. M.; Nuzzo, R. G., Formation of monolayer films by the spontaneous assembly of organic thiols from solution onto gold. *J. Am. Chem. Soc.* **1989,** 111, (1), 321-335.
53. Nuzzo, R. G.; Dubois, L. H.; Allara, D. L., Fundamental studies of microscopic wetting on organic surfaces. 1. Formation and structural characterization of a self-consistent series of polyfunctional organic monolayers. *J. Am. Chem. Soc.* **1990,** 112, (2), 558-569.
54. Lipshutz, R. J.; Fodor, S. P. A.; Gingeras, T. R.; Lockhart, D. J., High density synthetic oligonucleotide arrays. *Nature Genetics* **1999,** 21, 20-24.

55. Lockhart, D. J.; Winzeler, E. A., Genomics, gene expression and DNA arrays. *Nature* **2000,** 405, (6788), 827-836.
56. Nakatani, K.; Sando, S.; Saito, I., Scanning of guanine-guanine mismatches in DNA by synthetic ligands using surface plasmon resonance. *Nature Biotechnology* **2001,** 19, (1), 51-55.
57. Muhlberger, R.; Robelek, R.; Eisenreich, W.; Ettenhuber, C.; Sinner, E. K.; Kessler, H.; Bacher, A.; Richter, G., RNA DNA discrimination by the antitermination protein NusB. *Journal of Molecular Biology* **2003,** 327, (5), 973-983.
58. Casper, D.; Bukhtiyarova, M.; Springman, E. B., A Biacore biosensor method for detailed kinetic binding analysis of small molecule inhibitors of p38 alpha mitogen-activated protein kinase. *Analytical Biochemistry* **2004,** 325, (1), 126-136.
59. Schutt, M.; Krupka, S. S.; Milbradt, A. G.; Deindl, S.; Sinner, E. K.; Oesterhelt, D.; Renner, C.; Moroder, L., Photocontrol of cell adhesion processes: Model studies with cyclic azobenzene-RGD peptides. *Chemistry & Biology* **2003,** 10, (6), 487-490.
60. Kambhampati, D.; Nielsen, P. E.; Knoll, W., Investigating the kinetics of DNA-DNA and PNA-DNA interactions using surface plasmon resonance-enhanced fluorescence spectroscopy. *Biosensors & Bioelectronics* **2001,** 16, (9-12), 1109-1118.
61. Chan, W. C. W.; Maxwell, D. J.; Gao, X. H.; Bailey, R. E.; Han, M. Y.; Nie, S. M., Luminescent quantum dots for multiplexed biological detection and imaging. *Current Opinion in Biotechnology* **2002,** 13, (1), 40-46.
62. Bruchez, M.; Moronne, M.; Gin, P.; Weiss, S.; Alivisatos, A. P., Semiconductor nanocrystals as fluorescent biological labels. *Science* **1998,** 281, (5385), 2013-2016.
63. Schena, M.; Heller, R. A.; Theriault, T. P.; Konrad, K.; Lachenmeier, E.; Davis, R. W., Microarrays: biotechnology's discovery platform for functional genomics. *Trends in Biotechnology* **1998,** 16, (7), 301-306.
64. Meltzer, S.; Mandler, D., Microwriting of Gold Patterns with the Scanning Electrochemical Microscope. *Journal of the Electrochemical Society* **1995,** 142, (6), L82-L84.
65. Lopez, G. P.; Biebuyck, H. A.; Harter, R.; Kumar, A.; Whitesides, G. M., Fabrication and Imaging of 2-Dimensional Patterns of Proteins Adsorbed on Self-Assembled Monolayers by Scanning Electron-Microscopy. *Journal of the American Chemical Society* **1993,** 115, (23), 10774-10781.
66. Lopez, G. P.; Biebuyck, H. A.; Frisbie, C. D.; Whitesides, G. M., Imaging of Features on Surfaces by Condensation Figures. *Science* **1993,** 260, (5108), 647-649.
67. Kumar, A.; Whitesides, G. M., Patterned Condensation Figures as Optical Diffraction Gratings. *Science* **1994,** 263, (5143), 60-62.
68. Abbott, N. L.; Folkers, J. P.; Whitesides, G. M., Manipulation of the Wettability of Surfaces on the 0.1-Micrometer to 1-Micrometer Scale through Micromachining and Molecular Self-Assembly. *Science* **1992,** 257, (5075), 1380-1382.
69. Walczak, M. M.; Popenoe, D. D.; Deinhammer, R. S.; Lamp, B. D.; Chung, C. K.; Porter, M. D., Reductive Desorption of Alkanethiolate Monolayers at Gold - a Measure of Surface Coverage. *Langmuir* **1991,** 7, (11), 2687-2693.
70. Widrig, C. A.; Chung, C.; Porter, M. D., The Electrochemical Desorption of N-Alkanethiol Monolayers from Polycrystalline Au and Ag Electrodes. *Journal of Electroanalytical Chemistry* **1991,** 310, (1-2), 335-359.
71. Imabayashi, S.; Hobara, D.; Kakiuchi, T.; Knoll, W., Selective replacement of adsorbed alkanethiols in phase-separated binary self-assembled monolayers by electrochemical partial desorption. *Langmuir* **1997,** 13, (17), 4502-4504.

72. Imabayashi, S.; Iida, M.; Hobara, D.; Feng, Z. Q.; Niki, K.; Kakiuchi, T., Reductive desorption of carboxylic-acid-terminated alkanethiol monolayers from Au(111) surfaces. *Journal of Electroanalytical Chemistry* **1997,** 428, (1-2), 33-38.
73. Ross, C. B.; Sun, L.; Crooks, R. M., Scanning Probe Lithography .1. Scanning Tunneling Microscope Induced Lithography of Self-Assembled N-Alkanethiol Monolayer Resists. *Langmuir* **1993,** 9, (3), 632-636.
74. Tender, L. M.; Worley, R. L.; Fan, H. Y.; Lopez, G. P., Electrochemical patterning of self-assembled monolayers onto microscopic arrays of gold electrodes fabricated by laser ablation. *Langmuir* **1996,** 12, (23), 5515-5518.
75. Boon, E. M.; Jackson, N. M.; Wightman, M. D.; Kelley, S. O.; Hill, M. G.; Barton, J. K., Intercalative stacking: A critical feature of DNA charge-transport electrochemistry. *Journal of Physical Chemistry B* **2003,** 107, (42), 11805-11812.
76. Boon, E. M.; Ceres, D. M.; Drummond, T. G.; Hill, M. G.; Barton, J. K., Mutation detection by electrocatalysis at DNA-modified electrodes. *Nature Biotechnology* **2000,** 18, (10), 1096-1100.
77. Drummond, T. G.; Hill, M. G.; Barton, J. K., Electron transfer rates in DNA films as a function of tether length. *Journal of the American Chemical Society* **2004,** 126, (46), 15010-15011.
78. Drummond, T. G.; Hill, M. G.; Barton, J. K., Electrochemical DNA sensors. *Nature Biotechnology* **2003,** 21, (10), 1192-1199.
79. Palecek, E.; Fojta, M., Detecting DNA hybridization and damage. *Analytical Chemistry* **2001,** 73, (3), 74A-83A.
80. Knoll, W.; Zizlsperger, M.; Liebermann, T.; Arnold, S.; Badia, A.; Liley, M.; Piscevic, D.; Schmitt, F. J.; Spinke, J., Streptavidin arrays as supramolecular architectures in surface-plasmon optical sensor formats. *Colloids and Surfaces a-Physicochemical and Engineering Aspects* **2000,** 161, (1), 115-137.
81. Robelek, R.; Niu, L. F.; Schmid, E. L.; Knoll, W., Multiplexed hybridization detection of quantum dot-conjugated DNA sequences using surface plasmon enhanced fluorescence microscopy and spectrometry. *Analytical Chemistry* **2004,** 76, (20), 6160-6165.
82. Badia, A.; Arnold, S.; Scheumann, V.; Zizlsperger, M.; Mack, J.; Jung, G.; Knoll, W., Probing the electrochemical deposition and/or desorption of self-assembled and electropolymerizable organic thin films by surface plasmon spectroscopy and atomic force microscopy. *Sensors and Actuators B-Chemical* **1999,** 54, (1-2), 145-165.
83. Lipowsky;, R.; Sackmann, E., *Structure and dynamics of membranes: From cells to vesicles* Elsevier, Amsterdam: 1995

84. Gennis, R. B., *Biomembranes: Molecular structure and function*. Springer-Verlab, New York: 1989.
85. Mathews, C. K.; van Holde, K. E., *Biocheistry*. Benjamin/Cummings, Menlo Park, CA: 1996.
86. Darnell, J. E.; Lodish, H.; Baltimore, D., *Molecualr cell biology*. Scientific American Books, New York: 1986.
87. Singer, S. J.; Nicolson, G. L., Fluid Mosaic Model of Structure of Cell-Membranes. *Science* **1972,** 175, (4023), 720-&.
88. Prasad, R., *Manual on membrane lipids*. Springer-Verlag, Berlin: 1996.
89. Rentschler, M.; Fromherz, P., Membrane-transistor cable. *Langmuir* **1998,** 14, (2), 547-551.

90. Hauser, H.; Pascher, I.; Pearson, R. H.; Sundell, S., Preferred Conformation and Molecular Packing of Phosphatidylethanolamine and Phosphatidylcholine. *Biochimica Et Biophysica Acta* **1981,** 650, (1), 21-51.
91. Tien, H. T.; Ottova-Laitmannova, A., *The lipid bilayer concept: Experimental realization and current applications, Planar lipid bilayers (BLMs) and their application*. Elsevier, Amsterdam: 2003.
92. Evans, D. F.; Wennerström, H., *The colloid domain*. John Wiley & Sons, Chichester: 1999.
93. Seantier, B.; Breffa, C.; Felix, O.; Decher, G., In situ investigations of the formation of mixed supported lipid bilayers close to the phase transition temperature. *Nano Letters* **2004,** 4, (1), 5-10.
94. Neumcke, B.; Lauger, P., Nonlinear Electrical Effects in Lipid Bilayer Membranes .2. Integration of Generalized Nernst-Planck Equations. *Biophysical Journal* **1969,** 9, (9), 1160-&.
95. Coster, H. G. L., Self-assembly, stability and the electrical characteristics of cell membranes. *Australian Journal of Physics* **1999,** 52, (1), 117-140.
96. Coster, H. G. L.; Simons, R., Energy of Formation of Bimolecular Lipid Membranes. *Biochimica Et Biophysica Acta* **1968,** 163, (2), 234-&.
97. Bramhall, J., Electrostatic Forces Control the Penetration of Membranes by Charged Solutes. *Biochimica Et Biophysica Acta* **1984,** 778, (3), 393-399.
98. Deamer, D. W.; Bramhall, J., Permeability of Lipid Bilayers to Water and Ionic Solutes. *Chemistry and Physics of Lipids* **1986,** 40, (2-4), 167-188.
99. Flewelling, R. F.; Hubbell, W. L., Hydrophobic Ion Interactions with Membranes - Thermodynamic Analysis of Tetraphenylphosphonium Binding to Vesicles. *Biophysical Journal* **1986,** 49, (2), 531-540.
100. Flewelling, R. F.; Hubbell, W. L., The Membrane Dipole Potential in a Total Membrane-Potential Model - Applications to Hydrophobic Ion Interactions with Membranes. *Biophysical Journal* **1986,** 49, (2), 541-552.
101. Smaby, J. M.; Momsen, M. M.; Brockman, H. L.; Brown, R. E., Phosphatidylcholine acyl unsaturation modulates the decrease in interfacial elasticity induced by cholesterol. *Biophysical Journal* **1997,** 73, (3), 1492-1505.
102. Needham, D.; Nunn, R. S., Elastic-Deformation and Failure of Lipid Bilayer-Membranes Containing Cholesterol. *Biophysical Journal* **1990,** 58, (4), 997-1009.
103. Papahadj.D; Jacobson, K.; Nir, S.; Isac, T., Phase-Transitions in Phospholipid Vesicles - Fluorescence Polarization and Permeability Measurements Concerning Effect of Temperature and Cholesterol. *Biochimica Et Biophysica Acta* **1973,** 311, (3), 330-348.
104. Blok, M. C.; Vandeenen, L. L. M.; Degier, J., Effect of Gel to Liquid-Crystalline Phase-Transition on Osmotic Behavior of Phosphatidylcholine Liposomes. *Biochimica Et Biophysica Acta* **1976,** 433, (1), 1-12.
105. Clerc, S.; Barenholz, Y., Loading of amphipathic weak acids into liposomes in response to transmembrane calcium acetate gradients. *Biochimica Et Biophysica Acta-Biomembranes* **1995,** 1240, (2), 257-265.
106. Ueno, M., Partition Behavior of a Nonionic Detergent, Octyl Glucoside, between Membrane and Water Phases, and Its Effect on Membrane-Permeability. *Biochemistry* **1989,** 28, (13), 5631-5634.
107. Han, S.; Lindholm-Sethson, B., Electrochemistry at ultrathin polyelectrolyte films self-assembled at planar gold electrodes. *Electrochimica Acta* **1999,** 45, (6), 845-853.
108. Plant, A. L., Supported hybrid bilayer membranes as rugged cell membrane mimics. *Langmuir* **1999,** 15, (15), 5128-5135.

109. Drexler, J.; Steinem, C., Pore-suspending lipid bilayers on porous alumina investigated by electrical impedance spectroscopy. *Journal of Physical Chemistry B* **2003,** 107, (40), 11245-11254.
110. Stelzle, M.; Weissmuller, G.; Sackmann, E., On the Application of Supported Bilayers as Receptive Layers for Biosensors with Electrical Detection. *Journal of Physical Chemistry* **1993,** 97, (12), 2974-2981.
111. Karlsson, M.; Nolkrantz, K.; Davidson, M. J.; Stromberg, A.; Ryttsen, F.; Akerman, B.; Orwar, O., Electroinjection of colloid particles and biopolymers into single unilamellar liposomes and cells for bioanalytical applications. *Analytical Chemistry* **2000,** 72, (23), 5857-5862.
112. Lasic, D. D., *Liposomes: from physics to applicatons*. Elsevier, amsterdam: 1993.
113. Hope, M. J.; Bally, M. B.; Webb, G.; Cullis, P. R., Production of Large Unilamellar Vesicles by a Rapid Extrusion Procedure - Characterization of Size Distribution, Trapped Volume and Ability to Maintain a Membrane-Potential. *Biochimica Et Biophysica Acta* **1985,** 812, (1), 55-65.
114. Szoka, F.; Papahadjopoulos, D., Procedure for Preparation of Liposomes with Large Internal Aqueous Space and High Capture by Reverse-Phase Evaporation. *Proceedings of the National Academy of Sciences of the United States of America* **1978,** 75, (9), 4194-4198.
115. Dimitrov, D. S.; Li, J.; Angelova, M.; Jain, R. K., Surface Effects in Preparation of Cell-Size Liposomes. *Febs Letters* **1984,** 176, (2), 398-400.
116. Criado, M.; Keller, B. U., A Membrane-Fusion Strategy for Single-Channel Recordings of Membranes Usually Non-Accessible to Patch-Clamppipette Electrodes. *Febs Letters* **1987,** 224, (1), 172-176.
117. Barenholz, Y.; Gibbes, D.; Litman, B. J.; Goll, J.; Thompson, T. E.; Carlson, F. D., Simple Method for Preparation of Homogeneous Phospholipid Vesicles. *Biochemistry* **1977,** 16, (12), 2806-2810.
118. Olson, F.; Hunt, C. A.; Szoka, F. C.; Vail, W. J.; Papahadjopoulos, D., Preparation of Liposomes of Defined Size Distribution by Extrusion through Polycarbonate Membranes. *Biochimica Et Biophysica Acta* **1979,** 557, (1), 9-23.
119. Macdonald, R. C.; Macdonald, R. I.; Menco, B. P. M.; Takeshita, K.; Subbarao, N. K.; Hu, L. R., Small-Volume Extrusion Apparatus for Preparation of Large, Unilamellar Vesicles. *Biochimica Et Biophysica Acta* **1991,** 1061, (2), 297-303.
120. Mueller, P.; Rudin, D. O.; Tien, H. T.; Wescott, W. C., Reconstitution of Cell Membrane Structure in Vitro and Its Transformation into an Excitable System. *Nature* **1962,** 194, (4832), 979-&.
121. Hanyu, Y.; Yamada, T.; Matsumoto, G., Simultaneous measurement of spectroscopic and physiological signals from a planar bilayer system: Detecting voltage-dependent movement of a membrane-incorporated peptide. *Biochemistry* **1998,** 37, (44), 15376-15382.
122. Ogier, S. D.; Bushby, R. J.; Cheng, Y. L.; Evans, S. D.; Evans, S. W.; Jenkins, A. T. A.; Knowles, P. F.; Miles, R. E., Suspended planar phospholipid bilayers on micromachined supports. *Langmuir* **2000,** 16, (13), 5696-5701.
123. Mueller, P.; Wescott, W. C.; Rudin, D. O.; Tien, H. T., Methods for Formation of Single Bimolecular Lipid Membranes in Aqueous Solution. *Journal of Physical Chemistry* **1963,** 67, (2), 534-&.
124. Tien, H. T.; Ottova, A. L., The lipid bilayer concept and its experimental realization: from soap bubbles, kitchen sink, to bilayer lipid membranes. *Journal of Membrane Science* **2001,** 189, (1), 83-117.
125. Coronado, R.; Latorre, R., Phospholipid-Bilayers Made from Monolayers on Patch-Clamp Pipettes. *Biophysical Journal* **1983,** 43, (2), 231-236.

126. Purrucker, O.; Hillebrandt, H.; Adlkofer, K.; Tanaka, M., Deposition of highly resistive lipid bilayer on silicon-silicon dioxide electrode and incorporation of gramicidin studied by ac impedance spectroscopy. *Electrochimica Acta* **2001,** 47, (5), 791-798.
127. Keller, C. A.; Kasemo, B., Surface specific kinetics of lipid vesicle adsorption measured with a quartz crystal microbalance. *Biophysical Journal* **1998,** 75, (3), 1397-1402.
128. Hinterdorfer, P.; Baber, G.; Tamm, L. K., Reconstituted Influenza Hemagglutinin in Supported Planar Lipid Bilayers Selectively Binds Target Lipid Vesicles and Induces Membrane-Fusion at Low Ph. *Biophysical Journal* **1994,** 66, (2), A6-A6.
129. Tien, H. T.; Salamon, Z., Formation of Self-Assembled Lipid Bilayers on Solid Substrates. *Bioelectrochemistry and Bioenergetics* **1989,** 22, (3), 211-218.
130. Chiang, K. L.; Krull, U. J.; Nikolelis, D. P., Ellipsometric determination of the structure of surface-stabilized bilayer lipid membranes on silver metal. *Analytica Chimica Acta* **1997,** 357, (1-2), 73-77.
131. Rehacek, V.; Novotny, I.; Tvarozek, V.; Mika, F.; Ziegler, W.; Ottova-Leitmannova, A.; Tien, H. T., Supported BLM microprobe with thin-film Ag/AgCI reference electrode for pH measurements. *Sensors and Materials* **1998,** 10, (4), 229-239.
132. Cullison, J. K.; Hawkridge, F. M.; Nakashima, N.; Yoshikawa, S., A Study of Cytochrome-C-Oxidase in Lipid Bilayer - Membranes on Electrode Surfaces. *Langmuir* **1994,** 10, (3), 877-882.
133. Yang, Q.; Liu, X. Y.; Hara, M.; Lundahl, P.; Miyake, J., Quantitative affinity chromatographic studies of mitochondrial cytochrome c binding to bacterial photosynthetic reaction center, reconstituted in liposome membranes and immobilized by detergent dialysis and avidin-biotin binding. *Analytical Biochemistry* **2000,** 280, (1), 94-102.
134. Rapuano, R.; CarmonaRibeiro, A. M., Physical adsorption of bilayer membranes on silica. *Journal of Colloid and Interface Science* **1997,** 193, (1), 104-111.
135. Knoll, W.; Frank, C. W.; Heibel, C.; Naumann, R.; Offenhausser, A.; Ruhe, J.; Schmidt, E. K.; Shen, W. W.; Sinner, A., Functional tethered lipid bilayers. *Reviews in Molecular Biotechnology* **2000,** 74, (3), 137-158.
136. Beyer, D.; Elender, G.; Knoll, W.; Kuhner, M.; Maus, S.; Ringsdorf, H.; Sackmann, E., Influence of anchor lipids on the homogeneity and mobility of lipid bilayers on thin polymer films. *Angewandte Chemie-International Edition in English* **1996,** 35, (15), 1682-1685.
137. Dietrich, C.; Tampe, R., Charge Determination of Membrane Molecules in Polymer-Supported Lipid Layers. *Biochimica Et Biophysica Acta-Biomembranes* **1995,** 1238, (2), 183-191.
138. Lang, H.; Duschl, C.; Vogel, H., A New Class of Thiolipids for the Attachment of Lipid Bilayers on Gold Surfaces. *Langmuir* **1994,** 10, (1), 197-210.
139. Bunjes, N.; Schmidt, E. K.; Jonczyk, A.; Rippmann, F.; Beyer, D.; Ringsdorf, H.; Graber, P.; Knoll, W.; Naumann, R., Thiopeptide-supported lipid layers on solid substrates. *Langmuir* **1997,** 13, (23), 6188-6194.
140. Naumann, R.; Jonczyk, A.; Hampel, C.; Ringsdorf, H.; Knoll, W.; Bunjes, N.; Graber, P., Coupling of proton translocation through ATPase incorporated into supported lipid bilayers to an electrochemical process. *Bioelectrochemistry and Bioenergetics* **1997,** 42, (2), 241-247.
141. Naumann, R.; Schmidt, E. K.; Jonczyk, A.; Fendler, K.; Kadenbach, B.; Liebermann, T.; Offenhausser, A.; Knoll, W., The peptide-tethered lipid membrane as a biomimetic system to incorporate cytochrome c oxidase in a functionally active form. *Biosensors & Bioelectronics* **1999,** 14, (7), 651-662.
142. Schmidt, E. K.; Liebermann, T.; Kreiter, M.; Jonczyk, A.; Naumann, R.; Offenhausser, A.; Neumann, E.; Kukol, A.; Maelicke, A.; Knoll, W., Incorporation of the acetylcholine

receptor dimer from Torpedo californica in a peptide supported lipid membrane investigated by surface plasmon and fluorescence spectroscopy. *Biosensors and Bioelectronics* **1998,** 13, (6), 585-591.
143. Wagner, M. L.; Tamm, L. K., Tethered polymer-supported planar lipid bilayers for reconstitution of integral membrane proteins: Silane-polyethyleneglycol-lipid as a cushion and covalent linker. *Biophysical Journal* **2000,** 79, (3), 1400-1414.
144. Erdelen, C.; Haussling, L.; Naumann, R.; Ringsdorf, H.; Wolf, H.; Yang, J. L.; Liley, M.; Spinke, J.; Knoll, W., Self-Assembled Disulfide-Functionalized Amphiphilic Copolymers on Gold. *Langmuir* **1994,** 10, (4), 1246-1250.
145. Spinke, J.; Yang, J.; Wolf, H.; Liley, M.; Ringsdorf, H.; Knoll, W., Polymer-Supported Bilayer on a Solid Substrate. *Biophysical Journal* **1992,** 63, (6), 1667-1671.
146. Wiegand, G.; Arribas-Layton, N.; Hillebrandt, H.; Sackmann, E.; Wagner, P., Electrical properties of supported lipid bilayer membranes. *Journal of Physical Chemistry B* **2002,** 106, (16), 4245-4254.
147. Cornell, B. A.; BraachMaksvytis, V. L. B.; King, L. G.; Osman, P. D. J.; Pace, R. J.; Raguse, B.; Wieczorek, L., A synthetic gated ion channel within a synthetic tethered membrane. *Biophysical Journal* **1997,** 72, (2), TH289-TH289.
148. Schiller, S. M.; Naumann, R.; Lovejoy, K.; Kunz, H.; Knoll, W., Archaea analogue thiolipids for tethered bilayer lipid membranes on ultrasmooth gold surfaces. *Angewandte Chemie-International Edition* **2003,** 42, (2), 208-+.
149. Schiller, S.; Naumann, R.; Lovejoy, K.; Knoll, W., Thiolipids for tethered bilayer membranes. *Abstracts of Papers of the American Chemical Society* **2003,** 225, U539-U540.
150. Braach-Maksvytis, V.; Raguse, B., Highly impermeable "soft" self-assembled monolayers. *Journal of the American Chemical Society* **2000,** 122, (39), 9544-9545.
151. Epand, R. M., Biophysical studies of lipopeptide-membrane interactions. *Biopolymers* **1997,** 43, (1), 15-24.
152. Woese, C. R.; Fox, G. E., Phylogenetic Structure of Prokaryotic Domain - Primary Kingdoms. *Proceedings of the National Academy of Sciences of the United States of America* **1977,** 74, (11), 5088-5090.
153. Mathai, J. C.; Sprott, G. D.; Zeidel, M. L., Molecular mechanisms of water and solute transport across archaebacterial lipid membranes. *Journal of Biological Chemistry* **2001,** 276, (29), 27266-27271.
154. Butt, H. J.; Muller, T.; Gross, H., Immobilizing Biomolecules for Scanning Force Microscopy by Embedding in Carbon. *Journal of Structural Biology* **1993,** 110, (2), 127-132.
155. Naumann, R.; Schiller, S. M.; Giess, F.; Grohe, B.; Hartman, K. B.; Karcher, I.; Koper, I.; Lubben, J.; Vasilev, K.; Knoll, W., Tethered lipid Bilayers on ultraflat gold surfaces. *Langmuir* **2003,** 19, (13), 5435-5443.
156. Kim, S.; Morimoto, S.; Koh, E.; Miyashita, Y.; Ogihara, T., Comparison of Effects of a Potassium Channel Opener Brl34915, a Specific Potassium Ionophore Valinomycin and Calcium-Channel Blockers on Endothelin-Induced Vascular Contraction. *Biochemical and Biophysical Research Communications* **1989,** 164, (3), 1003-1008.
157. Cammann, K., Ion-Selective Bulk Membranes as Models for Biomembranes - Active Ion-Transport as a Consequence of Stationary State Situations at Asymmetric Biomembranes. *Topics in Current Chemistry* **1985,** 128, 219-259.
158. Lauger, P., Carrier-Mediated Ion Transport. *Science* **1972,** 178, (4056), 24-&.
159. http://www.imb-jena.de/peptaibols/1AMT.html.
160. http://user.chollian.net/~jtoh/data/data_pro.htm.
161. Woolley, G. A.; Wallace, B. A., Model Ion Channels - Gramicidin and Alamethicin. *Journal of Membrane Biology* **1992,** 129, (2), 109-136.

162. Sansom, M. S. P., Models and simulations of ion channels and related membrane proteins. *Current Opinion in Structural Biology* **1998,** 8, (2), 237-244.
163. Tieleman, D. P.; Berendsen, H. J. C.; Sansom, M. S. P., An Alamethicin Channel in a Lipid Bilayer: Molecular Dynamics Simulations. *Biophys. J.* **1999,** 76, (4), 1757-1769.
164. Cafiso, D. S., Alamethicin: A Peptide Model for Voltage Gating and Protein-Membrane Interactions. *Annual Review of Biophysics and Biomolecular Structure* **1994,** 23, (1), 141-165.
165. Gordon, L. G. M.; Haydon, D. A., Potential-Dependent Conductances in Lipid-Membranes Containing Alamethicin. *Philosophical Transactions of the Royal Society of London Series B-Biological Sciences* **1975,** 270, (908), 433-447.
166. Boheim, G.; Hanke, W.; Jung, G., Alamethicin Pore Formation - Voltage-Dependent Flip-Flop of Alpha-Helix Dipoles. *Biophysics of Structure and Mechanism* **1983,** 9, (3), 181-191.
167. Latorre, R.; Alvarez, O., Voltage-Dependent Channels in Planar Lipid Bilayer-Membranes. *Physiological Reviews* **1981,** 61, (1), 77-150.
168. Fox, R. O.; Richards, F. M., A Voltage-Gated Ion Channel Model Inferred from the Crystal-Structure of Alamethicin at 1.5-a Resolution. *Nature* **1982,** 300, (5890), 325-330.
169. Hall, J. E.; Vodyanoy, I.; Balasubramanian, T. M.; Marshall, G. R., Alamethicin - a Rich Model for Channel Behavior. *Biophysical Journal* **1984,** 45, (1), 233-247.
170. Mathew, M. K.; Balaram, P., A Helix Dipole Model for Alamethicin and Related Transmembrane Channels. *Febs Letters* **1983,** 157, (1), 1-5.
171. Rizzo, V.; Stankowski, S.; Schwarz, G., Alamethicin Incorporation in Lipid Bilayers - a Thermodynamic Study. *Biochemistry* **1987,** 26, (10), 2751-2759.
172. Gilbert Baumann, P. M., A molecular model of membrane excitability. *Journal of Supramolecular Structure* **1974,** 2, (5-6), 538-557.
173. Huang, H. W.; Wu, Y., Lipid-Alamethicin Interactions Influence Alamethicin Orientation. *Biophysical Journal* **1991,** 60, (5), 1079-1087.
174. Brogden, K. A., Antimicrobial peptides: pore formers or metabolic inhibitors in bacteria? *Nat Rev Micro* **2005,** 3, (3), 238-250.
175. Miller, C.; Cuendet, P.; Gratzel, M., K+ Sensitive Bilayer Supporting Electrodes. *Journal of Electroanalytical Chemistry* **1990,** 278, (1-2), 175-192.
176. Kleyman, T. R.; Cragoe, E. J., Amiloride and Its Analogs as Tools in the Study of Ion-Transport. *Journal of Membrane Biology* **1988,** 105, (1), 1-21.
177. Rietschel, E. T.; Brade, H., Bacterial endotoxins. *Scientific American* **1992,** 267, (2), 54.
178. Rietschel, E. T.; Kirikae, T.; Schade, F. U.; Mamat, U.; Schmidt, G.; Loppnow, H.; Ulmer, A. J.; Zahringer, U.; Seydel, U.; Di Padova, F., Bacterial endotoxin: molecular relationships of structure to activity and function. *FASEB J.* **1994,** 8, (2), 217-225.
179. Schletter, J.; Heine, H.; Ulmer, A. J.; Rietschel, E. T., Molecular mechanisms of endotoxin activity. *Archives of Microbiology* **1995,** 164, (6), 383-389.
180. Lerouge, I.; Vanderleyden, J., O-antigen structural variation: mechanisms and possible roles in animal/plant-microbe interactions. *Fems Microbiology Reviews* **2002,** 26, (1), 17-47.
181. Raetz, C. R. H.; Whitfield, C., Lipopolysaccharide endotoxins. *Annual Review of Biochemistry* **2002,** 71, 635-700.
182. Holst, O.; Mullerloennies, S.; Lindner, B.; Brade, H., Chemical-Structure of the Lipid-a of Escherichia-Coli J-5. *European Journal of Biochemistry* **1993,** 214, (3), 695-701.
183. Knirel, Y. A.; Kochetkov, N. K., The Structure of Lipopolysaccharides of Gram-Negative Bacteria .1. General Characterization of the Lipopolysaccharides and the Structure of Lipid a - (a Review). *Biochemistry-Moscow* **1993,** 58, (2), 73-84.

184. Holst, O.; Susskind, M.; Grimmecke, D.; Brade, L.; Brade, H., Core structures of enterobacterial lipopolysaccharides. In *Endotoxin and Sepsis*, 1998; Vol. 397, pp 23-35.
185. Erridge, C.; Bennett-Guerrero, E.; Poxton, I. R., Structure and function of lipopolysaccharides. *Microbes and Infection* **2002,** 4, (8), 837-851.
186. Nuno C. Santos, A. C. S. M. A. R. B. C. J. M.-S. C. S., Evaluation of Lipopolysaccharide Aggregation by Light Scattering Spectroscopy. *ChemBioChem* **2003,** 4, (1), 96-100.
187. Jauho, E. S.; Boas, U.; Wiuff, C.; Wredstrom, K.; Pedersen, B.; Andresen, L. O.; Heegaard, P. M.; Jakobsen, M. H., New technology for regiospecific covalent coupling of polysaccharide antigens in ELISA for serological detection. *Journal of Immunological Methods* **2000,** 242, (1-2), 133-143.
188. Aurell, C. A.; Wistrom, A. O., Critical aggregation concentrations of gram-negative bacterial lipopolysaccharides (LPS). *Biochemical and Biophysical Research Communications* **1998,** 253, (1), 119-123.
189. Muhle, S. A.; Tam, J. P., Design of gram-negative selective antimicrobial peptides. *Biochemistry* **2001,** 40, (19), 5777-5785.
190. Ulmer, A. J.; Rietschel, E. T.; Zahringer, U.; Heine, H., Lipopolysaccharide: Structure, bioactivity, receptors, and signal transduction. *Trends in Glycoscience and Glycotechnology* **2002,** 14, (76), 53-68.
191. Joseph B. Mcphee, R. E. W. H., Function and therapeutic potential of host defence peptides. *Journal of Peptide Science* **2005,** 11, (11), 677-687.
192. Alessandro Tossi, L. S. A. G., Amphipathic.
193. Epand, R. M.; Vogel, H. J., Diversity of antimicrobial peptides and their mechanisms of action. *Biochimica et Biophysica Acta (BBA) - Biomembranes* **1999,** 1462, (1-2), 11-28.
194. Frecer, V.; Ho, B.; Ding, J. L., De Novo design of potent antimicrobial peptides. *Antimicrobial Agents and Chemotherapy* **2004,** 48, (9), 3349-3357.
195. Frecer, V.; Ho, B.; Ding, J. L., Interpretation of biological activity data of bacterial endotoxins by simple molecular models of mechanism of action. *European Journal of Biochemistry* **2000,** 267, (3), 837-852.
196. Yu, L.; Ding, J. L.; Ho, B.; Wohland, T., Investigation of a novel artificial antimicrobial peptide by fluorescence correlation spectroscopy: An amphipathic cationic pattern is sufficient for selective binding to bacterial type membranes and antimicrobial activity. *Biochimica Et Biophysica Acta-Biomembranes* **2005,** 1716, (1), 29-39.
197. Lingler, S.; Rubinstein, I.; Knoll, W.; Offenhausser, A., Fusion of small unilamellar lipid vesicles to alkanethiol and thiolipid self-assembled monolayers on gold. *Langmuir* **1997,** 13, (26), 7085-7091.
198. Koper, I.; Schiller, S. M.; Giess, F.; Naumann, R.; Knoll, W.; Liu, A. L., Chapter 2 Functional Tethered Bimolecular Lipid Membranes (tBLMs). In *Advances in Planar Lipid Bilayers and Liposomes*, Academic Press: 2006; Vol. Volume 3, pp 37-53.